TÉCNICO LISBOA

Use of Retaining Walls in Shallow Geothermal Energy Systems

Duarte Nuno de Jesus Silva

Thesis to obtain the Master of Science Degree in

Civil Engineering

Supervisor:

Prof. Dr. Peter John Bourne-Webb

Examination Committee

Chairperson: Prof.ª Dr.ª Teresa Maria Bodas de Araújo Freitas

Supervisor: Prof. Dr. Peter John Bourne-Webb

Member of the Committee: Prof. Dr. José Manuel Vaz Velho Barbosa Marques

December 2020

Declaração

Declaro que o presente documento é um trabalho original da minha autoria e que cumpre todos os requisitos do Código de Conduta e Boas Práticas da Universidade de Lisboa.

Acknowledgements

I would like to thank my supervisor, Prof. Peter Bourne-Webb for all the support, guidance and motivation to develop this work. His experience, knowledge and positive attitude inspired me to question, think, deliver and seek for more, continuously. I am going to take that for life. I am also deeply grateful for the opportunity to contribute to such an interesting and complex subject, that introduced me to the demanding field that research is.

I would also like to thank DHI for providing an educational licensing for the MIKE Powered by DHI Software FEFLOW, that allowed me to perform the numerical analysis presented in this thesis.

To all the friends I have made over the past few years at Técnico, thank you for sharing this ride with me. To Ana and Miguel for the fellowship, support and friendship throughout all these years of teamwork. To my oldest friends and housemates, Adriana and Solange, for all the laughs during those endless dinners that helped lighten up after a day at Técnico.

Lastly, I would like to thank to all of my family for making me what I am today. To my parents and sister, that always inspired me, for the unique opportunity and support at home. To my godmother, for being my second mom. To Raquel, my anchor, for being there for me everyday with an unconditional love. To my godchildren, I hope I made you proud.

Abstract

Shallow geothermal energy has been used to provide renewable thermal energy to residential and commercial buildings, mainly by means of ground source heat pump systems that leverage the soil heat storage potential. One main drawback of these systems is the high capital cost associated with their construction that can be significantly reduced if the heat exchanger loops are incorporated into piles, retaining walls and tunnel linings, being therefore classified as thermally-activated structures or energy geostructures. While energy piles are the most common application, in the last decade the interest around energy walls has increased. However, there are still some knowledge gaps regarding the thermal behaviour of energy walls that due to their complexity require numerical analyses to asses their thermal performance. Therefore, a thermal analysis of a diaphragm energy wall was undertaken in the finite element software FEFLOW. The software response was validated not only against a set of available field data but also against an existing numerical study, revealing a good agreement with both sets of data, which allowed to establish some guidelines for the assembly of the subsequent parametric study. The parametric study focused on the impact of the ground (soil thermal conductivity), wall geometry, heat exchanger loop layout, interior and exterior environment and thermal load on the heat transfer rate. The results show that the conditions in the excavated space have a significant impact on the heat transfer rate of energy walls, followed by the wall geometry and the soil thermal conductivity.

Keywords

Energy geostructures; energy walls; ground source heat pump systems; geothermal energy; renewable energy;

Resumo

A energia geotérmica superficial tem sido utilizada para fornecer energia térmica renovável a edifícios, através de sistemas de bombas de calor geotérmicas que alavancam o potencial de armazenamento de energia no solo. A principal desvantagem destes sistemas prende-se com o elevado custo associado à sua construção, podendo ser significativamente reduzido se os permutadores de calor forem incorporados em estacas, muros de contenção e túneis, sendo, por isso, classificados como estruturas ativadas geotermicamente ou estruturas geotérmicas. Embora as estacas termo-ativas sejam a aplicação mais comum, na última década, o interesse em torno das paredes termo-ativas aumentou. No entanto, ainda existem lacunas no conhecimento sobre o comportamento térmico das mesmas pelo que, devido à sua complexidade, se recorre a análises numéricas para avaliar o seu desempenho térmico. Assim, realizou-se uma análise térmica a uma parede moldada termo-ativa, no programa de elementos finitos FEFLOW. A resposta computacional foi validada não apenas por comparação com um conjunto de dados experimentais disponíveis, mas também com um estudo numérico existente, apresentando uma boa concordância com ambos os conjuntos de dados e permitindo estabelecer algumas diretrizes para o subsequente estudo paramétrico. Este, focou-se no impacto da condutividade térmica do solo, da geometria da parede, do layout do permutador de calor, e do ambiente externo e interno e da carga térmica, na taxa de transferência de calor. Os resultados mostram que as condições na zona de escavação têm um impacto significativo na taxa de transferência de calor seguidas da geometria da parede e da condutividade térmica do solo.

Palavras-Chave

Estruturas ativadas geotermicamente; paredes termo-ativas; bombas de calor geotérmicas; energia geotérmica; energia renovável;

Table of Contents

List of Figures

List of Tables

List of Acronyms

1D	One-dimensional
2D	Two-dimensional
3D	Three-dimensional
BC	Boundary condition
CFA	Continuous flight auger
COP	Coefficient of performance
EGS	Enhanced geothermal system
HDPE	High-density polyethylene
GHE	Ground heat exchanger
GSHP	Ground-source heat pump
SGE	Shallow geothermal energy
SPF	Seasonal performance factor

List of Symbols

Latin Alphabet

A	Cross sectional area
A_w	Total wall surface area on the retained soil side
b	Hydraulic aperture
c	Specific heat capacity
c_p	Fluid specific heat capacity at constant pressure
c_s	Solid phase specific heat capacity
c_w	Water specific heat capacity
C	Concrete cover to pipes
d_i	Pipe inner diameter
d_o	Pipe outer diameter
D_b	Embedded depth of the wall below excavation level
D_e	Excavation depth
D_w	Wall depth
D_{wb}	Distance between the wall base and bottom model boundary
D_{wr}	Distance between the wall and right model boundary
E	Energy removed or supplied

E_{bt_pump}	Electrical energy use of the buffer tank pump
E_{HW_bu}	Energy use of back-up heater for space heating and domestic hot water
E_{HW_hp}	Electrical energy use of the heat pump for space heating and domestic hot water
$E_{B_{fan/pump}}$	Electrical energy use of the heat sink (building): fans or pumps for space heating and domestic hot water
$E_{S_{fan/pump}}$	Electrical energy use of the heat pump source fan or heat carrier fluid pump for space heating and domestic hot water
g_z	Gravity along z-axis
h	Convective heat transfer coefficient
H_L	Height of the loop on the embedded part of the wall
L	Length of the heat exchanger loop
m	Mass flow rate
n	Porosity
q	Heat transfer rate per wall surface area
q_{conv}	Rate of the heat transfer per unit of area by convection
q_{cond}	Rate of the heat transfer per unit of area by conduction
q_L	Heat transfer rate per meter of pipe
Q	Exchanged power
Q_{H_hp}	Quantity of heat of the heat pump in space heating operation
Q_{W_hp}	Quantity of heat of the heat pump in domestic hot water operation
r	Radial coordinate
r_{hydr}	Hydraulic radius
R	Wall to excavation depth ratio
R_e	Reynolds number
R_p	Radius of the pipe
S_L	Longitudinal spacing between pipe branches
S_T	Transverse spacing between pipe branches
T_C	Absolute temperature of cold reservoir
T_f	Fluid temperature
T_H	Absolute temperature of hot reservoir
T_i	Inlet temperature
T_o	Outlet temperature
T_s	Surface temperature
t_w	Pipe wall thickness
T_w	Wall thickness

v	Fluid velocity
V	Total volume of soil
V_a	Volume of air
V_s	Volume of solids
V_v	Volume of voids
V_w	Volume of water
v_z	Fluid velocity along z-axis
W	Panel width
W_r	Work required by the system for heating and cooling

Greek Alphabet

α	Thermal diffusivity
ΔT	Temperature difference between soil and air in contact with the wall surface
λ	Thermal conductivity
λ_{conc}	Concrete thermal conductivity
λ_s	Soil thermal conductivity
λ_w	Water thermal conductivity
μ	Dynamic viscosity of the fluid
ρ	Bulk density
ρc	Volumetric heat capacity
ρ_f	Fluid density
ρ_s	Solid phase density
ρ_w	Water density
∇T	Temperature gradient

1 Introduction

1.1 Overview

Global energy demand has seen an exponential increase in the past decades due to the growing population and the quest for a better quality of life, with the majority of that energy demand being fulfilled by energy sources with great impact on the environment, like fossil fuels. Since it is expected that energy consumption will continue to rise, it is essential to shift from coal, oil, and natural gas to renewable energy sources, even with energy production at the local level. As a result, geothermal energy has great potential to become one of the most relevant energy sources since it can be produced locally, is widely available and is sustainable.

Geothermal energy systems extract heat from the Earth's subsurface and can be divided into two different categories depending on the depth and source temperature. "Deep" geothermal is characterized by depths greater than 150 m and up to several km's and temperatures greater than about 30°C, which can be used for direct heating purposes and when higher than about 90°C can be used for the generation of electric power. "Shallow" geothermal is characterized by depths less than about 150 m and lower temperatures (typically <30°C) , which with the aid of a heat pump can be used to provide heating and cooling (Goetzl, 2020) .

Shallow geothermal energy (SGE) systems can play an important role in the energy transition to sustainable and renewable energy since the energy source is always available, which means that system availability is not dependent on the time of the day neither on weather conditions. Also, the ground temperature, below a few meters of depth, is almost constant throughout the year, allowing the ground to accept excess heat in the summer and release heat in the winter, acting as heat storage when the thermal load is balanced throughout the year, which makes the system independent from solar energy gains.

SGE systems have been widely used for several decades, in northern Europe and North America. These systems allow the heat exchange between the primary circuit (ground heat exchanger, GHE, typically formed in boreholes or trenches), that exchanges heat to and from the ground, and the secondary circuit that exchanges heat to and from the building, though a heat pump referred to as ground source heat pump (GSHP). The GSHP allows these systems with small temperature gradients to operate very efficiently, with a coefficient of performance (COP) of over four which means that for every kilowatt of energy spent to run the heat pump, it provides four kilowatts of heat or cooling.

Additionally, if the energy provided by the GSHP doesn't fully satisfy the buildings energy demand, the system can incorporate additional heat and cooling sources like electric resistances, solar collectors and air-source heat pumps that allow energy exchange through low-temperature heating systems, such as radiant floor heating, and air-conditioning units.

Since the 1980s, absorber pipes acting as GHE began to be installed in foundation elements and other geotechnical structures, first in piles and naturally evolving to retaining walls, slabs and tunnel linings. These energy geostructures or energy foundations allow a significant capital cost reduction when building a SGE system as they can incorporate GHEs without losing their main geotechnical purpose, thus removing the relative high additional cost associated with drilling borehole GHEs. These types of energy geostructures have been implemented in projects across countries like Austria, Switzerland, and the United Kingdom, with energy piles being the most common application. This is driven by the geometry resemblance to boreholes, with available thermal methods that can be adapted to energy piles and the reduced capital costs compared to vertical GHEs, hence energy piles being the most subject to research in recent years.

Energy walls have seen an increase in interest in recent years, particularly in diaphragm walls over piled walls, but there is still plenty to understand regarding which factors influence energy walls efficiency the most. A significant proportion of the knowledge related to energy piles does not apply to energy retaining walls because of their inherent differences: piles are surrounded by soil and exhibit a cylindrical shape as opposed to diaphragm walls that have one of the faces exposed to the environment and extend longitudinally. Additionally, retaining walls can be constructed as walls for building basements walls, metro stations or cut and cover tunnels. These geometrical differences add complexity to the thermal design of energy walls, with previous work showing that accurately assessing the environment in contact with the exposed face of the wall is a key factor to evaluate energy walls efficiency.

Although interest has been rising, energy walls still lack a full understanding of their thermal and thermal-mechanical behaviour, and suitable design guidelines, with high variability of implemented solutions from project to project. Some research has found that thermally-induced stresses are non-negligible in some wall cases since they can cause serviceability problems that must be taken into account when designing such structure, but no evidence was found that thermal-activation of the wall compromises structural behaviour. Concluding therefore that structural impacts are of minor importance, the focus of this thesis is the thermal performance of thermally-activated diaphragm walls, with the objective of eventually providing guidelines that can be applied to design of such walls herein referred to as Energy D-walls.

1.2 Motivations and objectives

Energy walls have been demonstrated to have the potential to be used as SGE systems, both as an alternative and as a complement to other energy geostructures. This thesis is driven by the possible role that energy geostructures will have on the future energy transition and aims to provide useful knowledge that can contribute to a better understanding of the thermal behaviour and energy performance of Energy D-walls. To accomplish this, a parametric study will be performed through numerical modelling to evaluate the effects on energy exploitation. A set of objectives were defined:

- Based on a literature review, identify the role of energy walls as a shallow geothermal energy system, as well as the parameters that might influence the thermal performance of energy walls the most;
- Perform a numerical parametric study based on a set of differing conditions and evaluate the impact of each parameter on the heat exchange performance;
- Propose preliminary design guidance to predict the heat exchange potential of an energy wall.

1.3 Structure of the thesis

This dissertation is organized in six chapters. In this Chapter 1, a general overview of the geothermal energy and the ground source heat pump systems, specifically energy walls, is presented and the document organization described.

The following two chapters focus on the literature review. In Chapter 2, the two types of geothermal energy are introduced, the differences highlighted as well as the means to exploit them. Detail is given to ground source heat pump systems, a way to exploit shallow geothermal energy that can be broadly implemented. The efficiency of these types of system, alongside the variety of ways to implement them is also discussed. A summary of the systems defined in the literature is presented and special attention is given to energy geostructures.

In Chapter 3, energy walls are introduced and some details regarding their implementation and construction presented. As the use of energy walls as ground heat exchangers is fairly recent, special attention was given to detail significant implementation projects of energy walls, as they provide valuable information regarding the technical difficulties that had to be overcome or considered to implement and design such projects. Following the detailing of the field data, a number of numerical analyses are presented and the assumptions compared to the implemented projects.

Chapter 4 focuses on the introduction and validation of the finite element software FEFLOW. The validation is undertaken with reference to a field test presented in Chapter 3 and also against a parametric study developed with the same software. The sensitivity of the software to parameters such as mesh size and time-stepping is tested and validated, for application in next chapter. In Chapter 5, the parametric study is fully detailed and the varying parameters defined. The software response to the mesh and domain size is evaluated one more time. The aim of this chapter is to provide useful knowledge to the complex analysis of an energy wall and to highlight how different parameters impact the heat transfer rate.

In Chapter 6, the main conclusions of the research are presented and some recommendations for future developments are suggested.

2 Geothermal energy and ground heat exchangers

2.1 Geothermal energy

2.1.1 Deep geothermal energy

The subsurface layers of the Earth store energy originating from Earth's formation that is responsible for the earth's internal dynamics. Geothermal energy is energy extracted as heat from the subsurface and depending on the location, the geothermal gradient, the rate at which the ground temperature increases with depth, can exhibit considerable values, typically in locations where volcanic activity is present. Figure 2.1 shows the heat flow rate for Europe in which red areas indicate volcanic fields. In these cases, the geothermal energy arises at the surface or near-surface depths as steam and hot water, allowing the exploitation of deep geothermal energy at electrical power plants or district heating systems. Additionally, deep geothermal energy can also be extracted at locations without volcanic activity but with some mantle base energy sources, by drilling wells with depths of kilometres to pump the heat to the surface that, depending on the pressure and temperature conditions at each location, the heat transfer fluid can either be water or steam. Also, when a hot rock mass is impermeable or fluid is absent or both, a third well can be drilled to inject water to the hot rock mass and force permeability, with these systems being referred to as enhanced geothermal systems (EGS) (Chamorro et al., 2014). Because of the cost associated with the drilling of such wells (10s of millions of euros), deep geothermal energy requires significant investment and rigorous planning, hence not being broadly available. Geothermal energy is still available in places where volcanic activity is absent, or the economic viability of deep geothermal energy is not achievable, by means of shallow geothermal energy.

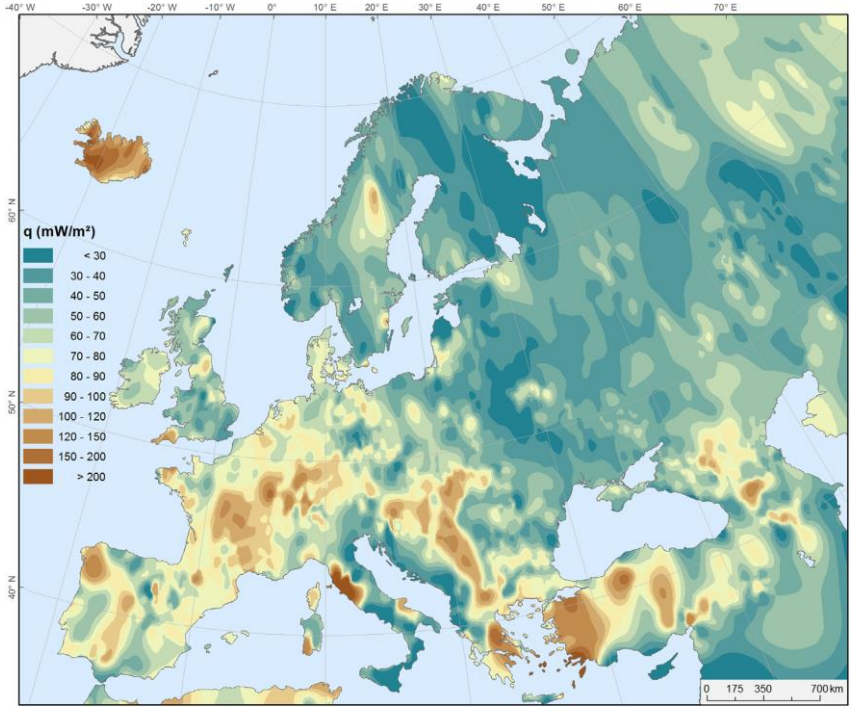

Figure 2.1 - Heat flow rate map for Europe (Chamorro et al., 2014).

2.2 Shallow geothermal energy and ground source heat pump systems

Shallow geothermal energy (SGE), as opposed to deep geothermal energy, does not make use of heat from mantle-based energy sources. Instead, it takes advantage of the energy storage potential in the ground in the first hundred metres of the upper crust to exchange heat to and from the ground. The first 10-15 m of depth exhibit a seasonal temperature change due to surface conditions (Figure 2.2). Below these depths, the ground temperature is constant year-round and similar to the average air temperature at the surface, therefore being characterized by "normal" ground temperatures. This allows heat disposal to the ground in the summer when air temperatures are higher than the yearly average and to harvest that heat in winter when air temperatures are lower than the ground temperature.

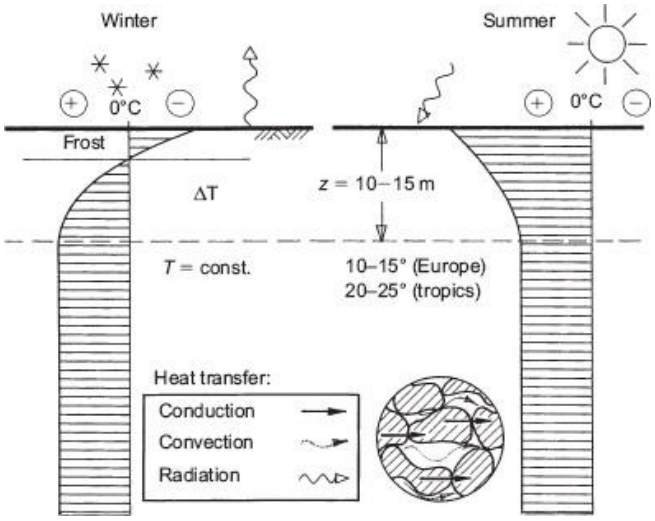

Figure 2.2 - Ground temperature profile for shallow depths (Brandl, 2006).

According to Banks (2012) Spain typical ground temperature is between 15ºC and 19ºC. Calado (2016) reported some ground temperature profiles from weekly field observations between December 2015 and October 2016 at Covilhã, Portugal. The average ground temperature at 5 m depth was reported to be 16.3ºC for one location monitored from December 2015 to October 2016), 12.5ºC and 12.7ºC at another location (monitored from February 2016 to October 2016 and April 2016 to October 2016, respectively). In all locations, the ground temperature at 5 m depth was lower (spring and summer) or higher (winter) than the external air temperature, which confirms the heat exchange potential with the ground. Additionally, the 24 hour field monitoring tests show almost no temperature variation during the day at 5 m of depth (16ºC in February, 13ºC in June and 15ºC in August) which indicates that temperature changes, at this depth and below, occur gradually and are delayed relative to the external air temperature that generates them. Furthermore, the ground temperature at 5 m depth is similar to the 13.6ºC yearly average air temperature for Covilhã. Considering the previous and the projected average air temperature for 2011-2040 in Lisbon (IPMA, 2015), it is possible to establish the average ground temperature in Lisbon at around 16.85ºC (Figure 2.3).

Since SGE systems operate with low-temperature gradients, a heat pump must be installed to boost the efficiency of the system, enabling broader applications of SGE systems to satisfy the demand for heating, cooling and hot water production in residential, services and public buildings at any location.

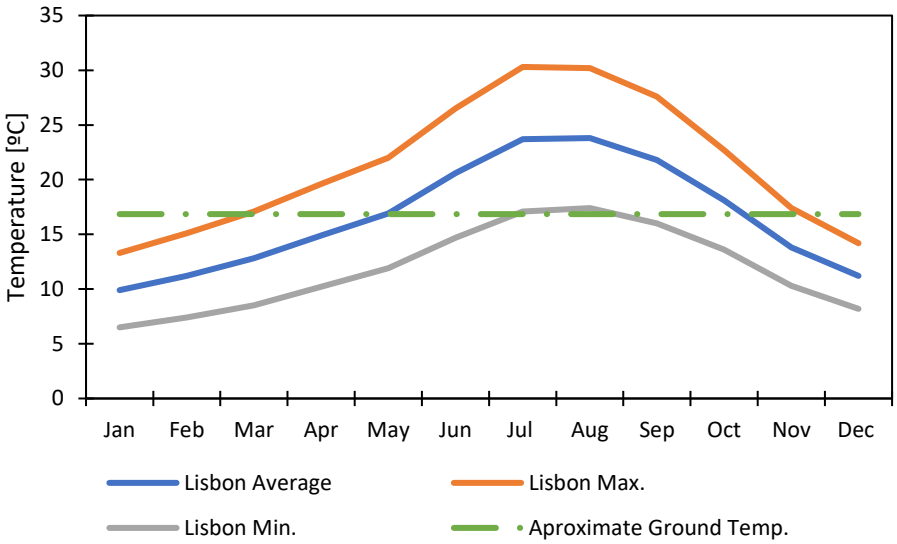

Figure 2.3 - Year, maximum and minimum temperature air temperature projected for 2011-2040 in Lisbon. Adapted from IPMA (2015).

2.2.1 GSHP technology

As mentioned previously, GSHP are used to boost the efficiency of SGE systems due to the low-temperature gradients that are common in these systems. The energy exploited has proven to be of great use in residential, office, services, and public buildings and new special applications in heating and cooling of bridge decks, roads, parking lots, and airport runways (Brandl, 2006).

A GSHP system has three main components (Figure 2.4): the primary circuit or ground loop, the heat pump, and the secondary circuit. The primary circuit consists of absorber pipes acting as ground heat exchangers that are embedded into the ground or concrete and come in a variety of layouts that vary accordingly to the type of system (see Section 2.2.2). In heating mode, the heat pump extracts heat from the primary circuit and raises the internal refrigerant fluid to a temperature compatible with that required by the secondary circuit (Figure 2.5). The secondary circuit runs through the interior of the building to provide space heating or through other infrastructures in case of special applications. Many GSHPs are reversible, meaning the process within the heat pump can be used for cooling provision in the secondary circuit, i.e. heat is taken from the building and injected into the ground. What makes the process so special is that the amount of energy needed to run the system is small compared to the heat output, i.e. following Figure 2.4, for each unit of input energy, four units of heat are produced by the heat pump. More details regarding the metrics available to assess the efficiency of GSHP and SGE systems can be consulted in Appendix A.

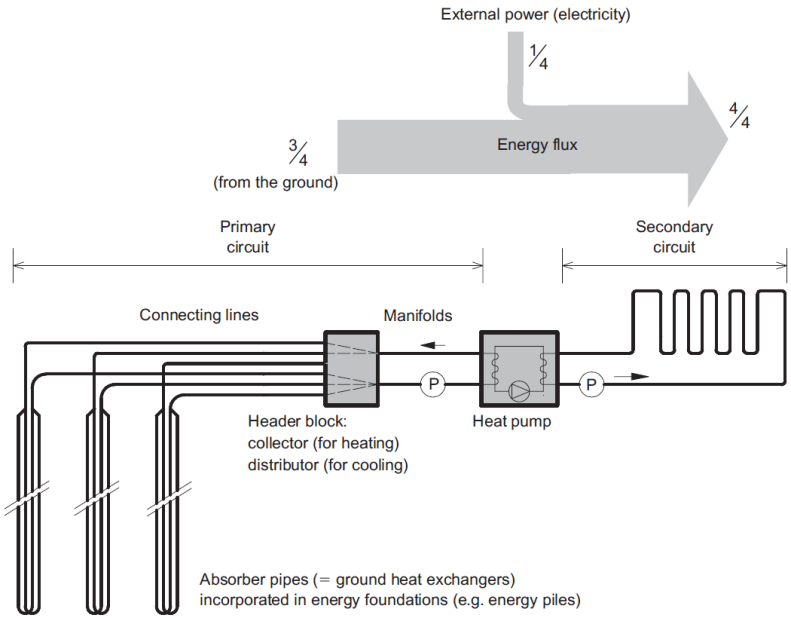

Figure 2.4 - Schematic representation of a GSHP system (Brandl, 2006).

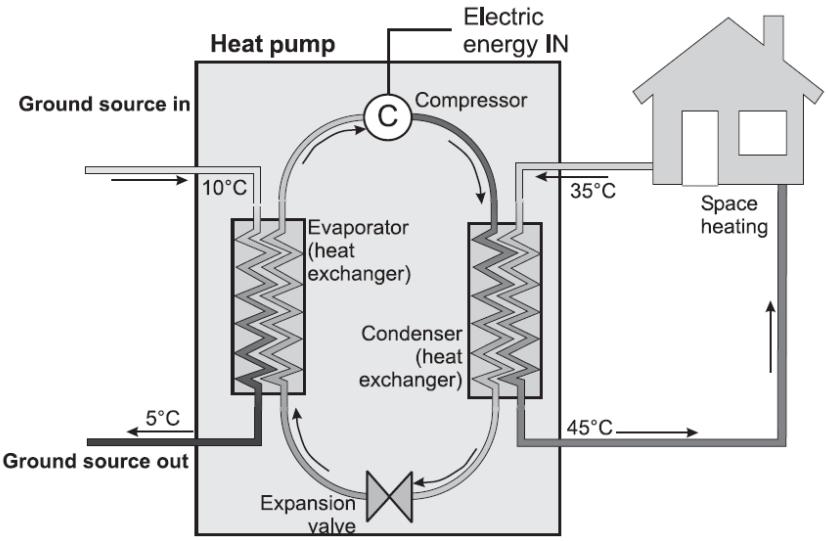

Figure 2.5 - Schematic diagram of a heat pump adapted from Banks (2012).

2.2.2 Heat exchange with the ground (Primary circuit)

Heat exchange with the ground is usually achieved through one of two approaches, so-called “open-loop” and “closed-loop” systems:

- Open-loop systems use groundwater as the heat carrier fluid that is pumped to the surface and that directly exchanges heat within the heat exchangers. These types of systems tend to extract more heat than closed-loop systems (Banks, 2012). Though, they are geology dependent, require higher capital costs and have higher running costs associated with the large amounts of pumped groundwater. Also, open-loop systems can present problems of clogging due to temperature

changes that induce mineral precipitation. Additionally, according to Snijders and Drijver (2016), open-loop systems have a bigger potential for direct cooling, i.e. heat exchange occurs without the need for the heat pump to work.

- In closed-loop systems, the heat transfer fluid, typically a solution of water and glycol (anti-freeze), runs through the high-density polyethylene (HDPE) absorber pipes installed as ground loops in trenches, vertical boreholes, and energy geostructures. The absorber pipes, that can run in a series or parallel configuration, form the primary circuit that exchanges heat through the heat pump with a secondary circuit that supply's heating and cooling to the building. Closed-loop systems can also be divided into two types: direct circulating systems, in which a high-pressure refrigerant fluid runs through the absorber pipes, typically from copper, and indirect circulation systems, in which a water-based fluid runs through HDPE absorber pipes, creating a closed circuit that exchanges heat at the GSHP evaporator with the GSHP's own circuit (Banks, 2012). The most common type is indirect circulation due to environmental concerns regarding refrigerant leakage and higher capital costs associated with the use of copper pipes.

The focus of this thesis is on closed loop GSHP systems where the ground heat exchanger (GHE) is integrated into a planar wall structure in the ground (Energy Wall). There are multiple applications of GSHP systems (Figure 2.6) with the most common being horizontal ground loops, vertical ground loops, and energy geostructures, which form a small but growing subset, and these are described in the following sections.

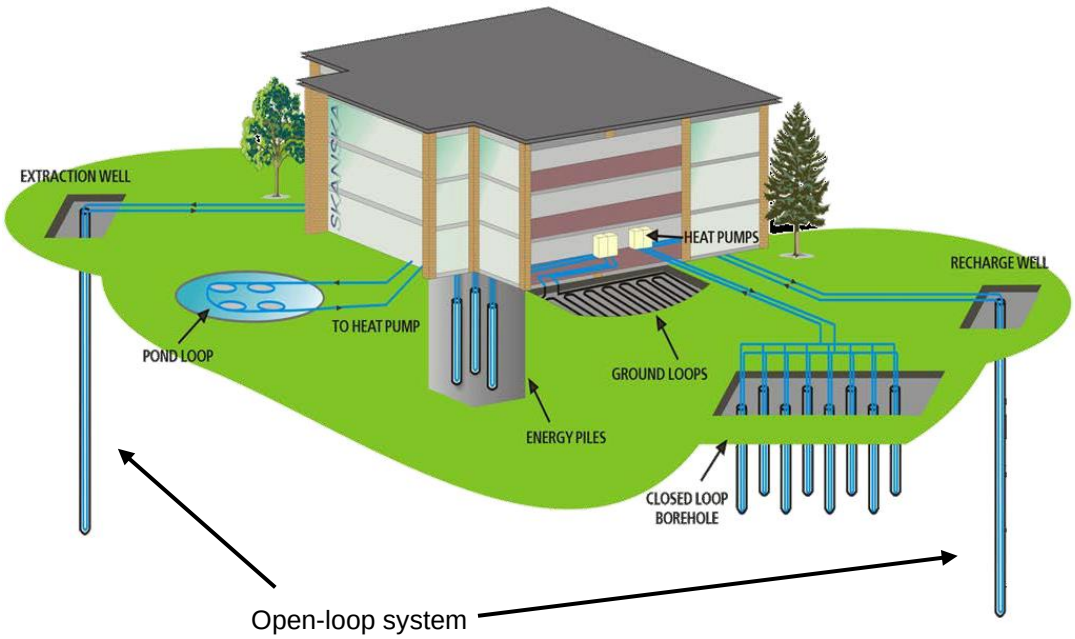

Figure 2.6 - Applications of ground heat exchangers (Amis, 2011).

2.2.2.1 Horizontal ground heat exchangers

Horizontal GHE are usually installed in shallow pits/trenches for new residential buildings or in retrofits of ones that have sufficient surrounding land area available. Compared to vertical GHEs (see following section), horizontal GHEs are less complex to install and require a lower initial investment due to reduced construction costs. These systems are usually installed in trenches, with depths between 1 m and 2 m that can be opened with common excavation machinery, thus eliminating the need for specialist equipment. However, to achieve the same energy performance, a horizontal GHE system may require higher land area usage than a vertical GHE system, even with multiple boreholes.

The inexpensive heat exchanger HDPE pipes can be arranged in several geometries, with the most common being: horizontal layout with parallel or in series connections, pipe in trench, trench collector (Figure 2.7) and “slinky” layouts, which can have horizontal or vertical configurations (Figure 2.8). Slinky heat exchangers are an interesting configuration due to the higher heat exchanger area per unit of trench length compared to parallel layouts and due to the ease of assembly since HDPE pipes are usually stored in a coil shape (Rees, 2016b). Additionally, this increase in the length of the heat exchanger loop has to be studied to check if the output heat transfer rate is higher than the additional pump energy consumption to overcome increased flow resistance. Banks (2012), cites values of 10 to15 m and 33 to 67 m of slinky heat exchanger trench and single pipe trench respectively, for every 1 kW of heat pump installed power, in heating mode. Although, the author points out that British guidelines tend to be more conservative, recommending respective peak heat extraction rates of 7 to 16 W m^{-1} (63 to 140m of trench) for single heat exchangers and 20 to 50 W m^{-1} (20 to 50 m of trench) for slinky heat exchangers.

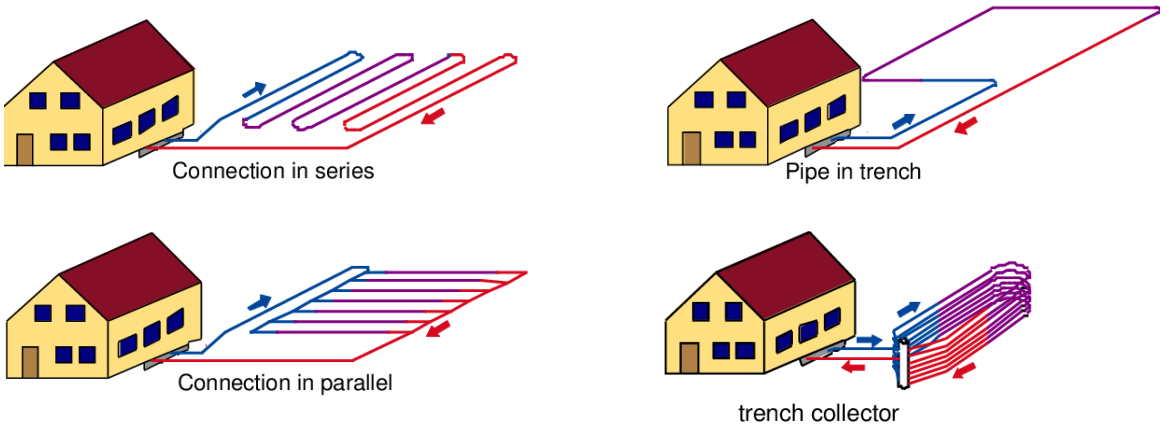

Figure 2.7 - Schematic configurations of horizontal GHE, adapted from Sanner (2004).

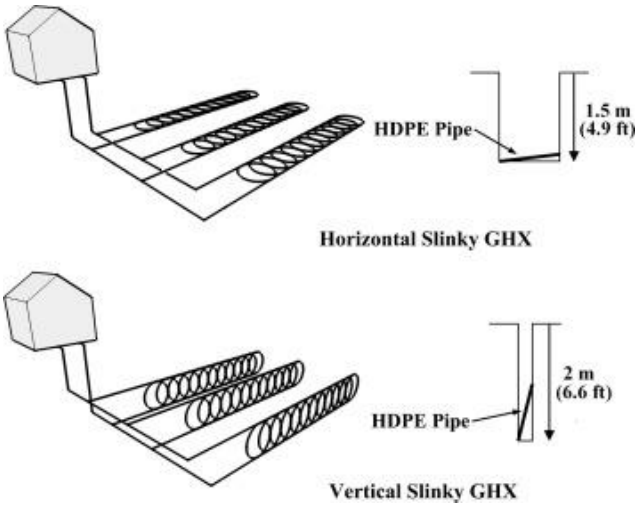

Figure 2.8 - Schematic Slinky pipe configurations (Xiong et al., 2015).

Finally, horizontal GHE must take into account the seasonal ground thermal property variations that occur due to groundwater table and soil saturation fluctuations, frost, surface ice or snow cover in cold climates and temperature variations, that below 100 mm depth follow a seasonal pattern (Rees, 2016b). Additionally, the backfill around the pipes should be made with a well-graded and high thermal conductivity granular material, like sand, to prevent soil clumps formation and uneven soil distribution, with air gaps, that create additional heat transfer resistance between the pipes and soil.

2.2.2.2 Vertical ground heat exchangers

In cases where the usable surface area is limited or there is a higher heat demand, vertical GHEs in the form of boreholes can become an alternative to shallow horizontal GHEs. Although not as economical, vertical GHE are less subject to near-surface ground temperature variations since the heat exchanger extends to much greater depths than a horizontal GHE. Therefore, vertical GHE must take into account the lithology of the subsurface, which greatly impacts the drilling technique choice and cost. In countries were the ground profile is more uniform, like in Sweden and Norway were a thin layer of loose sediments overlaps a rock layer, the drilling costs tend to be lower, due to standardization, than in places with more variable ground profiles, like the United Kingdom, in which the drilling technique must be adapted to the site specific characteristics (Banks, 2012).

Vertical GHE consist of embedding a heat exchanger circuit in a vertical borehole, typically drilled to depths that range between 70 m and 130 m. The depth of a borehole is a parameter that is dependent on multiple factors, like energy performance and cost. These are related since the deeper the borehole, the greater the expected heat exchange performance but slower the drilling rate which translates to higher costs. Therefore, a compromise between energy performance and cost should be achieved when the cost of drilling another borehole is lower than that to keep drilling deeper to meet a defined energy performance output.

The heat exchanger circuit layout is not fixed, with the most common types being a single U-pipe, a double U-pipe (with two inflow and two outflow branches) or a coaxial pipe, Figure 2.9. Borehole diameters usually range between 120 mm and 150 mm, and the spacing between the centre of the pipe branches ranges between 50 mm and 70mm. It is important to ensure that the pipe spacing remains constant throughout the borehole length to minimize pipe thermal interference and allow good grouting conditions. This is achieved by choosing a pre-fabricated layout that arrives at the site in a coil, ready to install with horizontal spacers separating the two pipes (Banks, 2012). To increase the heat exchange surface area, a double U-pipe can be installed, although the installation and grout process can be more difficult.

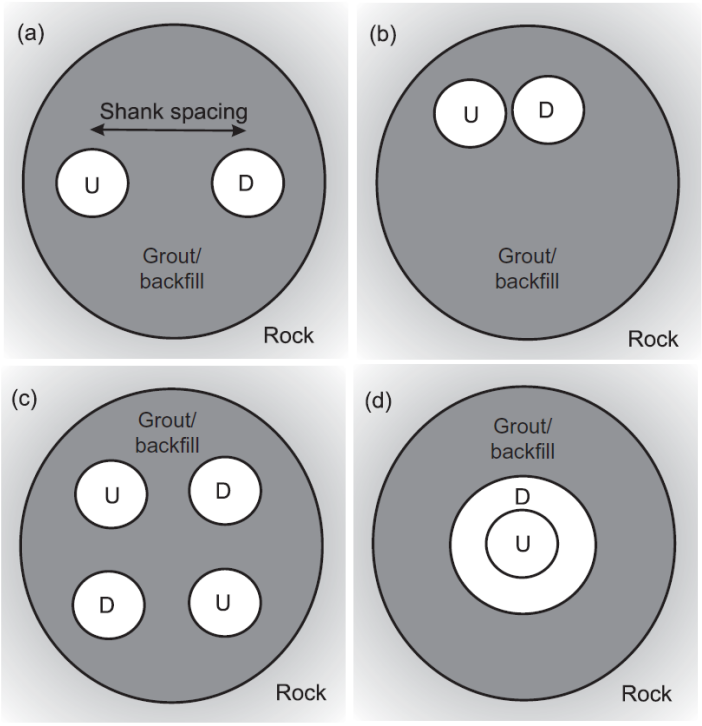

Figure 2.9 - Pipe layout cross-sections. a) correctly installed single U-pipe; b) single U-pipe without proper spacing; c) double U-pipe; d) coaxial pipe. 'U' refers to upflow or inflow branches and 'D' to downflow or outflow branches (Banks, 2012).

Banks, (2012) states that there is a relationship between the number of boreholes and the heat pump output capacity based on data from systems (installed and designed) in the UK, with values that range from 2 kW for borehole depths of 40 m to 17 kW for borehole depths of 180 m. Dividing the heat pump capacity output by the total drilled borehole depth, results in a linear metric, the specific installed thermal output. Values presented range between 37 W/m and 104 W/m of borehole drilled. Assuming heating mode and a COP of 3.4, the specific peak heat extraction rates values, i.e. heat extracted or dumped in the ground, range between 26 W/m and 73W/m of borehole drilled. Although these values are available in the literature, important details regarding the GSHP operation and site-specific conditions are missing, like ground thermal properties, the thermal load imposed to the GHE, borehole spacing and interference with each other as well as the ground loop's operating temperatures, and should be taken with caution when benchmarking other solutions against them. Vertical GHE were one of the first attempts to exploit SGE, and a great amount of knowledge regarding their design, installation and operation is available.

2.3 Energy geostructures

As outlined in previous sections, GSHP systems are characterized by high investment, mostly due to the construction costs of the GHE, especially when drilling boreholes. Foundation elements such as slabs, retaining walls and piles, and underground structures like tunnels (Figure 2.10) can incorporate heat exchanger pipes without losing their main structural purpose, therefore, assuming a dual function. These types of structures are also referred to as energy geostructures and arise as an alternative to conventional GHE due to the lower costs of implementation since the heat exchanger loops are installed during the construction process that would already be required for delivering such structural elements. The additional construction cost of an energy geostructure, in comparison with a non-thermally activated solution, is relative to the labour of embedding HDPE pipes into the steel cage, to the fairly inexpensive pipes, to the heat transfer fluid, and the circuit pressure leakage test. Therefore, energy geostructures are becoming more and more relevant since they can make GSHP systems, even more, cost-competitive than conventional heating systems, thus indirectly lowering the minimum required SPF_{H4} (see Appendix A) for cost reduction compared to non-renewable energy sources.

The use of energy geostructures presents other advantages including the following:

- The concrete, used in energy geostructures, has better thermal conductivity and thermal storage capacity than the materials surrounding heat exchanger pipes in conventional GHE systems, which makes it ideal for heat exchange with the ground.
- The bending radius of HDPE pipes, in many energy geostructures, is higher than in other shallow geothermal energy systems which results in lower heat transfer fluid flow resistance and thus, lowers operational costs due to the lower energy consumption of the circulating pump.
- As with other GHE, energy geostructures allow for a reduction in the environmental impact of heating and cooling. Specifically, energy geostructures incorporate the ability to exchange heat in the structural elements thereby reducing, in a first stage, the projects construction impact and the environmental impacts during the life span of the project.

Energy walls and tunnels are subject to additional logistical and bureaucratic barriers because in some situations the final consumer of thermal energy could be a third party as opposed to energy piles that usually supply the building on top, (Loveridge et al., 2020).

Figure 2.10 - Heat exchanger pipes installed in a) energy piles, b) energy slabs, c) energy tunnels and d) energy walls, (Laloui & Rotta Loria, 2020).

2.3.1 Operation modes

Energy geostructures, as other GHE, can operate in two different modes: heat exchange and heat storage mode. In heat exchange mode, the energy geostructure can operate in heating or cooling mode through the exchange of heat with a ground that recharges its ability to supply or retain heat. This is typically the case in places where groundwater flow is non-negligible which allows the excess heat to be transported away from the structure and when heating and cooling loads are balanced.

In heat storage mode, the energy geostructure supplies the cooling needs in the summer by injecting heat from the building into the ground, often supplemented by excess heat from e.g. solar hot water panels. In the heating period, the energy geostructure extracts the heat stored by the ground in the previous cooling season to meet the heating demand of the building. This operation mode is only possible in places were no groundwater flow is present.

2.3.2 Energy piles

Energy piles are one of the most common types of energy geostructures and the technology can be installed in both driven and bored piles. First applications date back to the 1980s in prefabricated concrete driven piles with imbedded heat exchangers, followed by increased interest on the installation of heat exchanger pipes in ductile iron piles. Though, the latter have a lower energy performance than precast driven piles and bored piles due to the smaller diameter of only about 170 mm (Brandl, 2006).

Therefore, the interest was targeted to bored energy piles that due to large diameters allow multiple heat exchanger pipes to be installed, enabling a higher energy performance. According to Brandl (2006), for energy piles, the rotary bored technique should be chosen rather than a continuous flight auger (CFA) once the latter requires submerging the reinforcement cage (with welded over tied rebars for increased stiffness) in concrete with the HDPE heat exchangers attached which can result in pipe damage. As shown by Figure 2.11a, in bored piles the pipes are attached to the steel cage that is installed before concrete pouring. In the case of CFA piles, to overcome the technical difficulty described previously, it is common to plunge the pipes into the centre of the pile, attached to a recoverable steel bar to provide stiffness during insertion (Figure 2.11b).

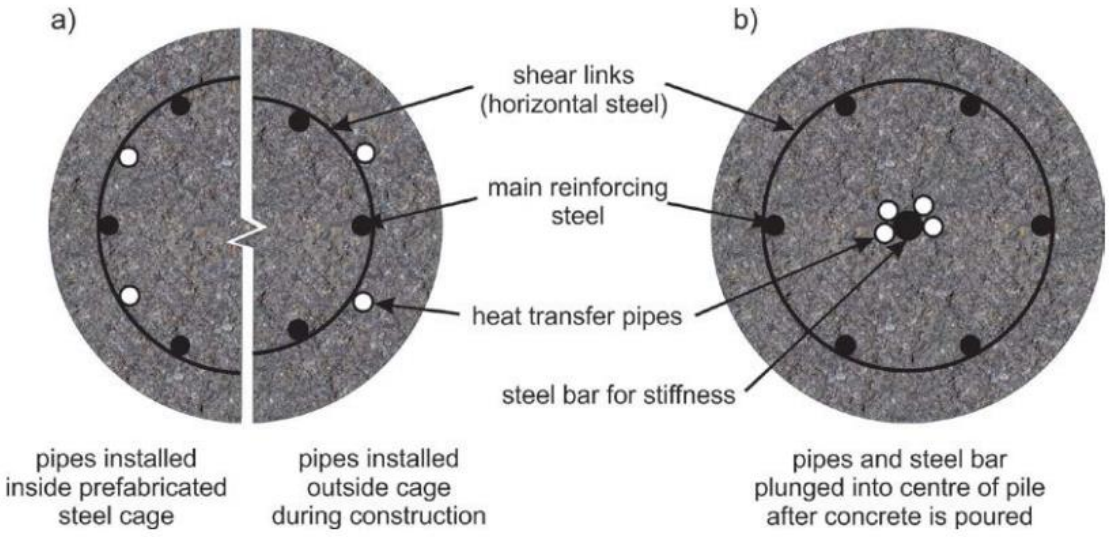

Figure 2.11 - Cross section of typical energy piles. a) bored piles: pipes attached to the steel cage; b) CFA piles: pipes installed in the centre of the pile; (Loveridge, 2012).

Typical heat exchanger pipes (Figure 2.12) are based on U-shaped pipe layouts, such as single U-pipe, double U-pipe parallel, double U-pipe cross and multi-tube, helix layout and indirect double pipe layout (coaxial).

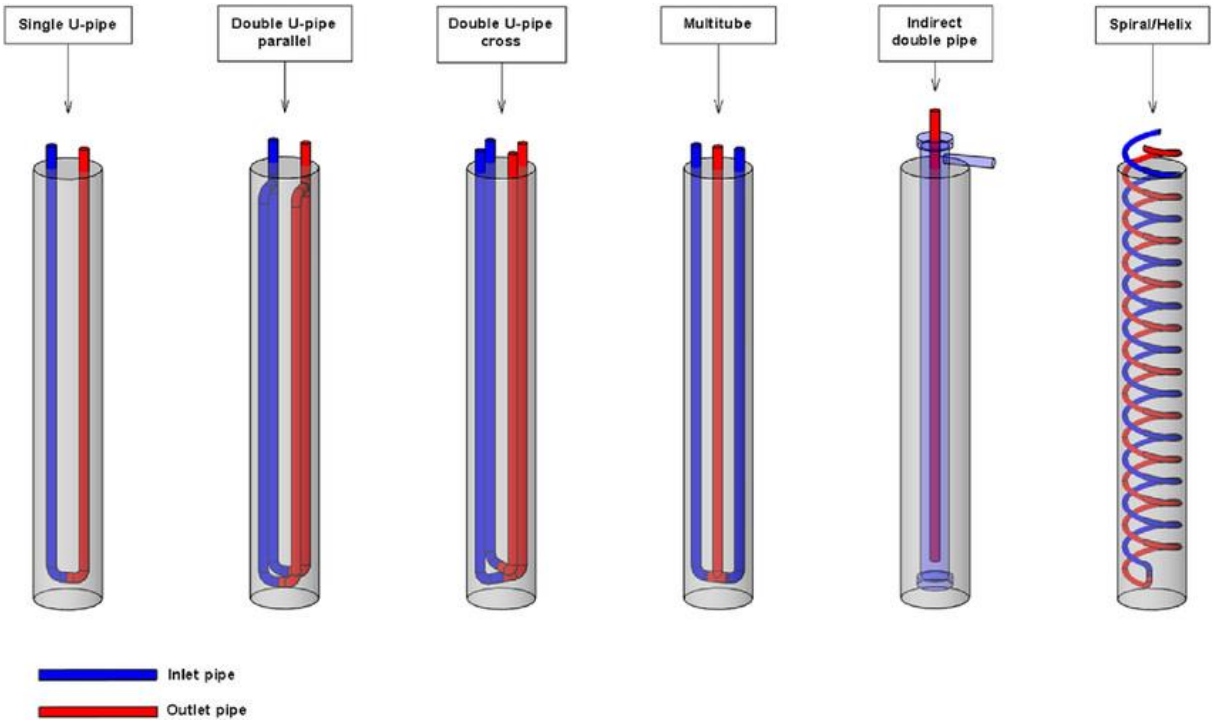

Figure 2.12 - Schematic heat exchanger pipe layouts for bored energy piles (Fadejev et al., 2017).

The thermal behaviour of energy piles has been a subject of study for several years. Piles have a geometry similar to boreholes; therefore, several analytical models are available in the literature, most of them adapted from solutions proposed for boreholes, with their limitations being well defined. As bored piles can have diameters bigger than 1 m, a large volume of concrete has to be taken into account when applying heat source models that assume a steady-state temperature field inside the pile, to calculate temperature changes in the ground. Additionally, pipe layout can vary, as shown by Figure 2.12, which makes numerical simulations using finite element methods more suitable for energy piles design as they cope better with the variability of parameters (Soga & Rui, 2016).

Loveridge et al. (2020) report that the number of pipes installed in a pile is the primary factor that contributes to greater energy performance, followed by pile length and pile thermal properties. Therefore, layouts like double U-pipe are preferred to a single U-pipe. Additionally, authors state that some studies regarding the helix layout report potential greater heat transfer rates than U-pipe layouts, mainly due to a greater pipe length.

Some long-term tests and monitoring data of energy piles were summarised by Loveridge et al. (2020). The authors found that some studies of bored energy piles reported heat transfer rates that range between 15 and 35 W/m of pile length and some few reported values ranging between 90 and 220 W/m. A relationship between the monitoring period, the pile diameter, the number of pipes, the pile length and

the heat transfer rate values is not evident which shows that without a full description of parameters, like thermal load and system operation the definition of a benchmark value is nearly impossible. The lower values are the in the range expected for energy piles while the upper values are possibly from systems with an intermittent operation or a balanced thermal load. Additionally, (Bourne-Webb et al., 2013) provides a detailed summary regarding the ground profile, the pile characteristics and the thermal parameters of already implemented projects of energy piles.

Since piles primarily function is as a foundation element, some attention as to be made to the thermal-induced changes to the mechanical behaviour of energy piles. Because a thermal load is imposed to the pile, it is expected that expansion (heating of the pile) and contraction (cooling of the pile) of the pile will generate additional compression and tensile stresses respectively, that must be evaluated. The magnitude of these stresses is dependent on the temperature variation imposed on the pile and the pile restraints, i.e. if the pile can freely move (no restraint), the expansion or contraction will not generate additional stress as opposed to a pile fully restrained in which no contraction or expansion is allowed thus generating additional stresses. Additionally, the surrounding soil is also heating and cooling, hence expanding and contracting which induces stresses in the piles, adding another layer of complexity to the evaluation of the thermomechanical behaviour. A detailed description of these effects in piles is outside the scope of this thesis which is focussed on the thermal performance of energy walls and many works have already dealt with this problem extensively, e.g. (Bourne-Webb et al., 2009, 2019; Bourne-Webb & Bodas Freitas, 2020).

2.3.3 Energy tunnels

Tunnel linings with embedded heat exchanger pipes or energy tunnels are seen as an opportunity to exploit energy not only from the ground but also from the interior space of tunnels. Like other energy geostructures, the increase of interest in the potential of energy tunnels has been driven not only by sustainability but also by the innovative component demanded in large infrastructure projects.

As with other energy geostructures, heat exchanger pipe layout and installation should be compatible with the adopted construction technique and keep the additional construction cost low. Therefore, there are two main ways to install heat exchangers into tunnel linings: by installing a prefabricated energy textile or energy fleece (non-woven geosynthetics with pipes attached) between inner and outer tunnel linings (Adam & Markiewicz, 2009), used in tunnels constructed using the NATM method, or by installing the pipes into precast lining segments for TBM excavations (Frodl et al., 2010). In the latter, the pipes are attached to the reinforcement cage before concrete casting (Figure 2.13) and arrive at the construction site ready to install, thus lowering the amount of labour required. After installation, the pipe ends are connected to the other element pipe ends to create a segment circuit that is then connected to the main pipe collector.

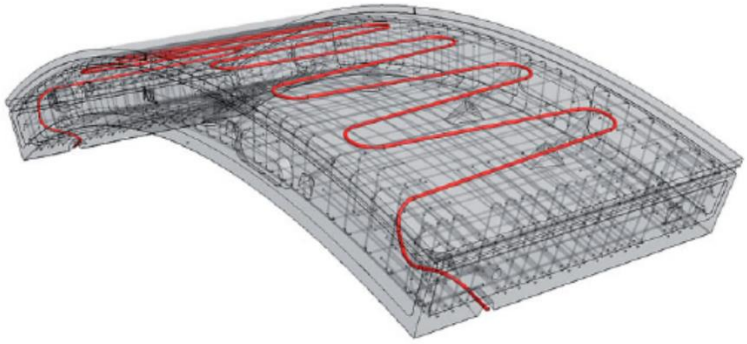

Figure 2.13 - Schematic representation of a heat exchanger pipe installed in a TBM lining segment (Frodl et al., 2010).

Pipe layouts (Figure 2.14) can be defined as longitudinal (parallel to the main tunnel axis), transversal (perpendicular to the main tunnel axis) or slinky, although with applications only in energy textiles (Loveridge et al., 2020).

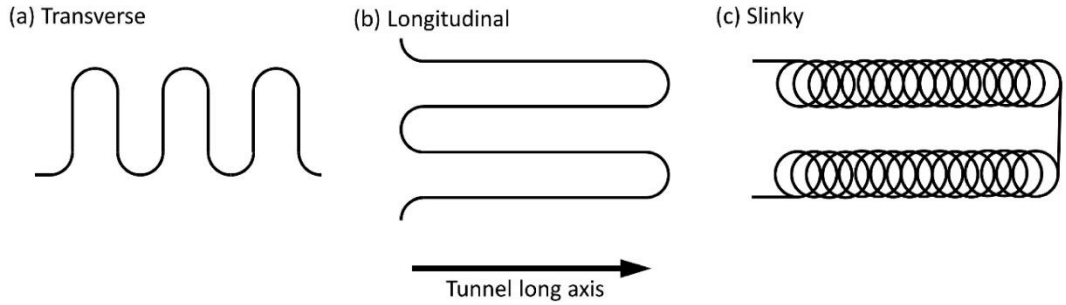

Figure 2.14 - Energy tunnels absorber pipe layouts (Loveridge et al., 2020).

In vertical borehole heat exchangers and energy piles, the ground is the only heat source and sink. In energy tunnels, the interior space of the tunnels is also an energy source. Properly defining this additional boundary condition (BC) between the tunnel lining and the internal air space is critical for a correct thermal output evaluation. Two types of tunnels can be identified depending on their thermal behaviour: “Cold tunnels” are tunnels with similar internal temperature as the surface air temperature due to short length or to ventilation. Conversely, “hot tunnels” refers to tunnels that due to internal activity and lack of ventilation exhibit higher internal air temperature than the surface air temperature (Soga & Rui, 2016), as is the case in some metro tunnels. The internal environment of metro tunnels can be a great heat source due to the heat generated by trains and passengers. Nicholson et al. (2013) report that every London Crossrail train emits 1 MW of heat plus 0.1 MW from air-conditioning, which correlates to 22 W/m^2 at peak times and 13 W/m^2 at the tunnel lining on a weekly average. Additionally, train movement can induce convective heat transfer, even in “hot tunnels”, which adds another layer of complexity when defining this BC.

As with other emerging energy geostructures, there is still a lack of published data, mainly monitoring data from implemented projects that could be used to complement and validate analytical, numerical and scale models. Although, some studies are available and several conclusions can be established.

Tinti et al. (2017) developed an analytical model to evaluate energy and economic feasibility of a possible installation of an energy tunnel lining into a drill and blast excavated tunnel located on the Italian Alps. A maximum of 560 kW thermal output was estimated from 32 pipelines of 330 m each alongside a 73% cost reduction compared to borehole heat exchangers for the same thermal power. Although it is highlighted that the lack of potential users near the mountain tunnel can compromise the utilization of such amounts of thermal energy. A COP variation between 3.9 and 5.1 along the year is achievable for low enthalpy district heating system with 50 users.

Regarding field tests, Buhmann et al. (2016) conducted a thermal performance test on two 10 m long tunnel lining segments with a surface area of 360 m^2, in a tunnel located in Stuttgart. The pipes were installed in a longitudinal layout between the inner and outer tunnel linings and no groundwater flow was registered around the tunnel. The test was conducted for 6 months (April to October) in cooling mode, with almost constant inlet temperature. The heat transfer rate values exhibit a reducing trend from 30 W/m^2 to 5 W/m^2 as the tunnel air temperature increased, with values of 20 W/m^2 being reported for an additional intermittent operation heating test (constant inlet temperature for 8 hours a day). The authors conclude that the tunnel inner space temperature is the main influence on the thermal performance of the system followed by an optimized operation and accurate energy demand profiles that can substantially increase heat transfer rates.

Lee et al. (2016) describe a field thermal performance test of six energy textiles with longitudinal, transverse, and slinky pipe layouts, installed in an abandoned tunnel in South Korea. The long-term monitoring tests were performed with an 8 h thermal operation and 16 h rest period to simulate the energy load of an office building. They found that higher heat transfer rates were achieved in cooling operation (layout average of 435.7 W) than in heating operation (layout average of 88.8 W) due to higher temperature differences between the inlet and tunnel air in the summer (from 10.2ºC to 15.6ºC, than in winter (from 0.3ºC to 6.8ºC) which is in agreement with the German tunnel tests (Buhmann et al., 2016). Additionally, heat transfer rates range from 4 to 6 W/m^2 (heating) and 24 to 34 W/m^2 (cooling) for the transverse layout, 5 to 10 W/m^2 (heating) and 24 to 28 W/m^2 (cooling) for the longitudinal layout and 11 W/m^2 (heating) and 37 W/m^2 (cooling) for the slinky layout based on a 1.5 m high and 10 m long energy textile panel.

Frodl et al. (2010) reports the design, approval and construction details of a TBM tunnel lining segment equipped with heat exchanger loops to provide heating to a town council in Germany. The 54 m thermally activated segment consisted of 27 rings of energy segments (7 segments each), each with 175 m of pipe installed (25 m for each segment) in a longitudinal layout. Franzius & Pralle (2011) report a field test for a set of segments in the same tunnel. The test was conducted in a semi-circular activated surface of 5 segments and 60 m^2 of area. As stated previously, in TBM energy tunnels, each lining segment loop ends are connected to the adjacent lining segments to form a bigger ring loop. To perform the field test, the segments were connected by the lining exterior to activate only the ones required to form the

semi-circular surface. The authors reported a heat flux of 10 to 20 W/m^2 which relates to a supplied heat demand of 40 kW by the 54 m tunnel segment.

Besides analytical models and field tests, numerical models have also been implemented to study thermally-activated tunnel linings. Barla & Di Donna (2018) established some impacts of ground conditions on the heat transfer. The first being that by changing the soil thermal conductivity from 0.9 to 3.9 W/mK, the amount of heat exchanged can be doubled; the second being that groundwater flow can multiply by 3 to 8 the amount of heat exchanged by increasing the flow rate from 0 to 2 m/d. Additionally, Barla et al. (2016) developed a finite element model to study the possible installation of active tunnel linings in a metro tunnel under construction in Torino. The model consists of a 1.4 m wide TBM precast lining element with embedded heat exchanger pipes that due to perpendicular groundwater flow to the tunnel main axis, was assumed to not thermally interfere with the surrounding elements. The results output a heat exchange between 53 and 74 W/m^2 in winter and summer, respectively, and a power output of 2822 kW (heating) and 3756 kW (cooling) considering a full-length (1350 m) activation of the tunnel. In terms of cost, technology implementation would represent an estimated overall cost increase of less than 1%.

Energy tunnels therefore have the potential to deliver great amounts of thermal energy with a relatively small investment. City-scale planning is needed since energy tunnels are favourable for direct supply of buildings and for being incorporated into district heating and cooling systems. Though, connecting the tunnel system to the surface distribution systems cost effectively is still a challenge that must be overcome (Barla & Di Donna, 2018; Nicholson et al., 2013).

3 Energy walls

3.1 Introduction

As mentioned previously, energy walls are thermally-activated foundation elements with large heat transfer potential due to the large surface area. Like energy tunnels, there are still few implementations of this technology which results in scarce monitoring data to evaluate the thermal and thermal-mechanical behaviour, and to validate analytical and numerical models. Laloui & Rotta Loria (2020) reviewed the number of applications of the different types of energy geostructures by surveying companies involved in the construction of these geostructures and from data available in literature. Therefore, 157 energy pile, 17 energy wall, 7 energy slab and 11 energy tunnel projects were reported (Figure 3.1) which shows that energy piles are by far the most used application, followed by energy walls. Therefore, a better understanding of the thermal behaviour of energy walls will certainly allow for an increase in the number of projects implemented.

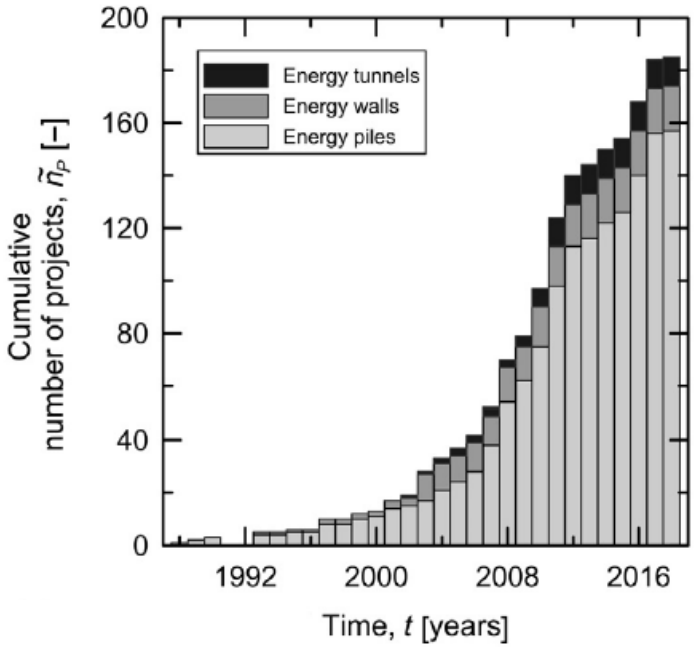

Figure 3.1 - Cumulative number of energy geostructure projects globally (Laloui & Rotta Loria, 2020).

Heat exchanger pipes can be installed in both diaphragm walls and piled walls. The latter can be divided into secant, tangent or contiguous pile walls, with spacing between piles assuming a strong influence on the system efficiency (Brandl, 2006). Although being classified as thermally-activated retaining walls, pile walls and diaphragm walls differ in geometry which impacts not only their thermal behaviour but also the heat exchanger pipe layouts which on energy pile walls are similar to the pipe layouts of energy piles (Figure 2.12), except that the pipes may only be installed on the side of the pile in contact with the ground.

Diaphragm walls allow for greater pipe layout flexibility due to their longitudinal development, as shown in Figure 3.2. Though the choice of pipe layout must take into account not only the additional heat exchanged provided by greater pipe length but also the additional circulating pump energy costs for ensuring turbulent flow on layouts with higher hydraulic head losses. Additionally, the impact of pipe arrangement and spacing on the thermal performance of energy walls will be discussed based on reported numerical analysis and field tests presented in the following sections.

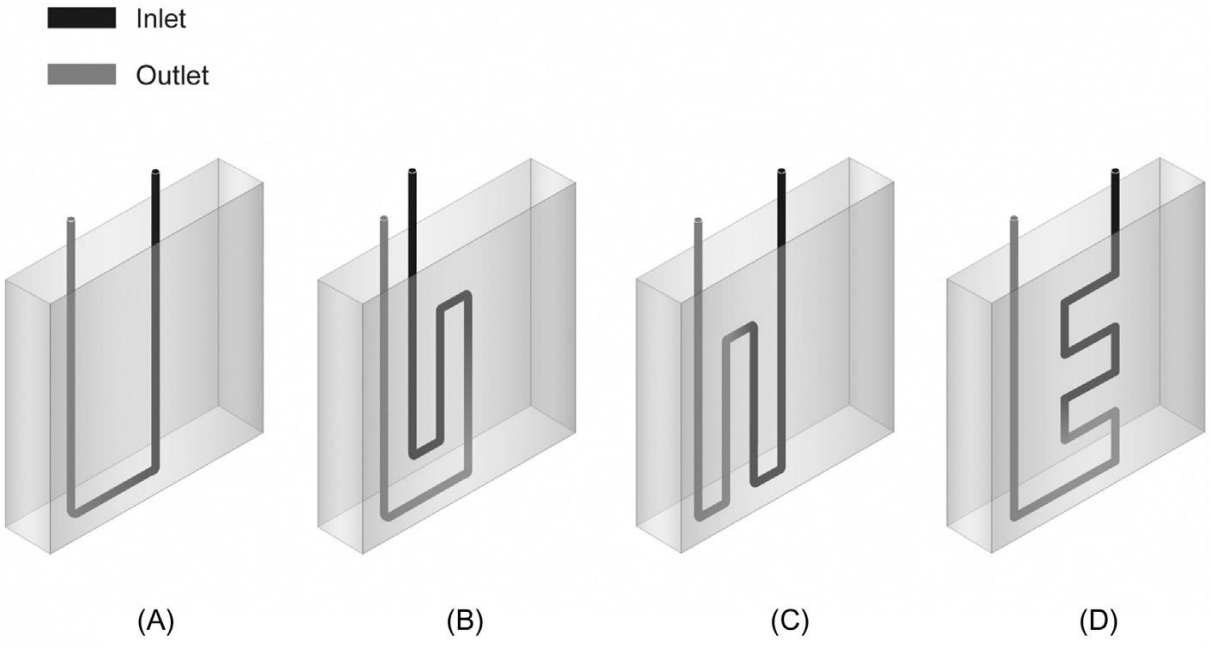

Figure 3.2 - Schematic pipe layouts in energy walls: a) U-shaped pipe, b) bent U-shaped pipe, c) W-shaped pipe and d) repeatedly bent pipe (Laloui & Rotta Loria, 2020).

As in bored energy piles and TBM tunnel linings, the heat exchanger pipes in energy diaphragm walls are attached to the reinforcement cage, which can be done either at a pre-fabrication plant or on-site. They are usually made of HDPE, with an outer diameter of 10 to 40 mm and a wall thickness of 2 to 4 mm and are located inside the reinforcement cage, to ensure a proper concrete cover, facing the groundside (Laloui & Rotta Loria, 2020). Although, as reported by Amis et al. (2010), the cage dimensions can be adapted to accommodate the heat exchanger pipes outside the reinforcement cage (Figure 3.3), i.e. increasing the cage cover to maintain the required cover to the loops, which improves safety and the constructability of the cages, especially where cage sections are joined as they are inserted into the wall panel.

Additionally, the heat exchanger pipes exit the diaphragm walls via the base slab or, more usually, via the capping beam (Figure 3.3). In the latter, the space required for the pipes must be taken into account in the design (Bourne-Webb et al., 2013) and pipes can be insulated to minimise heat losses/gains due to lower/higher temperatures at the surface (Laloui & Rotta Loria, 2020).

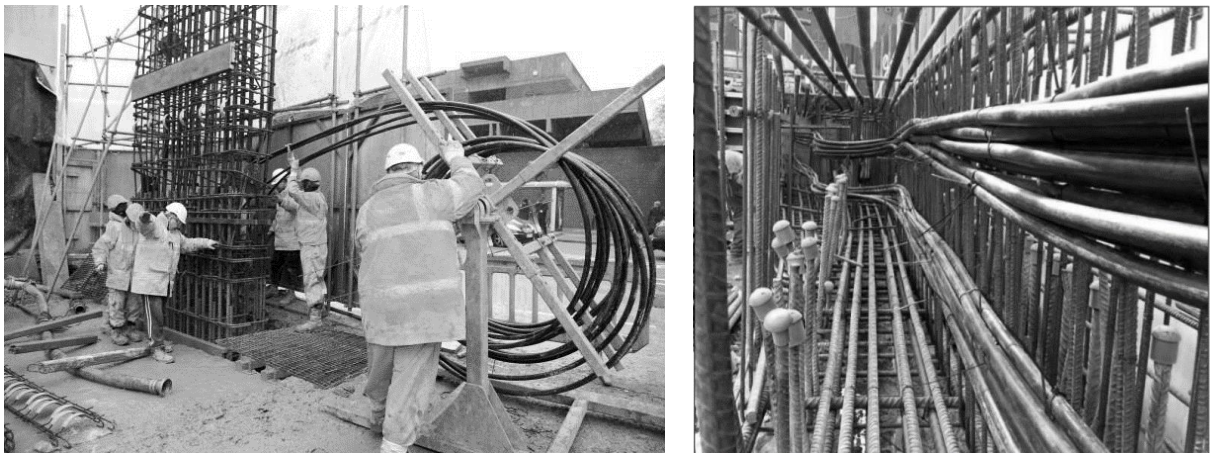

Figure 3.3 - Energy walls construction. Right: pipe installation during reinforcement cage lowering (Amis, 2010), Left: Pipes routed through capping beam (Bourne-Webb et al., 2013).

3.2 Field monitoring data

There is a lack of long term monitoring data regarding the thermal behaviour of energy walls. Although, there are some reports in the literature regarding energy wall project implementation and overall thermal performance, e.g. diaphragm wall of a metro station in Vienna and a cut and cover tunnel bored pile wall (Brandl, 2006), a residential building basement diaphragm wall (Adam & Markiewicz, 2009) as well as the monitored mechanical behaviour of an energy diaphragm wall (Soga et al., 2015). The following subsections will focus on additional selected projects available in the literature.

3.2.1 Bulgari hotel, UK

The Bulgari Hotel in Knightsbridge was the first project in the UK to incorporate energy diaphragm walls as a geothermal heat source. Amis et al. (2010) reported the iterative process undertaken by the geothermal, structural and contractor teams to deliver the project. The building consists of 10 raised floors and 6 levels of basement. The diaphragm walls consist of 39 panels (800 mm thick and typically 3300 mm long) that extend to a depth of 36 m below ground level to retain a 24 m deep excavation and to support vertical load, in some panels. The ground profile was characterized by 3 m of fill, 4.5 m of silty clay, 6.5 m of River Terrace Deposits and the London Clay Formation that extends below diaphragm wall toe (Bourne-Webb et al., 2013). The groundwater level was located 10 m below ground level.

The geothermal system comprises 49 energy piles and 100 linear meters of energy diaphragm walls that were designed to output 150 kW of heating and cooling. It was not possible to include heat exchanger pipes in all diaphragm wall panels (approx. 155 linear meters) due to deep basements in adjacent buildings. Though, the additional diaphragm wall depth required for supporting vertical load in some panels, allowed for extra heat transfer area.

The initial heat exchanger pipe arrangement (Figure 3.4) raised some concern due to the complex pipe geometry, and potential reinforcement cage attachment and pipe connection problems. The designer

and contractor with long experience in delivering energy pile projects reviewed the pipe layouts which lead to the adoption of a less complex U-pipe layout. Figure 3.4 also shows a panel cross-section with the two ground loops attached to the outer face of the reinforcement cage which lead to changes in the reinforcement layout to accommodate a 75 mm concrete cover from the pipes. As the heat exchanger pipes were installed on only one side of the wall, unlike energy piles surrounded by the ground, the designers adopted very conservative thermal values and two thermal response tests were defined to verify them. The first test was performed after diaphragm wall construction and the results validated the conservative values adopted, while the second test was performed after excavation and returned a 13% decrease in thermal conductivity, considerably less than expected (Amis, 2011).

The geothermal design aimed to not disturb in any major way the panel construction time and sequence. Therefore, with the final pipe arrangement, the teams were able to install and pressure test the loops while reinforcement cages were being lowered and joined together, and while tremie piles were installed for concreting, respectively. Ultimately, this project shows that energy diaphragm wall projects can be delivered without additional delays, in demanding site conditions, and that the coordination between the different stakeholders is essential to provide an efficient design. Additionally, although analyses were undertaken to maximise heating and cooling output, the details and results of such analyses were not presented by Amis (2011) and Amis et al. (2010).

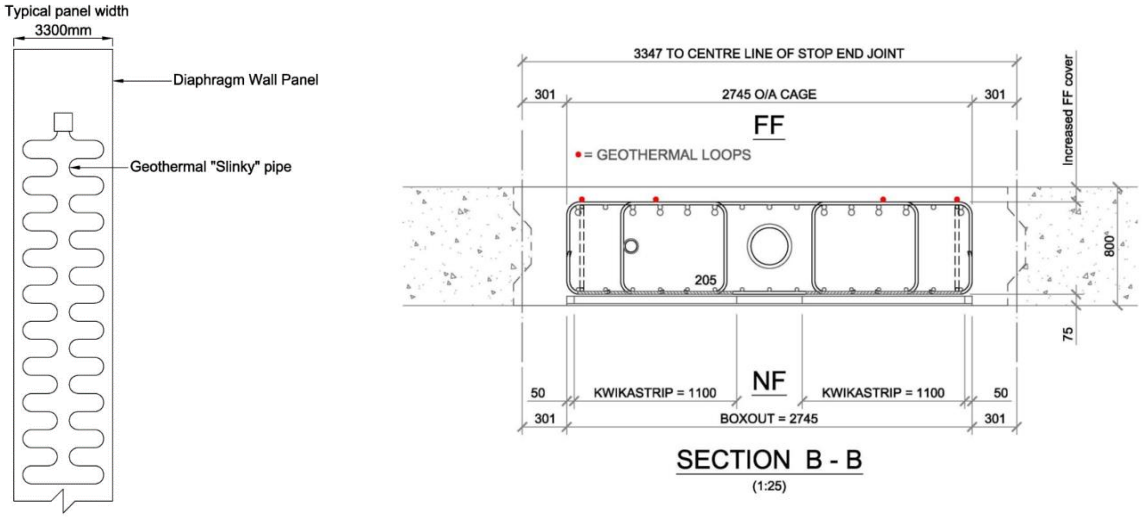

Figure 3.4 - Heat exchanger pipe arrangements. Left: schematic initial pipe arrangement; Right: diaphragm wall cross-section with the final arrangement of two loops (Amis et al., 2010).

3.2.2 Shanghai museum of natural history

The Shanghai Museum of Natural History is a public building in China with thermally-activated foundation elements. Specifically, heat exchangers were embedded in the piles under the base slab and in the diaphragm walls of both the museum and the Shanghai metro line 13, which runs underneath. There are 452 W-shaped heat exchangers, embedded in the diaphragm walls, with depths of 30 to 38

m. Each W loop consists of two U-shaped loops connected in series, with a pipe diameter of 25 mm and pipe wall thickness of 2.3 mm.

To implement an efficient geothermal design with maximised heat exchange, a field thermal performance test was carried by a constant temperature method, i.e. constant inlet temperature for both heating and cooling, at three diaphragm wall panels (each 38 m deep and 1 m thick) with three different heat exchanger layouts (Figure 3.5). The excavation depth was 18.5 m and during the tests, the base slab was under construction, while the waterproofing layer and inner lining wall were not installed yet. Four groups of tests were performed to assess the impact of the heat exchanger layout, heat transfer fluid velocity (water) and inlet temperature, and operation mode on the heat transfer rate. Table 3-1 presents the details of the parameters that were subject to study in the performance tests. At the beginning of the test, the average temperature of the diaphragm wall was reported as 23.0ºC and the average soil temperature was 16.3ºC.

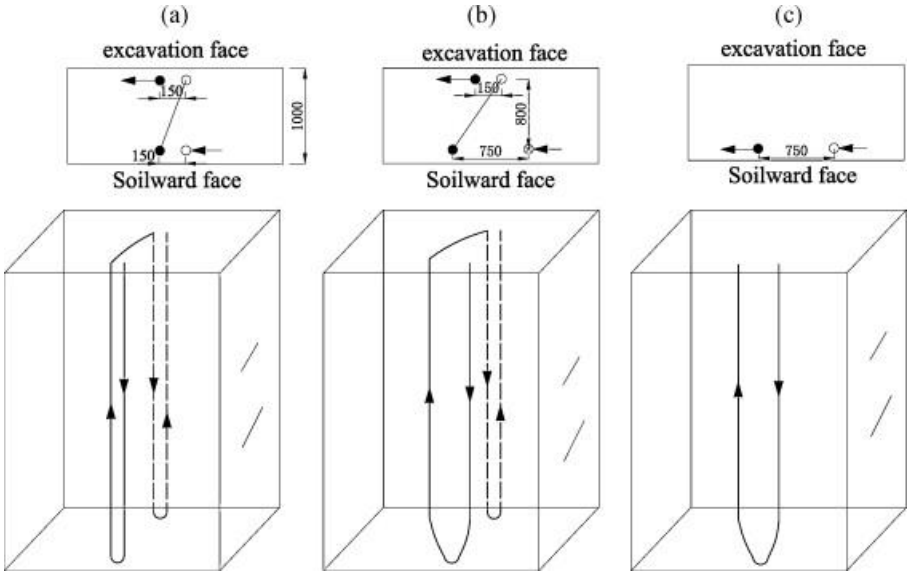

Figure 3.5 - Experimental pipe heat exchangers arrangements. a) W-shaped, b) improved W-shaped, c) single U-shaped (Xia et al., 2012).

Table 3-1 - Experimental schemes of the performance test (Xia et al., 2012).

No.	Influence factors	Factor levels	Other conditions
1	Heat exchanger types	Tubes type (*a*), (*b*), (*c*)	Velocity 0.6 m/s; inlet temperature 35 °C
2	Water velocity (m/s)	0.25, 0.45, 0.6, 0.75, 0.90, 1.05, 1.30, 1.5	Tubes type (*b*); inlet temperature 7 °C
3	Inlet water temperature (°C)	32.0, 35.0, 38.0	Tubes type (*a*), (*b*), (*c*); velocity 0.6 m/s
4	Operation modes	Intermittent operation (1:1), Continuous operation	Tubes type (*b*); velocity 0.6 m/s, inlet temperature 35 °C

From the results, one can conclude that: the heat transfer rate of the W-shaped loops is 25% to 40% higher than the U-shaped loop, under the same conditions (illustrating the benefits of additional pipe

length), and that the increase in spacing between pipe branches on the side facing the ground, i.e. from arrangement a) to b), results in 11% higher heat transfer rates (showing that pipe spacing needs to be optimised to prevent pipe to pipe thermal interference); there is a great increase of the heat transfer rate with the increase of velocity until 0.9 m/s, after which stays relatively constant (turbulent conditions are optimal for heat exchange); there is an almost linear relation between the inlet temperature and the heat exchange rate, with an increase of 1ºC resulting in an increased heat exchange rate by 15%, and an intermittent operation mode (12 hours running and 12h stopped) improves the heat transfer rate by almost 15% compared to a continuous operation.

3.2.3 Residential building in northern Italy

Angelotti & Sterpi (2018) report some details of a building in northern Italy consisting of six above ground and three basement floors, with thermo-active foundation elements (diaphragm walls and base slab) and two groundwater wells forming an additional open-loop system. The latter are only used when the thermo-active foundation elements do not cope with the energy demand. Additionally, the seasonal operation mode of the system allows for space heating and domestic hot water production in the winter, and space cooling and domestic hot water production in the summer.

There are 66 no., 2.4 m long, 0.5 m thick, and 15.2 m deep panels, resulting in 160 linear meters of diaphragm wall (four sides of 40 m each) to retain an excavation height of 10.8 m. Each diaphragm wall panel contains two HDPE heat exchanger loops and a free central space (0.8 m wide) to allow for the installation of 10 m long anchors at two levels (Figure 3.6). The loops are attached to the reinforcement cage on the soil side only and consist of six vertical pipe segments over a width of 800 mm resulting in an average pipe spacing of 160 mm and a total pipe length of 90m. A concrete cover of 50-80 mm to the pipes was provided. The total heat exchange area (walls and base slab) is about 4065 m^2, with two thirds being exposed to the internal excavation environment.

To evaluate the heat transfer rates of the thermo-active foundation elements and heat pump, as well as the system efficiency, the mass flow rate, inlet and outlet heat transfer fluid temperatures, and heat pump electricity consumption were monitored in the first months of operation (December to March), i.e. short-term monitoring data. The authors reported a monthly average heat transfer rate between 12.5 and 14.9 W/m^2 for the diaphragm walls, which correlates to 30 to 35.8 W/m of wall depth, in agreement with the values of the short-term performance test from Xia et al. (2012). Additionally, the COP for both space acclimatization and domestic hot water shows a decreasing trend from a maximum of 5.0 in December to a minimum of 4.2 in March that the authors attribute to the extended heat exchange operation and to the increasingly intermittent operation of the system approaching March.

Temperature sensors were installed at various depths (Figure 3.6), on both the excavation side and soil side of the wall, along the anchors in the soil behind the wall and at heat exchanger loop centre (section x=0.8 in Figure 3.6). From the temperature data collected, it was possible to conclude by the difference in temperature between wall faces, that the basement environment contributes negatively to the heat

transfer, i.e. in heating mode the basement environment withdraws heat from the heat exchanger loops (i.e. the basement is cooler), and the opposite occurs in cooling mode (the basement is hotter). Conversely, the ground around the buried part of the wall always acts as heat source in the winter and as a heat sink in the summer.

Additionally, Sterpi et al. (2018) report some more details regarding the thermal behaviour of the energy wall. It is added that the conditions on the inner lining of the basement changes, i.e. one side of the basement has a 0.5 to 1 m air gap in contact with the ground surface air, while other parts have a similar gap but without contact with ground surface air, others are in direct contact with the basement environment and lastly the part that delimits the garage ramp contacts with the air by way of a central shaft. Although no details are given regarding the type of inner lining on the wall panel presented, it is stated that the temperature at the excavation side of the wall is very close to the ground surface air temperature in the winter and slightly below in the summer.

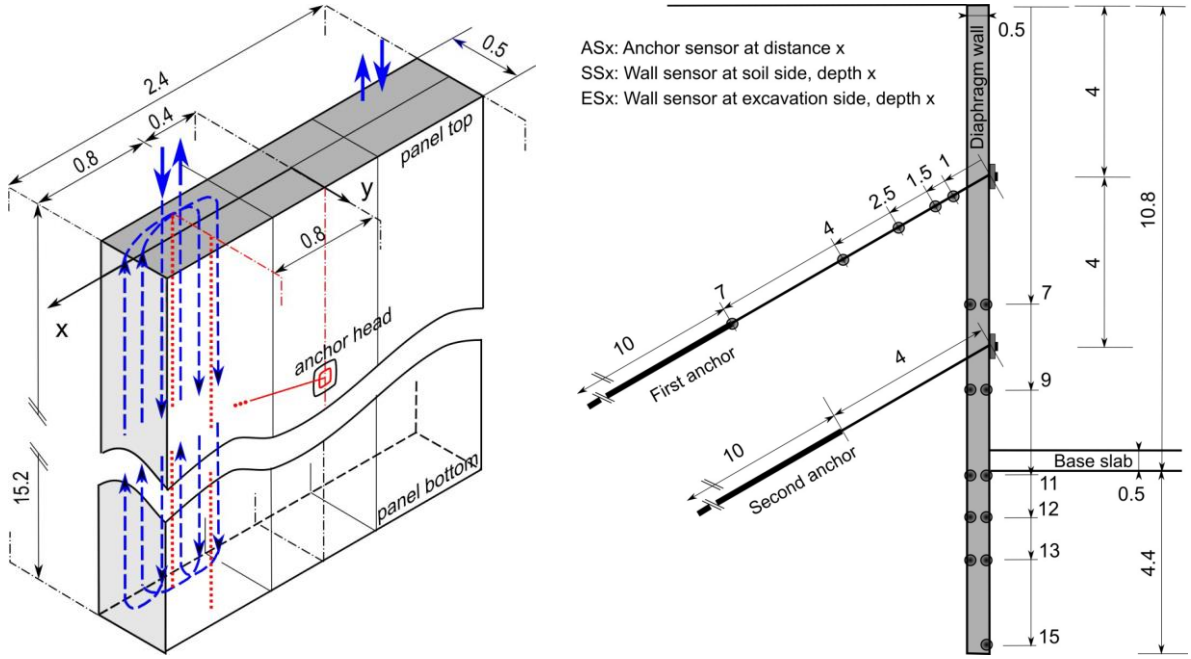

Figure 3.6 - Diaphragm walls. Left: schematic representation of a single diaphragm wall panel with one of two heat exchanger loops; Right: Anchors cross section with the temperature probes (dots); (Angelotti & Sterpi, 2018).

3.2.4 Model scale test

Kürten et al. (2015) developed a model scale test of an energy wall installed in a box with a base area of about 3m × 3m and 2m of height. The test model consists of two independent circuits, the “inner cycle” and the “outer cycle” (Figure 3.7). The former controls the inlet temperature and mass flow rate in the heat exchanger pipes whereas the latter controls the ground temperature and groundwater velocity. This allows for different BC and parameters to be tested. The groundwater flow direction was

defined as parallel to the wall to prevent “flow dead zones” closer to the wall (as illustrated by Figure 3.7) which results in lower influence of groundwater flow on the wall energy performance.

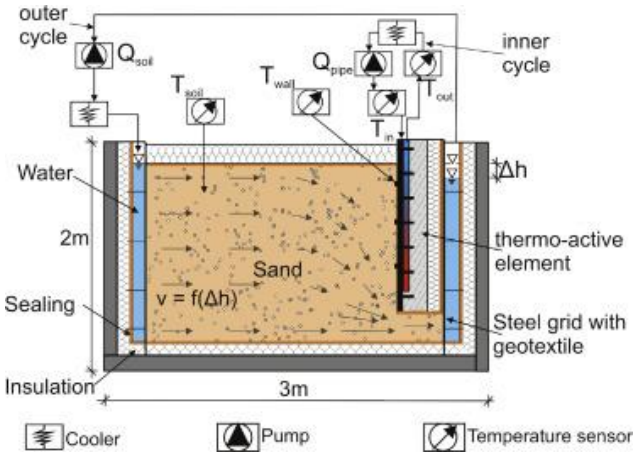

Figure 3.7 - Scheme of the model scale test (Kürten et al., 2015).

The wall contained both U and W-shaped heat transfer loops with outer diameter of 25 mm and inner diameter of 20 mm. The arrangement of the loops (Figure 3.8) prevents interference as only one of the sets of geometries (U1 and U2 or W1 and W2) were tested at any time. The results show that the pipe length is more important than the pipe arrangements, and relatively high values of heat transfer rates, ranging between 36 W/m^2 and 150 W/m^2, were reported possibly due to the short duration of the test (6 to 10 hours). Authors also report that the specific power, the heat power normalised to the pipe length, seemed independent from the groundwater velocity. Actually, no significant differences were found by increasing the groundwater flow velocity. The authors point out that the limited impact of groundwater is due to the short pipe lengths used in the laboratory test, as the relative low time that the fluid is in contact with the element prevents a greater influence of groundwater.

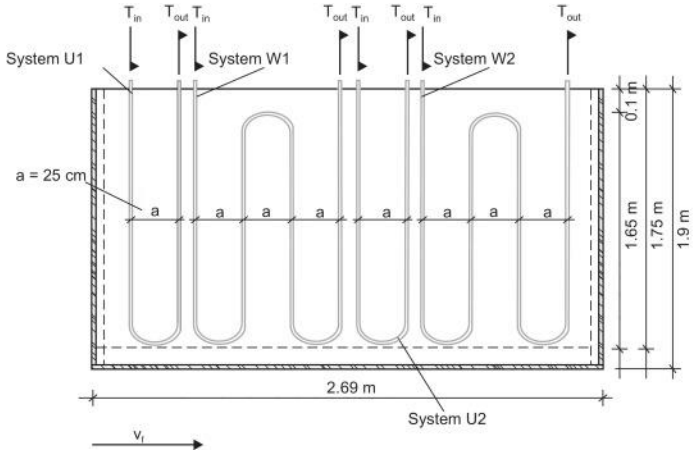

Figure 3.8 - Heat exchanger loops of the model scale test (Kürten et al., 2015).

3.3 Numerical analyses

Numerical analyses are the most common method to assess the thermal and mechanical behaviour of energy walls, not only because of the increase of interest in energy walls but also due to the lack of monitoring data. A number of studies have shown that the observed thermal response of energy piles

can be reproduced numerically, so the use of numerical analysis to study energy walls seems reasonable, even in the absence of good observational data to allow validation. There are now a number of numerical studies available in the literature that seek to better understand the impact of a range of parameters on the thermal performance of energy diaphragm walls.

Barla et al. (2020) reported a numerical study aiming to assess the most efficient heat exchanger layout and heat transfer fluid velocity. They conclude that a horizontal type configuration (or repeatedly bent pipe as seen in Figure 3.2 d)) is favourable for heat performance maximisation and that the fluid velocity does not impact in a significant manner the heat exchange. On the other hand, Makasis & Narsilio (2020) state that vertical heat exchanger loop configurations show a performance increase over horizontal configurations, mainly in walls with less than 10 m depth. Additionally, horizontal configurations are found to be more expensive in terms of material and labour costs, and vertical configurations can result in delays due to the execution of the pipes connections between diaphragm wall sections, which is in contrast with the project detailed in Section 3.2.1 where the pipes were arranged on the outside of the cage to avoid exactly this issue.

The impact of ground conditions on the heat exchange output of energy walls was assessed by Di Donna et al. (2020). The study focused on three parameters: the undisturbed ground temperature, the groundwater flow velocity, and the soil bulk thermal conductivity. A wall panel 20 m in depth, 2.5 m wide and 1 m thick, with a w-shaped heat exchanger loop installed in the soil side of the wall, was implemented in a model with 60 m height, 2.5 m width and 120 m length (to consider the groundwater effects perpendicular to the wall). Additionally, a constant temperature (10ºC in winter, 20ºC in summer) and a convective heat BC (convective heat transfer coefficient (h) of 2.5 W/m^2K) were applied to the exposed wall face, resulting in a decrease of efficiency of 10% to 12% relative to the constant temperature BC, reported as a reference case (without groundwater flow). Regarding the three parameters considered in the study, the authors report a rise from 9 to 27 W/m^2 by increasing the absolute temperature difference from 4ºC to 20ºC between the initial soil temperature and the inlet temperature. In addition, by increasing the groundwater flow velocity from zero to 2 m/day or the soil thermal conductivity from 0.9 to 3.9 W/m K (without groundwater flow), a 150% or more increase in heat output is achievable. Though, it is unclear how these percentage increases were computed since the data reported do not support them. Moreover, Makasis & Narsilio (2020) state that the ground thermal conductivity impacts the thermal performance, specifically in shallow walls, but to a lesser degree than the wall depth. However, these analyses were performed considering insulation between the exposed part of the wall and the interior space, which means that the soil thermal conductivity will have a greater effect as the heat can only be absorbed by the soil. Makasis & Narsilio (2020) also conclude that the optimal pipe spacing is independent from the soil thermal conductivity and that there is no performance gains to be made by implementing a pipe spacing lower than 300 mm, confirming what was reported by Adam & Markiewicz (2009). In fact, the heat exchange is less impacted by the pipe spacing in deeper walls than it is in shallow walls (depth less than 20 m). Balanced thermal loads can allow for larger pipe spacing and thus, less total heat exchanger pipe length.

3.3.1 2D steady state analysis

Bourne-Webb et al. (2016) reported a 2D steady state thermal and thermo-mechanical analysis of an energy wall installed in a tunnel. The thermal analysis aimed to evaluate the effect of the BC of the exposed face of the wall, namely the observed difference on the heat transfer rate between a constant temperature boundary and a convective boundary.

For the thermal analysis, a diaphragm wall panel slice was defined as shown in Figure 3.9. Two pipe loops were considered, one on the soil side and the other on the excavation side of the wall, and were simulated as holes in the mesh with a 27ºC (summer) constant temperature BC. The adiabatic BC indicated (Figure 3.9) constrain the heat flux to the horizontal plane whereas the right-hand boundary parameters changed from a constant temperature of 15ºC, representing a very large air-speed in contact with the wall face, to a convective boundary with the same air temperature combined with convective heat transfer coefficients of 2.5 W/m^{2}K, 12.5 W/m^{2}K and 25 W/m^{2}K representing air-speeds of near-zero, 0.5 m/s to 2 m/s and 3.5 m/s to 5 m/s, respectively.

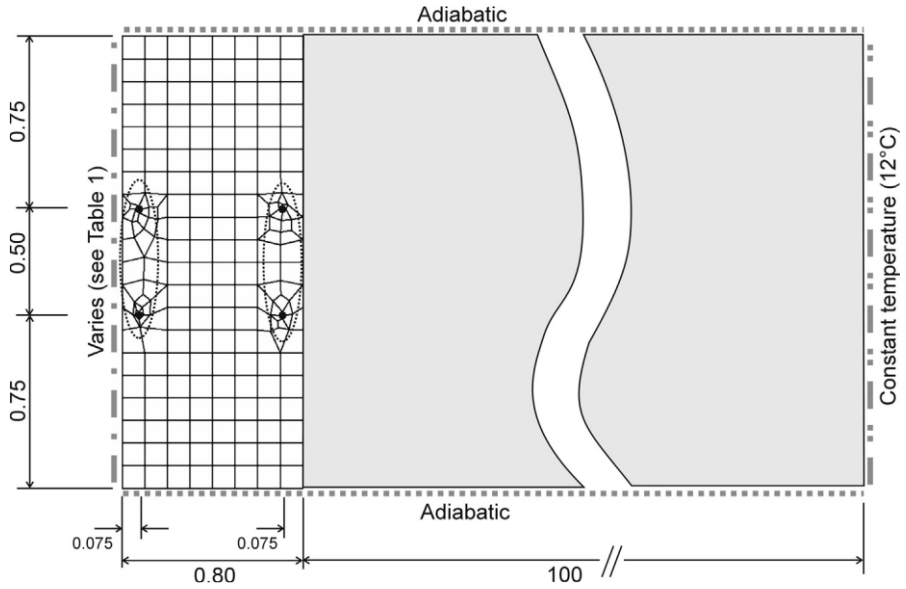

Figure 3.9 - Diaphragm wall panel geometry and boundary conditions (Bourne-Webb et al., 2016).

The results of the study showed that the climatic conditions in contact with the wall have a great influence on the heat transfer. It was observed that the heat transfer rates to the tunnel side were much higher (12 to 21 W/m^2 for soil side loop only; 20 W/m^2 – 79 W/m^2 for both loops) than the ones for the soil side (less than 1 W/m^2 for the soil side loop only and for both loops), thus the warm interior space was acting as the main heat source, which might be adequate for heating but not cooling. Additionally, the constant temperature BC and the lower convective heat transfer coefficient result in the highest and lowest heat transfer rates, respectively. Therefore, applying a constant temperature BC could lead to a non-conservative design. Though, the authors point out that the performed steady state analyses could not represent in the best way the long-term behaviour of a true transient problem such as energy walls. In fact, Loveridge et al. (2020) reports much lower heat transfer rate differences between constant temperature and convective BC from transient analyses.

3.3.2 Heat exchanger layout optimisation based on monitoring data

Sterpi et al. (2020) performed a numerical simulation for design optimisation based on monitoring data. Firstly, the authors compared the heat transfer rates from the energy diaphragm walls of the residential building detailed in Section 3.2.3, based on field data, against values presented in the literature. From that, it is established that the part of the wall above the base of the excavation behaves differently, and worse, than the buried part due to the heat exchanger pipes layout (Figure 3.6) that run consecutively above and below the excavation level, possibly disregarding the better performance of the buried part of the wall. Additionally, the authors point out that the inlet and outlet pipe branches are closer, and the spacing between branches lower, than the examples of Bourne-Webb et al. (2016) and Xia et al. (2012).

Therefore, a numerical model was created, aiming to assess the possible pipe thermal interference, in a first stage, and the potential heat exploitation from the buried part of the wall, in a second stage, thus leading to a more efficient pipe layout. The finite element method was used to perform the numerical analysis of a three-dimensional (3D) model, 1.2 m wide, that corresponds to half of a single panel (Figure 3.10 a))

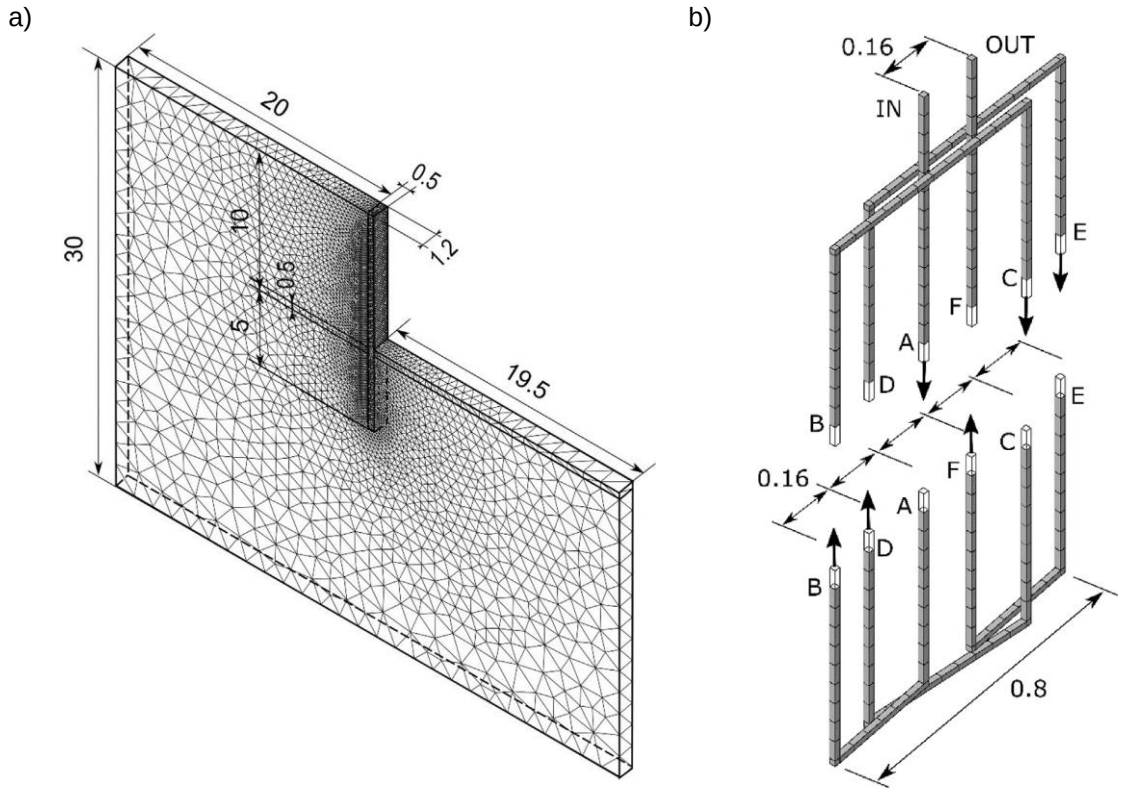

Figure 3.10 - Geometry, dimensions and finite element meshes: a) modelled domain, b) Initial heat exchanger pipe layout (Sterpi et al., 2020).

Regarding BCs, an adiabatic condition was assigned on the front and back faces of the model (symmetry planes) as well as on the right lateral boundary (central symmetry plane of the excavation) and left lateral boundary, considered far enough from the energy wall to be undisturbed by temperature variations. On the ground surface (top boundary) a temperature profile reproducing the monitored surface temperatures was applied, and at the wall face and excavation base, a time-varying BC with a damping

coefficient of 0.66 applied to the surface temperatures profile was assigned (no convective heat transfer) to consider the expected temperature difference between the interior space and the exterior air temperature. A 13.4ºC constant temperature BC, equal to the surface yearly average temperature, is assigned to the bottom face of model.

The heat exchanger pipe layout (Figure 3.10 b)) for the numerical model results from the real pipe layout (Figure 3.6) after some simplifications: the internal circular section of the pipe is replaced by a square section with similar area, the HDPE material is neglected and the bends on the pipe edges are replaced by square corners. Additionally, the saturated soil thermal properties were estimated based on the individual thermal properties of solid and water components and the reinforcing steel fraction taken into account for the concrete thermal properties calculation (Table 3-2). Hydrostatic conditions were applied (no groundwater flow) and only forced convection, in the pipes, and conduction, in the other elements, were considered.

Table 3-2 - Thermo-physical properties of the soil and reinforced concrete (Sterpi et al., 2020).

		Density, ρ	**Thermal cond., λ**	**Specific heat, c**
		[kg/m³]	**[W/(mK)]**	**[J/(kgK)]**
Water/Heat carrier fluid		1000	0.57	4186
Solid grains		2750	3.6	820
Initial analysis	Saturated soil	1930	2.2	1642
	Reinforced concrete 2.4%	2500	2.6	880
Sensitivity analysis	Dry soil	1460	0.4	725
	Reinforced concrete 1%	2500	1.8	880

The authors used the field data available to perform a sensitivity analysis and validate their initial assumptions. The numerical results demonstrated that the saturated soil thermal properties, rather than a dry soil, are adequate and that the reinforcing steel fraction has no effect on the overall output. On the other hand, the authors found that by applying the damping coefficient of 0.66 in the summer and no damping coefficient in the winter, a better agreement is achieved with the field data. This is possibly due to the natural convection in some parts of the basement wall that may lower the higher temperatures in the summer but do not increase the temperatures in winter. This calibrated model returns a heat transfer rate of 14.6 W/m^2, an underestimation of 2% from the monitored performance (see Section 3.2.3).

The authors performed further numerical analyses to define a pipe layout that maximizes heat transfer rates. It was found that the thermal interferences between pipe branches, i.e. adjacent pipes with the heat transfer fluid at different temperatures, led to a decrease of the system efficiency. Also, the length of the heat exchanger pipes on the exposed part of the wall can result in a lower heat power output, e.g. when the heat flux direction (wall to the heat exchanger pipes or the opposite) is detrimental to the heating or cooling operation. As a result, two heat exchanger pipe layouts were defined to address

spacing between pipe branches and pipe length on the exposed part of the wall. They consist of one down flow and one up flow branch in the top of the panel, spaced at 0.6 m, that connects with a single w-shaped (Figure 3.11a)) or double w-shaped (Figure 3.11b)) loop (located in the part of the wall embedded below the excavation), resulting in an increase of performance, compared to the initial layout, of 10.0% (16.1 W/m2) and 15.8% (16.9 W/m2), respectively.

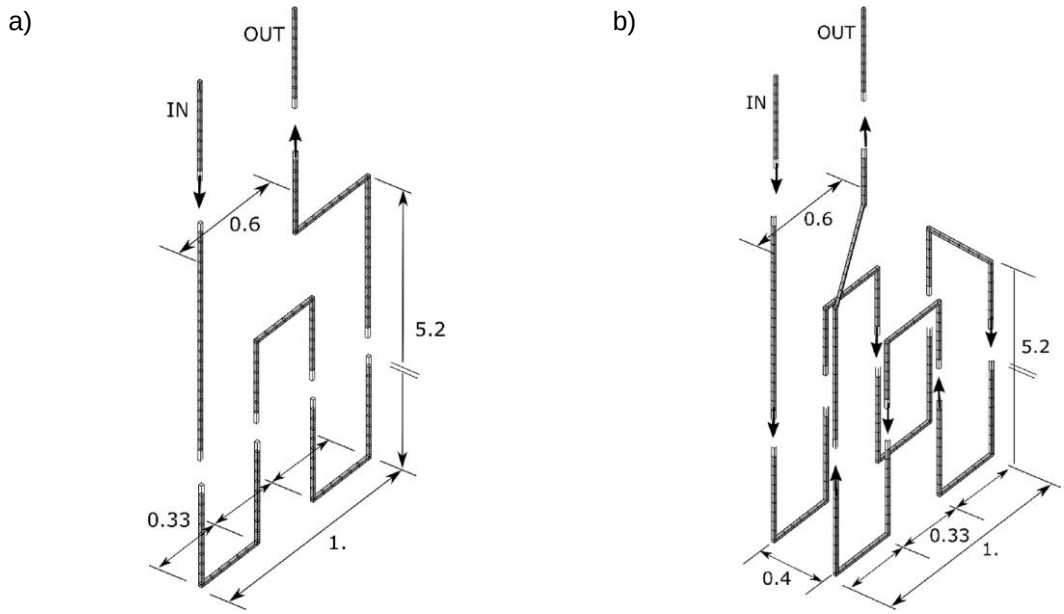

Figure 3.11 - Layout of the enhanced heat exchanger pipe (units in m): a) Single-W, b) Double-W (Sterpi et al., 2020).

3.3.3 3D transient analysis

Di Donna et al. (2017) reported a parametric study undertaken to better understand which parameters impact energy wall performance the most. In a first stage, a model validation was performed based on the wall parameters and monitoring data from Xia et al. (2012), more specifically the scheme no. 1 described in Table 3-1(see Section 3.2.2) with the heat exchanger pipe layout c). The average soil and wall temperatures reported in Section 3.2.2 were assigned as initial temperatures for the soil and wall elements and a constant external air temperature of 10.6ºC was applied at the top (ground surface), excavation base and exposed wall face boundaries. Additionally, a constant average soil temperature was applied to the bottom, right and left boundaries of the model. Therefore, only constant temperature BC were defined. The simulation time was set to two days and a concrete cover to the pipes of 10 cm was specified. The soil and concrete properties are presented in Table 3-3. The authors reported a good agreement between the numerical results and the heat exchanger power calculated from the monitoring data. Although, it is not clear how Xia et al. (2012) normalized their results, if by the wall depth or by the length of the heat exchanger pipes. This will be discussed in more detail in section 4.2.

Table 3-3 - Soil and concrete properties assumed in the model validation. Adapted from (Di Donna et al., 2017).

	Bulk Density, ρ	Bulk Thermal cond., λ	Bulk Specific heat capacity, c
	[kg/m³]	[W/(mK)]	[J/(kgK)]
Concrete	2500	2.34	1046
Soil	1800	1.74	1690
Heat Carrier fluid	1000	0.58	4200

Following the numerical model validation, a parametric study was performed focusing on the following parameters: wall thickness (T_w), excavation to wall depth ratio (R), heat transfer fluid velocity (v), spacing between pipe branches (S_L), concrete cover to the pipes (C), temperature difference between the soil and the air in contact with the exposed wall surface (ΔT), and concrete thermal conductivity (λ_{conc}). A statistical method was applied to define the parameter values for each of the eight runs (Table 3-4) and, in a subsequent phase, to assess the evolution of the impact of each parameter on the heat exchange.

Table 3-4 - Parameter values for each run of the parametric study (Di Donna et al., 2017)

		Parameter						
		T_W [m]	R [-]	S_L [m]	C [mm]	v [m/s]	ΔT [ºC]	λ_{conc} [W/(m K)]
Run Number	**1**	0.8	1.25	0.25	50	0.2	2.0	1.5
	2	0.8	1.25	0.25	100	1.2	6.0	3.0
	3	0.8	2.0	0.75	50	0.2	6.0	3.0
	4	0.8	2.0	0.75	100	1.2	2.0	1.5
	5	1.2	1.25	0.75	50	1.2	2.0	3.0
	6	1.2	1.25	0.75	100	0.2	6.0	1.5
	7	1.2	2.0	0.25	50	1.2	6.0	1.5
	8	1.2	2.0	0.25	100	0.2	2.0	3.0

Figure 3.12 presents the model geometry that varies according to the geometrical parameters studied, namely the wall thickness (T_w), the excavation to wall depth ratio, defined as a function of the excavation depth (De), the pipe spacing (S_L), and the concrete cover (C) (not represented). The wall section considered was 20 m deep and 1.5 m wide. The heat exchanger pipes extended from the top of the wall to 19.5 m depth and were implemented by means of one-dimensional (1D) elements. The initial soil temperature was set to 12ºC. Regarding the BC, only constant temperature BC were defined. Specifically, a 12ºC constant temperature BC was assigned on the left, right and bottom model boundaries and a 14ºC or 18ºC constant temperature BC was assigned to the top of the model, wall face and base of the excavation, depending of the value of ΔT (2ºC or 6ºC). A constant inlet temperature of 20ºC and pipe fluid velocity, depending on the run, were defined, thus reproducing a heat injection scenario, and the simulation had a duration of 60 days. The soil and concrete properties are presented in Table 3-5.

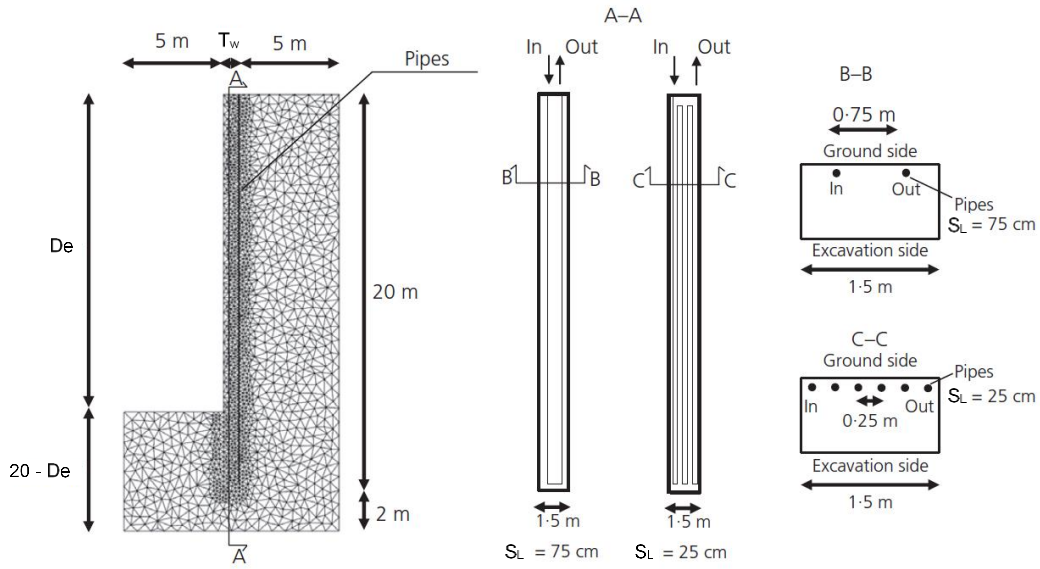

Figure 3.12 - Parametric study model geometry: a) finite-element mesh and model dimensions, b) vertical cross section and c) horizontal cross section of the wall panel. Adapted from (Di Donna et al., 2017).

Table 3-5 - Soil and concrete properties assumed in the parametric study. Adapted from (Di Donna et al., 2017).

	Bulk Density ρ	**Bulk Thermal cond. λ**	**Bulk Specific heat capacity c**
	[kg/m³]	**[W/(mK)]**	**[J/(kg K)]**
Concrete	2210	Depends on the run	1600
Soil	1900	2.00	1600
Heat Carrier fluid	1000	0.60	4200

After a simulation period of 60 days, the heat exchange power per square metre of wall ranged between 5 and 15 W/m^2, for the eight runs. Following the statistical analysis, the authors ranked the parameters to better understand their influence in the short and long-term (after 60 days) system performance. From Figure 3.13, it was concluded that: 1) pipe spacing and the temperature difference between the soil and the air are the two most important parameters, followed by concrete thermal conductivity; 2) as the initial transient heat exchange progresses to a condition closer to a steady state, the parameters that impact on the system performance also change. Namely, pipe spacing shows a decrease from short to the long-term but remains in the top three most important parameters, and the temperature difference becomes the most important parameter in the long term. This shows that hot environments, like metro stations, together with heat exchanger pipes in both sides of the wall and a reduced pipe spacing, are more favourable for heat extraction than for heat disposal. The authors also point out that, contrary to expected, the excavation to wall depth ratio has limited importance on the overall thermal performance, which could be more important at steady state, which was not considered in this parametric study.

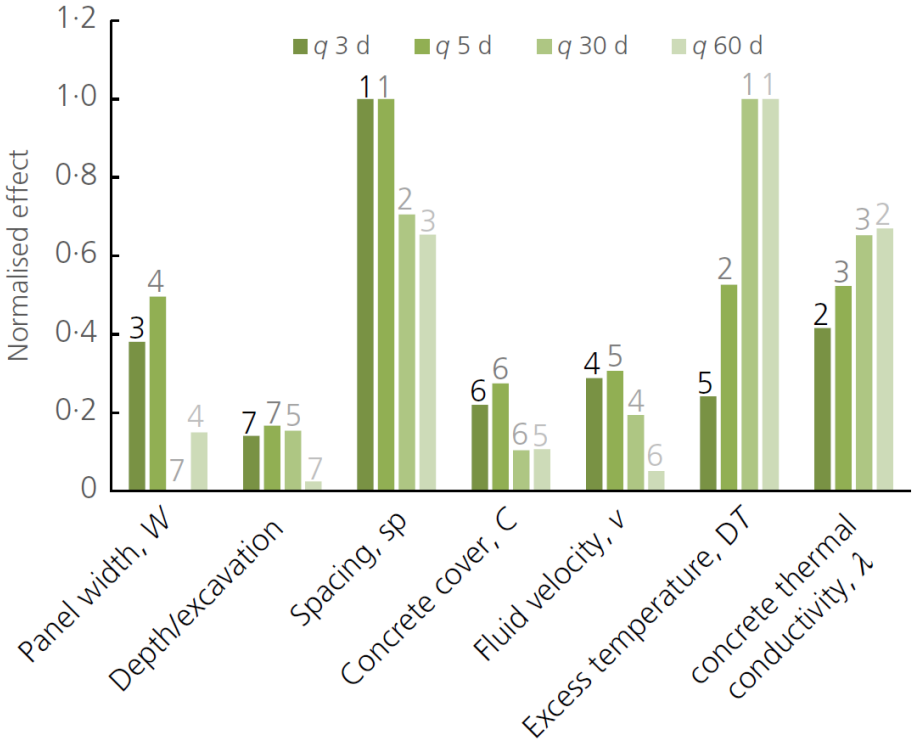

Figure 3.13 - Normalised effect and ranking of each parameter on the heat exchanged for multiple time frames (Di Donna et al., 2017).

4 Numerical analysis: model validation

4.1 Introduction

The first stage when performing numerical analysis consists of validating the models against real monitoring data, which is scarce for energy walls, and other similar numerical models. Therefore, the software was tested against the field test performed at the Shanghai Museum of Natural History (Xia et al., 2012), and against a parametric study presented by Di Donna et al. (2017).

To provide a better understanding of the assumptions used in the subsequent model validation and the parametric study, the following sub-sections will present a comprehensive overview of the software used and the heat transfer processes modelled.

4.1.1 Finite element software introduction

The finite element software FEFLOW enables complex analysis of groundwater flow, mass and heat transport, in porous and fractured materials, and is mainly used in the analysis of hydrogeological problems. However, thermal and coupled thermo-hydro analysis of energy walls using FEFLOW have been reported in the literature, e.g. Barla et al. (2020), Di Donna et al. (2017, 2020), and validate the potential of the finite element software to study the energy performance of energy geostructures and other GSHP systems.

All of the numerical simulations presented in this and the next chapter have the same basis: a transient analysis of a three-dimensional (3D) model with heat transfer by conduction and without convective heat flow due to groundwater flow. The general methodology for establishing the 3D model in FEFLOW, as well as some assumptions of the software, are described in this section and are also relevant in subsequent sections and chapters.

To generate the finite element mesh, a two-dimensional (2D) vertical cross-section is defined first, according to the model boundaries and wall geometry, along with a line positioned on the location of the heat exchanger loop, to “impose” a continuous alignment of mesh element edges, in the following stage. Subsequently, the mesh is generated using triangular elements, according to the element dimensions and defined refinement areas. Then the 2D model is converted to a 3D model through a layered configuration in which a defined spacing is applied to each layer. The spacing and the number of layers describe not only the model width but also the degree of discretisation in the third dimension. Then, the triangular mesh elements are transformed into prismatic six-node 3D elements that are vertically aligned and form a layer (an example can be seen in Figure 4.2. In FEFLOW terminology, a slice is a set of 2D mesh elements while a layer is a set of 3D elements located between two slices.

After the 3D model generation, the problem class is defined, i.e. it is specified as a saturated groundwater medium, including only the transport of heat in a transient state. Following these steps, the remaining parameters can be assigned: initial temperature and material thermal properties are assigned to the elements while boundary conditions are assigned to the element nodes. Lastly, the heat exchanger loop geometry is implemented via 1D special elements called “Discrete Features”, assigned to the edges of the mesh elements. Although these elements neglect the HDPE pipe wall resistance, authors report insignificant temperature output errors (Di Donna et al., 2017). There are three different flow laws available: Darcy law, that describes the fluid flow through a porous medium, Hagen-Poiseuille law, that describes the flow of an incompressible and Newtonian fluid (constant viscosity) in a long cylindrical pipe of constant cross-section, and Manning-Strickler empirical formula, that estimates the average fluid velocity in free-surface flows like open channels or partially full conduits. The formulation does not include the thermal resistance of the boundary layer in non-turbulent flow and therefore, varying the fluid velocity will not have any effect on heat transfer, except at very low velocities.

Since the heat exchanger loops are long cylindrical and constant cross-section pipes, the Hagen-Poiseuille law is the most suitable. According to Diersch (2014), the velocity in an axisymmetric flow (Figure 4.1) is given by:

$$v_z = -\frac{1}{4\mu}\left(\frac{\boldsymbol{dp}}{\boldsymbol{dz}} - \rho_f g_z\right)\left({R_p}^2 - r^2\right) \tag{4-1}$$

Where:

- v_z: fluid velocity along z-axis [m s^{-1}];
- μ: dynamic viscosity of the fluid [Pa.s];
- ρ_f: fluid density [kg m^{-3}];
- g_z: gravity along z-axis [m s^{-2}];
- R_p: radius of the pipe;
- r: radial coordinate;

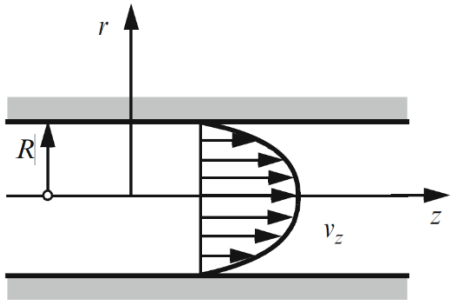

Figure 4.1 - Axisymmetric Hagen-Poiseuille flow in a circular pipe.

Subsequently, the average velocity of the flow becomes:

$$\bar{v}_z = -\frac{R_p}{8\mu}\left(\frac{\boldsymbol{dp}}{\boldsymbol{dz}} - \rho_f g_z\right) \quad (4\text{-}2)$$

Equation (4-2) can be expressed in terms of the hydraulic radius, defined as the ratio between the cross section area and the wetted perimeter of the channel. For a submerged circular cross-section, the hydraulic radius is given by:

$$r_{hydr} = \frac{\pi {R_p}^2}{2\pi R_p} \quad (4\text{-}3)$$

And (4-2) becomes:

$$\bar{v}_z = -\frac{r_{hydr}^2}{2\mu}\left(\frac{dp}{dz} - \rho_f g_z\right) \quad (4\text{-}4)$$

Additionally, and given that the standard geometry for 1D discrete features is not the submerged circular cross-section, corrections must be adopted. These corrections are assigned into the software via the hydraulic aperture, b, for the Haggen-Poiseuille law (Diersch, 2014). For the submerged circular cross-section, the corrected hydraulic aperture is computed by:

$$b = 1.224745\, R_p \sqrt{\frac{f}{f_0}} \quad (4\text{-}5)$$

Where R_p is the pipe radius, f is a parameter factor to input different values of viscosity (μ), gravity (g) and density (ρ) than the standard ones, considered by the parameter factor f_0. Once that the standard values of water viscosity (1.3 Pa s), gravity (9.81 m/s) and water density (1000 kg/m^3) were assumed, equation (4-5) becomes:

$$b = 1.224745\, R_p \quad (4\text{-}6)$$

FEFLOW will then compute the true hydraulic radius of the heat exchanger pipes via the hydraulic aperture, b, and the geometrical input parameter, the cross-section area, *A*. Additionally, to impose a fluid flow in the pipes, the fluid velocity value is assigned to the inlet and outlet nodes via a fluid-flux boundary condition. The software considers inflows as negative and outflows as positive, thus a negative value is assigned to the inlet node and a positive one to the outlet node.

4.1.2 Heat transfer mechanisms

The internal energy of a system includes the kinetic and potential energy of the random translational, rotational and vibrational motion of atoms and molecules and is related to the temperature of the system. Heat is a process by which the thermal energy is exchanged with other systems, due to a temperature difference. It also refers to the total amount of energy exchanged. Therefore, three different heat transfer mechanisms can be defined: conduction, convection and radiation. The latter can be neglected as the temperature ranges in shallow geothermal energy systems are low, resulting in low energy radiated.

Thermal conduction is the main heat transfer mechanism and is characterized by the exchange of internal energy, through the collision of high-energy microscopic particles with low-energy particles, between two adjacent areas of the same body or two different bodies in direct contact. Conductive heat transfer takes place in all phases (solid, liquid and gas) and the rate of energy exchanged depends on the temperature gradient and the conductive properties of the material i.e. the thermal conductivity, as stated by the differential form of the Fourier's Law:

$$q_{cond} = -\lambda \nabla T \tag{4-7}$$

Where:

- q_{cond}: rate of heat transfer per unit of area by conduction [W m^{-2}];
- λ: material's thermal conductivity [W m^{-1} K^{-1}];
- ∇T: temperature gradient [K m^{-1}];

In a transient state, the Fourier's Law is not valid since temperature changes over time. For a system that only changes its total energy due to the thermal energy exchanged through its boundaries, the principle of energy conservation states that the rate of increase of the total energy stored in the system is equal to the rate of energy entering the system minus the rate of energy leaving the system. Therefore, as the temperature distribution in the medium is determined, the conductive heat flux can be computed by the Fourier's Law. For an isotropic material with constant thermal conductivity, the heat diffusion equation is

$$\frac{\partial^2 T}{\partial x^2} + \frac{\partial^2 T}{\partial y^2} + \frac{\partial^2 T}{\partial z^2} = \frac{1}{\alpha}\frac{\partial T}{\partial t} \tag{4-8}$$

Where $\alpha = \lambda/\rho c$ is the thermal diffusivity [m^2/s], a measure of the ability of the material to conduct thermal energy relative to its storage capacity (Bergman et al., 2011).

When groundwater flow is absent, as will be assumed in all of the numerical simulations performed in this thesis, heat conduction will be the main heat transfer mechanism. Though, convection will be the governing heat transfer mechanism on the 1D elements simulating the fluid flow on the heat exchanger pipes. Convection can be described by Newton's law of cooling:

$$q_{conv} = h(T_S - T_f) \tag{4-9}$$

Where:

- q_{conv}: rate of heat transfer per unit of area by convection [W m^{-2}];
- h: convective heat transfer coefficient [W m^{-2} K^{-1}];
- T_S: surface temperature [K];
- T_f: fluid temperature [K];

As the fluid motion imposes heat transport, the heat transfer mechanism is referred to as forced convection. According to Bergman et al. (2011), in the case of an incompressible fluid flow in a pipe, it is possible to relate the convective heat transfer rate to the difference in temperature at the inlet and outlet, through the following equation:

$$q_{conv} = mc_p(T_o - T_i) \tag{4-10}$$

Where:

- m: mass flow rate [kg/s];
- c_p: fluid specific heat capacity at constant pressure [J kg^{-1} K^{-1}];
- T_o: outlet temperature [K];
- T_i: inlet temperature [K];

4.2 Validation with field test

To better understand the response of the finite element software FEFLOW, a model reproducing the field tests of Xia et al. (2012) at the Shanghai Museum of Natural History was assembled. The results of this numerical analysis are then compared to the monitoring data and the numerical model validation results presented by Di Donna et al. (2017) for the same set of field data.

4.2.1 Geometry and material properties

The model reproduces the wall panel geometry, and experimental scheme no. 1 (Table 3-1) alongside the heat exchanger layout c) (Figure 3.5), presented in section 3.2.2. The model domain is 10 m long, 40 m high and 2.25 m wide, to allow for an additional comparison with the numerical results reported in Di Donna et al. (2017), and is presented in Figure 4.2 (the out of plane direction has a scaling factor of 5, in the case of the 3D model). As stated in the previous section, the 3D layered model is generated by extruding the 2D mesh elements. This is achieved by defining the width of each layer and the number of layers (see Table 4-3).

The heat exchanger pipes are spaced at 0.75 m centres and are located centrally in the panel width and 100 mm from the soil side. These were implemented via the 1D special elements, considering a distance between the horizontal pipe branch and the wall base of 0.25 m. While the pipe cover was reported by Xia et al. (2012), the distance between the wall base and the horizontal pipe branch was assumed by the author. The spacing between pipe branches was set to 0.75 m following Xia et al. (2012). The pipe cross-section geometry is summarized in Table 4-1.

Table 4-1 - Pipe geometric parameters.

Pipe outer diameter, d_o [mm]	25
Pipe wall thickness, t_w [mm]	2.3
Pipe inner diameter, d_i [mm]	20.4
Cross sectional area, A [mm²]	326.851

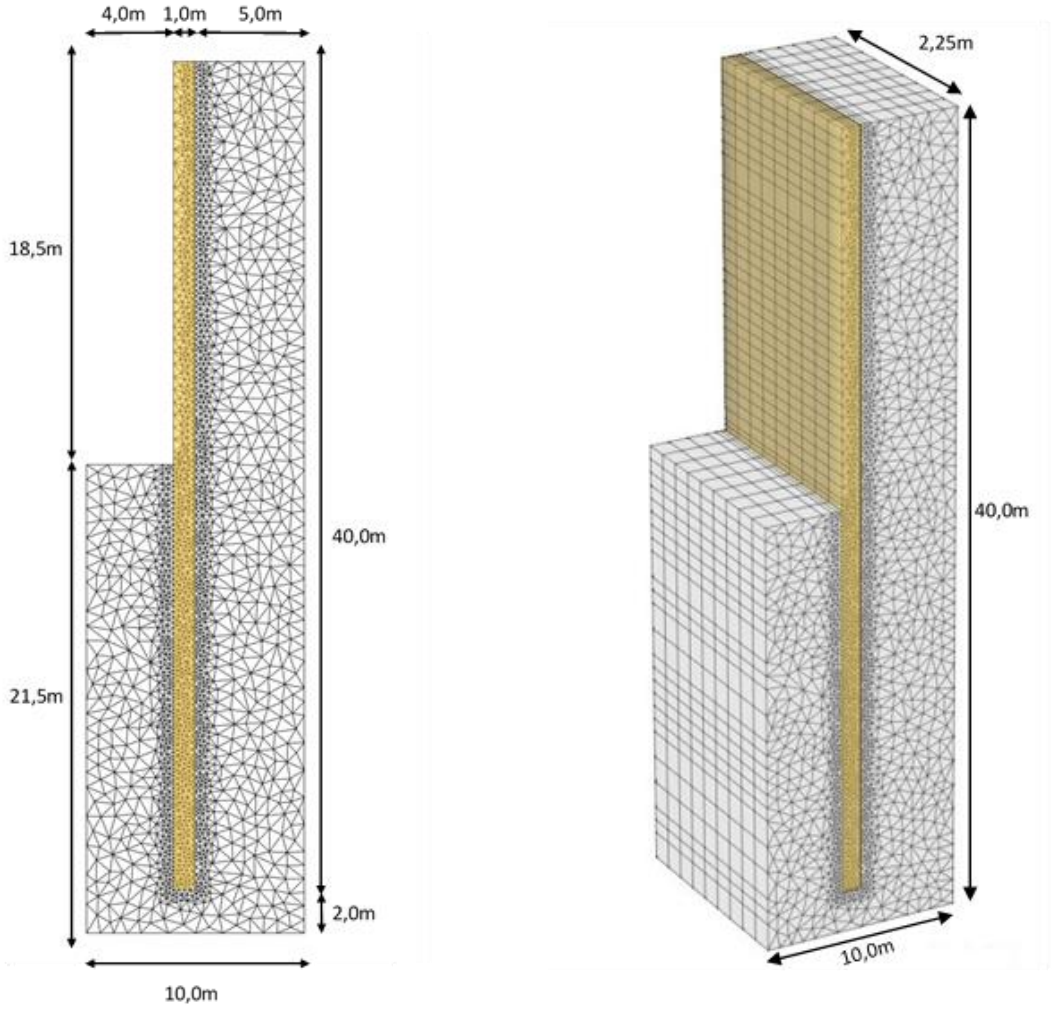

Figure 4.2 - Model geometry and dimensions.

Figure 4.3 illustrates the 1D elements assigned to the mesh element edges in the 3D model, alongside the inlet and outlet location at the top of the wall. To simulate the fluid flow inside the elements, a fluid flux has to be prescribed along with an inlet temperature. The fluid flux was specified in terms of a fluid velocity, ν of 0.6 m/s with a negative and positive value at the inlet and outlet node, respectively. The inlet temperature was set to a constant value of 35ºC, as used in the test reported by Xia et al. (2012). The numerical simulation duration was set to 3 days, as per Di Donna et al. (2017), even though Xia et al. (2012) reported a 2 day field test duration.

a) b)

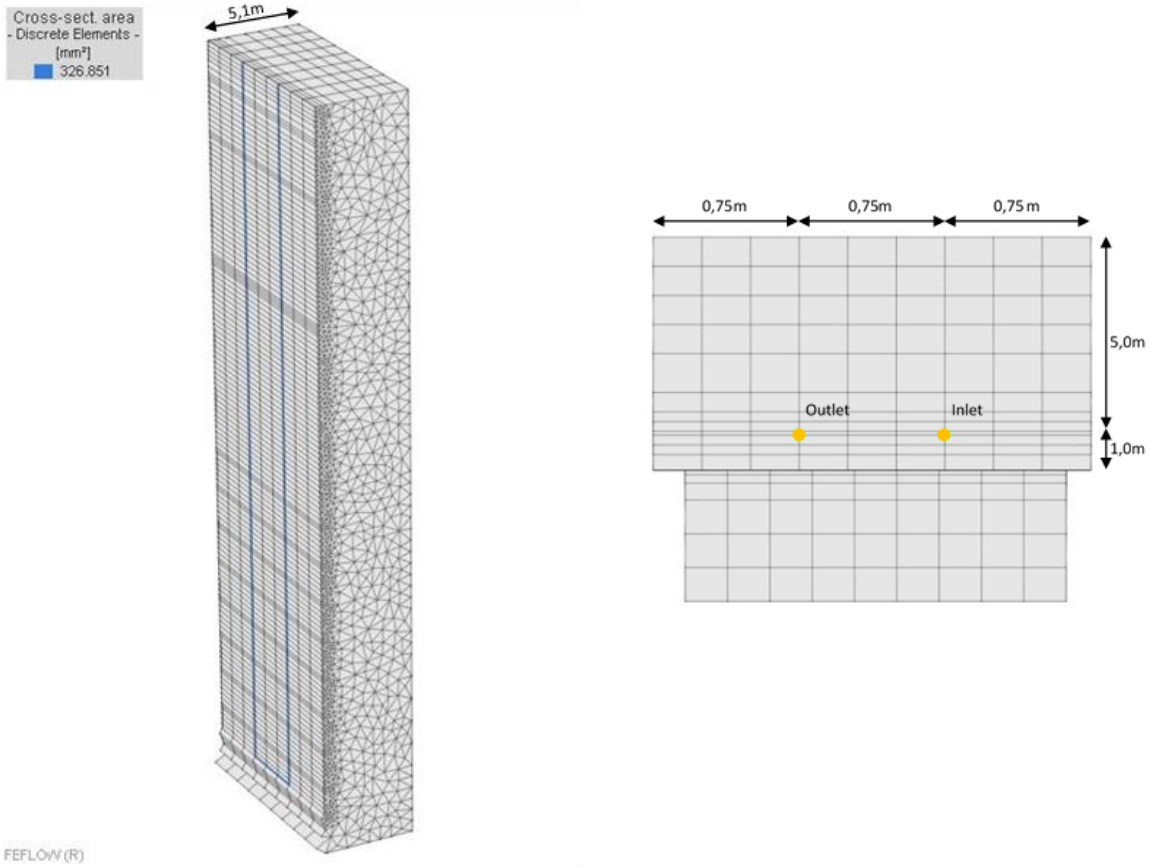

Figure 4.3 - Implementation of the heat exchanger loop in the 3D model: a) vertical distribution of 1D elements; b) plane view of 1D elements at top boundary.

The thermo-physical properties of concrete, soil and heat carrier fluid are presented in Table 3-3 in terms of bulk values. FEFLOW considers the solid and water phases separately and computes for each element the bulk thermal conductivity and volumetric heat capacity according to the element porosity. A material such as soil is characterized as a three-phase medium consisting of the soil skeleton (solid phase), water (liquid phase) and air (gaseous phase). Porosity is a dimensionless parameter that describes the ratio of void space over the total volume of the material:

$$n = \frac{V_w + V_a}{V_S + V_w + V_a} = \frac{V_V}{V} \tag{4-11}$$

Where:

- V_V: volume of voids [m³];
- V_w: volume of water [m³];
- V_a: volume of air [m³];
- V_S: volume of solids [m³];
- V: total volume of soil [m³];

Considering a saturated soil, i.e. a soil with all the voids filled with water, the following relations can be established:

$$\rho = n\rho_w + (1-n)\rho_s \quad (4\text{-}12)$$

$$\rho c = n\rho_w c_w + (1-n)\rho_s c_s \quad (4\text{-}13)$$

$$\lambda = n\lambda_w + (1-n)\lambda_s \quad (4\text{-}14)$$

Where ρ is the bulk density [kg m^{-3}], ρc is the bulk volumetric heat capacity [J K^{-1} m^{-3}], λ is the bulk thermal conductivity [W m^{-1} K^{-1}] and the subscripts w and s refer to the water and solid phase, respectively. Considering the thermal properties (Table 3-3) as well as the values of porosity of 0 and 0.25 for the concrete and soil elements, used by Di Donna et al. (2017), the thermal parameter values for the solid phase of the soil (Table 4-2) were calculated through equations (4-12), (4-13) and (4-14), assuming the default values of FEFLOW for the thermal properties of groundwater. Although some authors report higher values of porosity for Shanghai deposits (Tan & Li, 2011; Tan & Wei, 2012; Xu et al., 2015), the value of soil porosity used by Di Donna et al. (2017) is not expected to impact the thermal output since the bulk values are in accordance with the values reported by Sun et al. (2013) for this field test. In fact, the solid and liquid phase parameter values are only needed if groundwater flow is considered. Therefore, an alternative approach of defining the bulk values directly in the software, could have been used.

Table 4-2 - Thermophysical properties of concrete, soil (solid and water phases) and heat carrier fluid.

	Porosity	**Density, ρ**	**Thermal cond., λ**	**Volumetric heat capacity, ρc**
	[-]	**[kg/m³]**	**[W/(m K)]**	**[MJ/(K m³)]**
Concrete	0	2500	2.34	2.615
Soil	0.25	1800	1.74	3.042
Solid phase	-	2067	2.10	2.656
Liquid phase	-	1000	0.65	4.200
Heat Carrier fluid	-	1000	0.58	4.200

4.2.2 Boundary conditions, initial conditions and mesh

Xia et al. (2012) reported an average soil temperature of 16.3ºC and an average wall temperature of 23ºC at the beginning of the field test. It is also reported that the wall temperatures at 9 m, 25 m and 35 m depth were 12.2ºC, 25.0ºC and 21.2ºC, respectively, one day before the beginning of the field test. Therefore, assuming an average constant temperature throughout the wall in the numerical model

seemed a relevant simplification when reproducing a short-term test, in which the initial wall temperatures could impact the results considerably.

The air temperature was also measured and was set to 10.6ºC. Therefore, a constant air temperature BC was applied to the top, wall face and excavation plane model boundaries, and a constant soil temperature BC was applied to the left, bottom and right boundaries of the model, Figure 4.4.

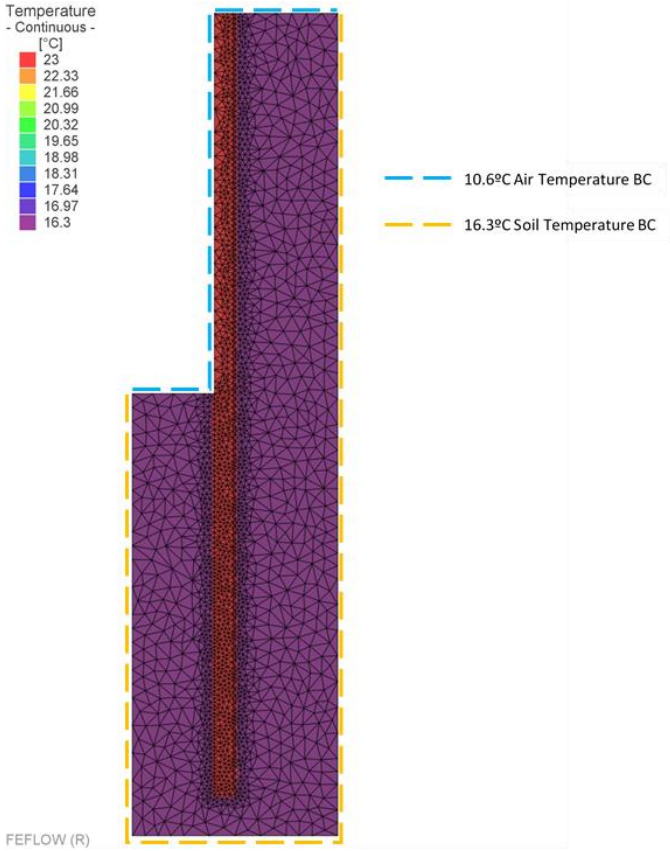

Figure 4.4 - Initial wall and soil temperature and thermal boundary conditions.

In the first simulations, it was shown that the mesh refinement is a crucial parameter, with a significant impact on the results. Therefore, a set of three different meshes were defined to verify how finite element mesh refinement, impacted the stability and accuracy of the results. Table 4-3 lists the properties and refinement details of each mesh and Figure 4.5 shows the 2D and 3D details of the same set of meshes. When defining the three different mesh types, consideration was given to the fact that elements should not be distorted, i.e. the dimension of the element in the plane should be approximately equivalent to their third dimension. Therefore, the average size, in mesh type M1, of the elements adjacent to the heat exchanger loop is around 0.15 m (plane) and 0.125 m (third dimension) while in mesh type M2 and M3, the size of the elements adjacent to the heat exchanger loop is around 0.29 m (plane) and 0.25 m (third dimension). In the wall face, the average element size is equal to that along the heat exchanger loop for mesh type M1 and M2 and 0.57 m for mesh type M3. All of the three mesh types have an average element size of 0.65 m near the other model boundaries.

Table 4-3 - Properties of the analysed meshes.

Mesh	# Nodes	# Elements	# Nodes per slice	# Layers	Refinement Selection
M1	89338	164952	4702 (19 slices)	18 (0.125m)	Wall and pipe + additional wall elements refinement
M2	24010	41670	2401 (10 slices)	9 (0.25m)	Wall and pipe
M3	22750	39699	2275 (10 slices)	9 (0.25m)	Wall (except wall face) and pipe

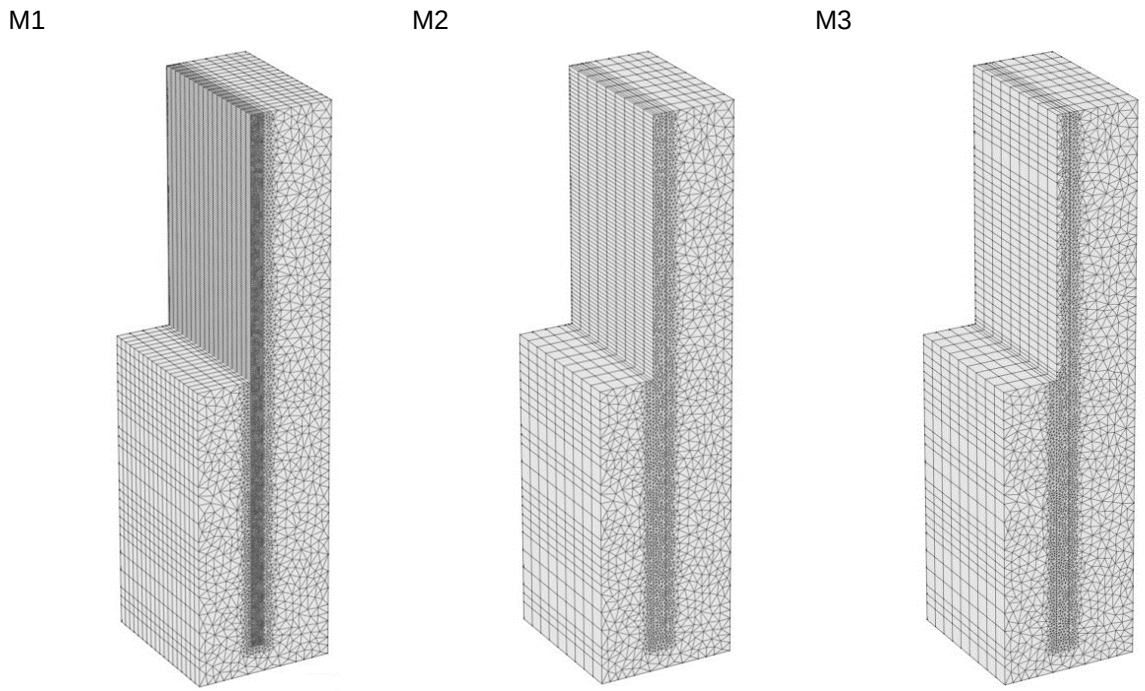

Figure 4.5 - 2D and 3D mesh details.

Additionally, mesh refinement should not be analysed without taking into consideration the time step length, especially early in the simulation as the software has to compute the high temperature gradients imposed by the difference in temperature between the wall (initial temperature of 23º C) and the heat carrier fluid circulating in the pipes (35º C). These high temperature gradients can result in convergence problems as the software computes a temperature field in which convergence is not reached, and uses that temperature field in the following time step, resulting in a series of under and overestimations of temperature around a more stable solution. Usually, increasing the maximum number of iterations allowed in each time step do not result in reaching convergence, it being more time-efficient to decrease the time step length. This decreases the complexity associated with the estimation of a temperature field with high temperature gradients between large simulation periods. The convergence problems tend to disappear in higher simulation times as the temperature increases around the heat exchanger pipes, lowering the temperature gradients around those elements, and the system tends to an equilibrium. Therefore, a set of three different types of time step were defined and are listed in Table 4-4.

Table 4-4 - Properties of the analysed time steps.

Time step	Prescribed additional time steps	Time step length	Simulation time interval
T1	-	Variable	-
T2	100	0.001	0.001d to 0.1d
T3	42	0.05	0.025d to 0.9d

4.2.3 Results and discussion

The exchanged power, Q [W], and the heat transfer rate per metre of pipe, q_L [W m^{-1}], can be calculated using the following equations:

$$Q = mc_w\,(T_i - T_o) \tag{4-15}$$

$$q_L = \frac{Q}{L} \tag{4-16}$$

Where c_w is the specific heat capacity of heat exchange fluid, in this case water [J kg^{-1} K^{-1}], T_i and T_o are the inlet and outlet temperatures [K], respectively, L is the length of the heat exchanger loop, and m is the mass flow rate [kg s^{-1}] defined as:

$$m = A\,v\,\rho_w \tag{4-17}$$

4.2.3.1 Influence of mesh refinement and time steps

The first simulation was performed with the mesh type M1, a very refined mesh with 19 slices and 18 layers with a width of 0.125 m, combined with the time step type T1, in which the software automatically controls the time step length. The heat transfer rate per metre of pipe, q_L, is calculated assuming 76.25 m of heat exchanger pipe length. A second simulation was performed considering the mesh type M1 and the time step type T2. Figure 4.6 shows that even with a high refinement mesh, there are some convergence problems at the beginning of the simulation which are eliminated by specifying additional time steps for those simulation times (time step type T2).

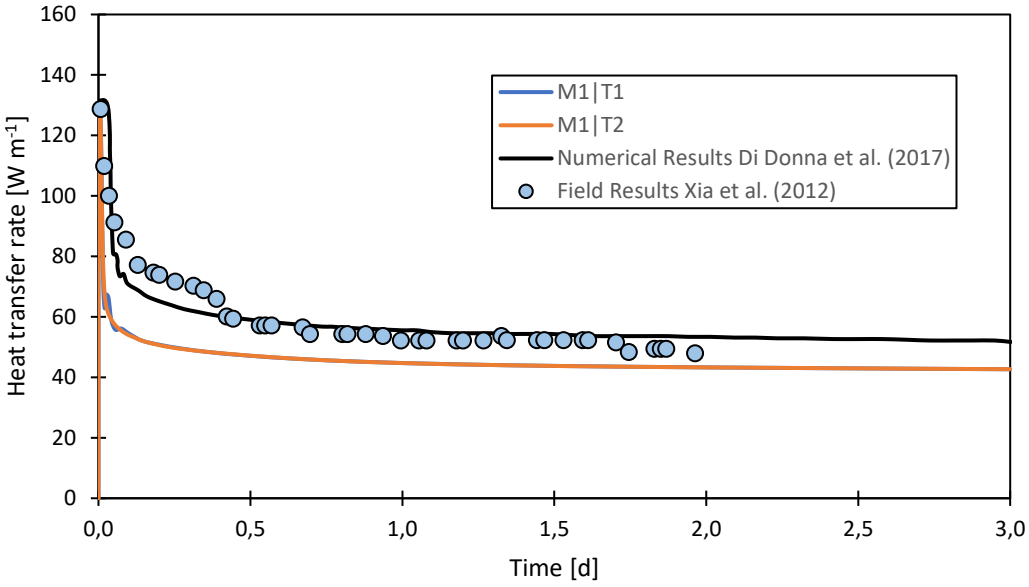

Figure 4.6 - Numerical results of M1T1 and M1T2 against field data and numerical results of Di Donna et al. (2017).

Taking into account the observed behaviour regarding the prescription of additional time steps, two additional simulations were performed. In this case, a coarser mesh was adopted (mesh type M2) in combination with time step type T1 and T3. Compared to the results presented in Figure 4.6, the results of Figure 4.7 show a better agreement with the experimental results of Xia et al. (2012) and the numerical results of Di Donna et al. (2017). As expected, the lack of prescribed time steps in the simulation scheme M2|T1 resulted in convergence problems that were eliminated on the simulation scheme M2|T3. Additionally, the time step scheme T3 combined with the coarser mesh type M2 allowed for a reduction of the simulation run time, when compared to time step scheme T2, without oscillations in the very first stages.

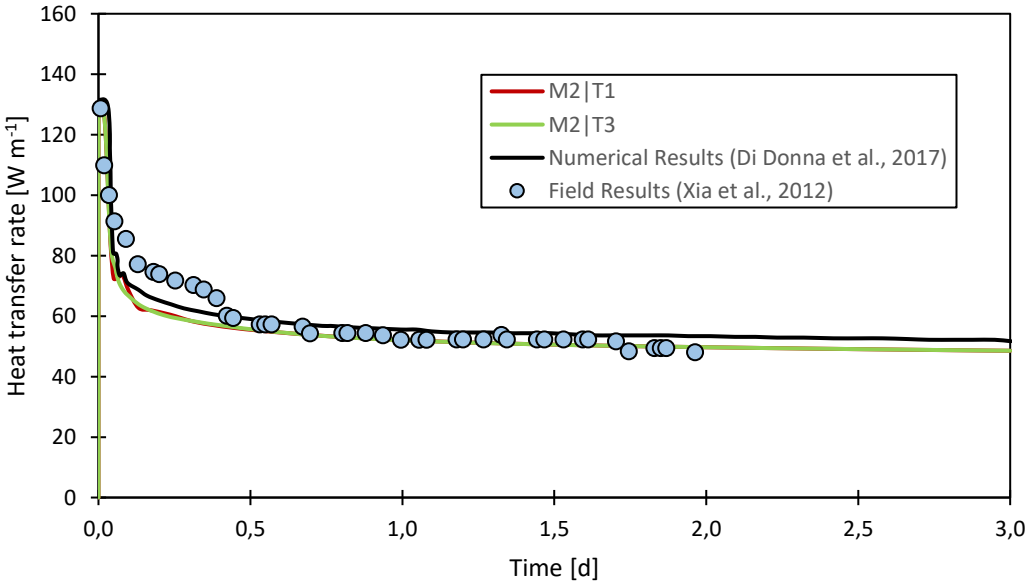

Figure 4.7 - Numerical results of M2T1 and M2T3 against field data and numerical results of (Di Donna et al. (2017).

Two further analyses were performed as the mesh reported by Di Donna et al. (2017) seemed to be coarser than those of the previous simulations. Additionally, they will also assess how the refinement of the wall elements impact the results and the simulation stability, as it is expected that the elements adjacent to the heat exchanger loop require a higher degree of refinement, due to the forced convection imposed in the heat exchanger pipe elements, than the ones of the exposed wall surface. Therefore, the simulation schemes adopted were the M3|T1 and M3|T3. As shown in Figure 4.8, the observed behaviour at the lower time steps was the same as in the previous case. The highest "error" between these results and the results of the previous simulation scheme, for the same time steps, is 0.49%. Even though it is a small difference, the exposed wall surface elements will be subject to refinement in the parametric study presented in the next chapter since there was no significant computational time reduction with this simulation scheme.

Figure 4.9 focuses on the early stages of the above simulations where the convergence problems can be observed more clearly. It is also shown that a better agreement between the results of the numerical analyses and the field test results is achieved after 0.5 d as the initial system response is highly impacted by the initial conditions defined in the numerical model. Also, the early heat transfer rate values are not representative of the system thermal performance as the relatively high values are due to the high temperature differences between the inlet and outlet, that significantly decreases as the heat transfer fluid circulates inside the pipes and the system evolves to an equilibrium.

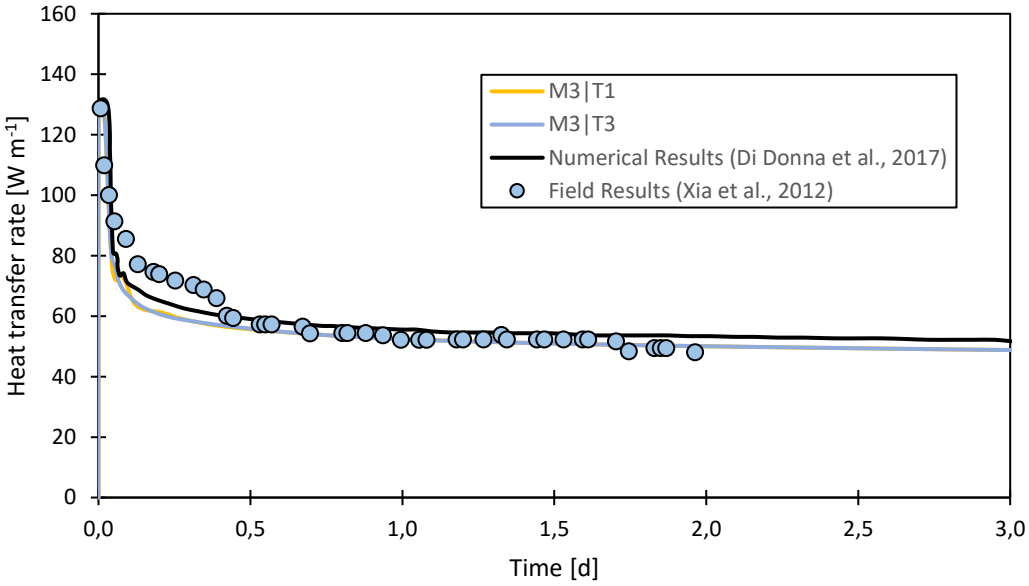

Figure 4.8 - Numerical results of M3T1 and M3T3 against field data and numerical results of Di Donna et al. (2017).

Through the previous results, it is possible to conclude that a distance between slices of 0.25 m shows a better agreement with the experimental data and the numerical results reported by Di Donna et al. (2017), than those at 0.125 m.

An additional simulation was performed without porosity, i.e. assigning a porosity value of zero for the soil, since there will be no groundwater flow in all of the simulations presented in this thesis. This allows the definition of the volumetric heat capacity and thermal conductivity parameters as bulk values. As expected, there was no difference in the results obtained through this approach which will then be used in the parametric study.

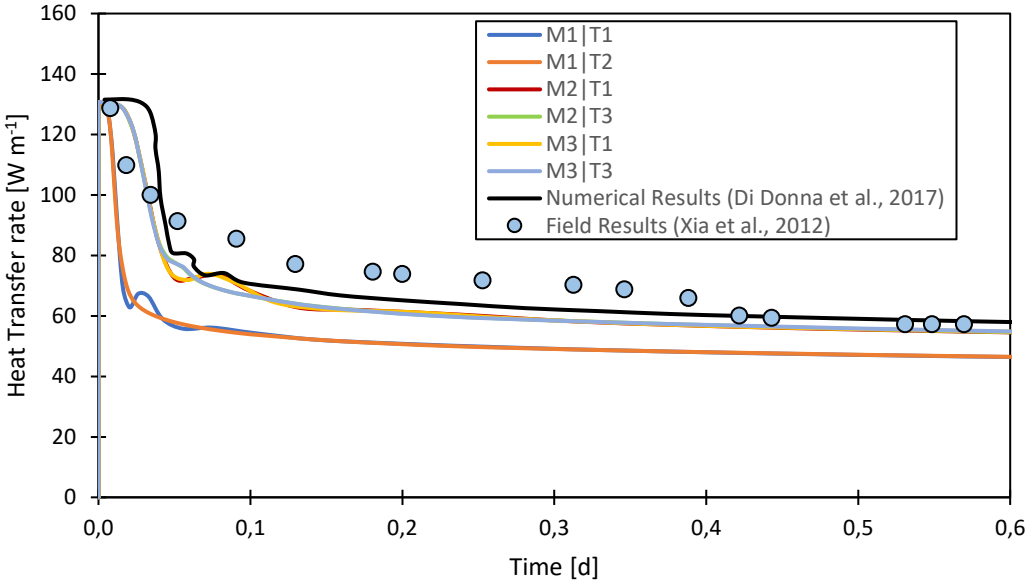

Figure 4.9 - Mesh refinement and time step analysis results against experimental data and numerical results of Di Donna et al. (2017).

4.2.3.2 Influence of initial wall temperature

As stated in section 4.2.2, Xia et al. (2012) reported wall temperature values of 12.2ºC, 25.0ºC and 21.2ºC for 9 m, 25 m and 35 m depth, respectively, one day before the beginning of the field test. As these values were actually the real temperatures of the energy wall before system activation, adopting the average temperature value of 23ºC (also reported by Xia et al. (2012)) in the numerical simulations, as per Di Donna et al. (2017), seemed to be a simplification that was worth evaluating against the available field data. Therefore, an additional simulation was performed considering a different initial temperature in the exposed part (12.2ºC) and embedded part (23ºC) of the wall, as can be seen in Figure 4.10 a). All of the other parameters were kept equal to the previous simulations and the combination M1|T1 was used for the mesh and time steps. The initial temperature of 12.2ºC in the upper part of the wall is in better agreement with the measured air temperature (10.6º C) than an initial temperature of 23.0ºC is, since the lower air temperature in contact with the exposed wall face imposes a heat flow from the wall and the soil, that brings the wall temperature closer to that of the external air temperature.

Figure 4.10 b) presents the results of this simulation with a different initial wall temperature. It is possible to see that this assumption is in better agreement with the field results of Xia et al. (2012) than the "default" simulation M1|T1 and the numerical results of Di Donna et al. (2017) are, which is even more evident after 0.5 d as the results follow the trend of the field data, while the M1|T1 and the numerical

results of Di Donna et al. (2017) show a more stable heat transfer rate evolution after that simulation time.

a) b)

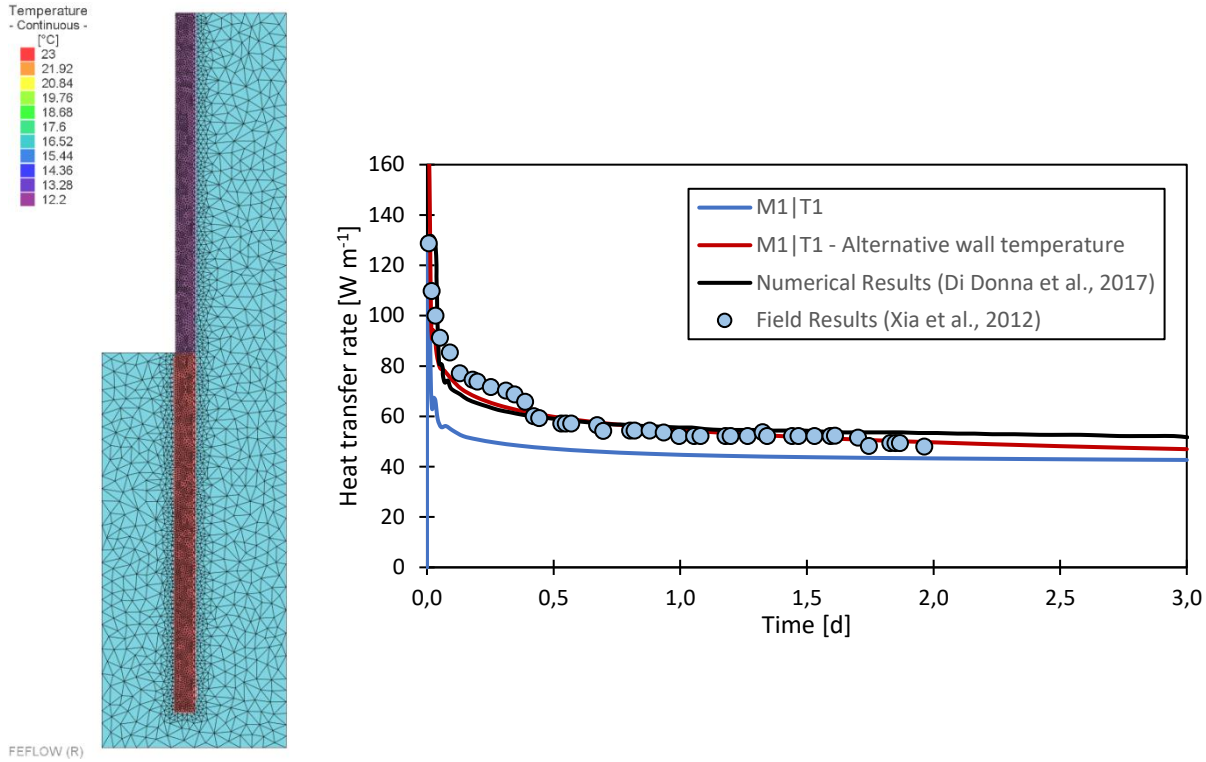

Figure 4.10 - Influence of initial wall temperature: a) initial temperature distribution along the wall; b) heat transfer rate results against M1T1, field data and the numerical results of Di Donna et al. (2017);

4.2.3.3 Influence of inlet temperature

To understand the system response to different inlet temperatures, the experimental scheme no. 3 (Table 3-1) alongside the heat exchanger type c) (Figure 3.5) presented in section 3.2.2 was reproduced. This simulation adds a set of two additional inlet temperatures, 32ºC and 38ºC to the simulations presented in section 4.2.3.1, with the adopted mesh and time step combination M1|T1 and M2|T3. As can be seen in Figure 4.11, the heat transfer rate evolution is similar for the three inlet temperatures, resulting, however, in different thermal performance between them, as expected. It is also noticeable that combination M2|T3 returns higher heat transfer rates than combination M1|T1.

Figure 4.12 presents the relationship between the inlet temperature and the heat transfer rate after two days, to allow for a comparison with the field test results reported by Xia et al. (2012). It is possible to conclude that the linear relationship between the fluid inlet temperature and the heat transfer rate for combinations M1|T1 and M2|T3 are underestimated when compared to the one reported by Xia et al. (2012), i.e. the same increase in inlet temperature results in a lower increase in heat transfer rate. Two further analyses were carried with all of the assumptions presented previously but with the alternative wall temperature distribution presented in section 4.2.3.2. As expected, they result in higher heat transfer rates, with relationship curves almost parallel to the ones with a uniform wall temperature of 23ºC. The average increase from the uniform temperature wall distribution to the alternative temperature wall

distribution is 16.5% and 16.7% for combination M1|T1 and M2|T3, respectively. A similar increase of 16.2% and 16.4% is observed between the results computed through combination M1|T1 and the results computed through combination M2|T3, for the uniform and alternative temperature wall distribution, respectively. Xia et al. (2012) report heat transfer rates of 33.6 W/m, 50.0 W/m and 68.4 W/m for inlet temperature of 32ºC, 35ºC and 38ºC, respectively, which correlates to a 48.8% increase from 32ºC to 35ºC and a 36.8% increase from 35ºC to 38ºC. These results compare to an average increase, for the two mesh and time step combinations, of 25.2% and 18.5% from 32ºC to 35ºC and from 35ºC to 38ºC, respectively. This indicates that the lack of matching between the numerical results and the field test results is due to some field test conditions that were not reported and are not being properly reproduced by the numerical models.

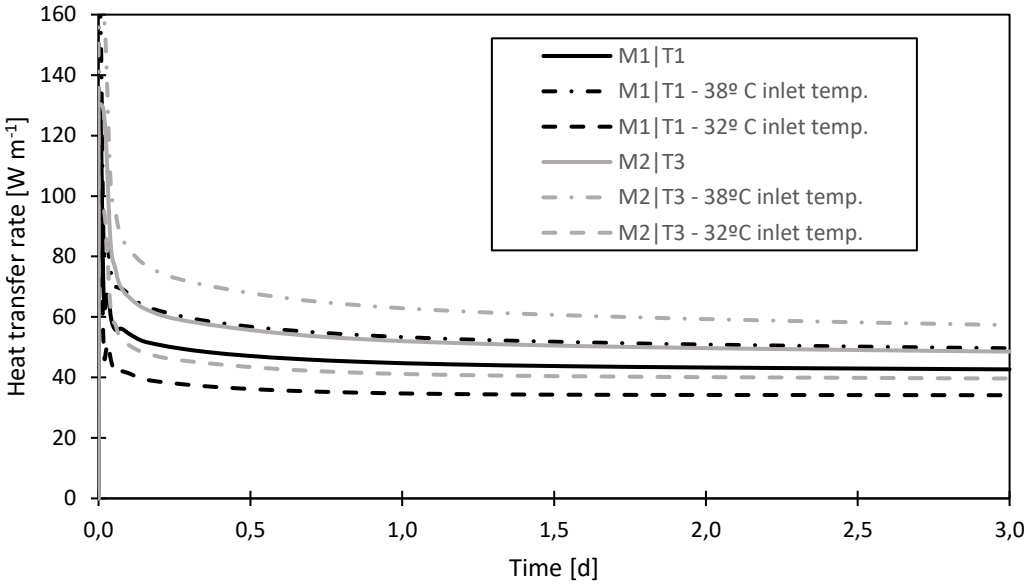

Figure 4.11 - Results for different inlet temperatures.

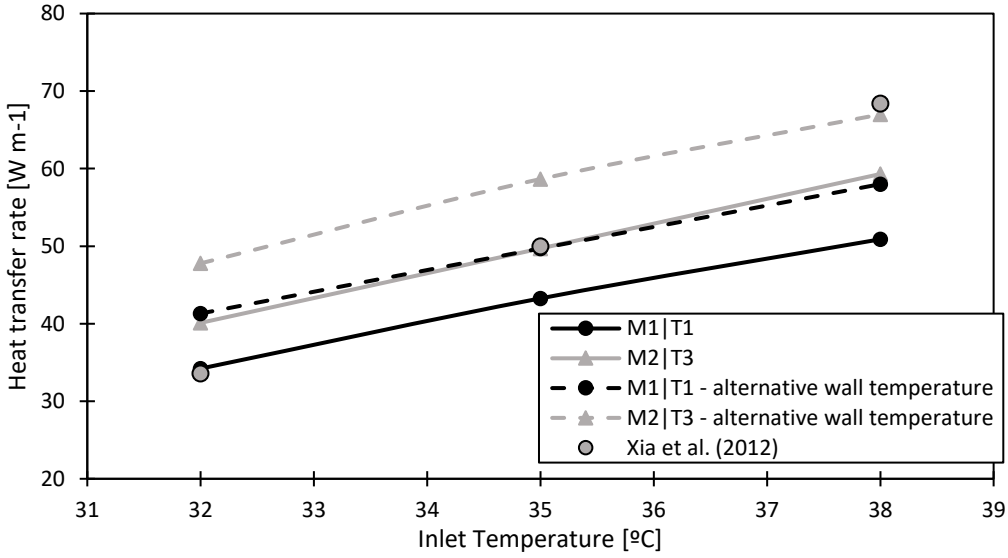

Figure 4.12 - Relationship between the inlet temperature and the heat transfer rate at time = 2 d.

4.2.4 Conclusions

From the previous analyses, it is possible to conclude that when reproducing a field test through numerical analysis, a large number of factors impact the outcome results. In the first place, the mesh and time step discretization can significantly impact the results of the numerical simulations which demonstrates how important it is to validate the software response against field data.

Secondly, a set of detailed information describing the field test is essential to properly reproduce the field conditions. As highlighted in section 4.2.3.2, the initial wall temperature impacts the heat transfer rate results in the short-term field test, with a different temperature in the exposed part of the wall showing a better agreement with the field results. Although, these additional simulations were carried out assuming a temperature distribution based on the wall temperatures one day before the beginning of the field test, that was undertaken between March and July, a period in which the diaphragm walls were certainly exposed to different thermal conditions. This also possibly explains the difference between the results of section 4.2.3.3 and the results reported by the authors, as no information was given regarding the wall or air temperatures at the beginning of the different inlet temperature response tests.

Additionally, Xia et al. (2012) defined L (equation (4-16) as the buried depth of heat exchangers while Di Donna et al. (2017), when reproducing the field test numerically, defined it as the length of the pipe. As the depth of the wall and the length of the pipe are 38 m and 76.25 m, respectively, assuming the wall depth as L, results in twice the heat transfer rate computed by the numerical models, a significant shift from the results of the field test.

4.3 Validation against existing numerical study

Since there are few numerical analyses of energy walls using FEFLOW, the parametric study reported by Di Donna et al. (2017) and presented in section **Erro! A origem da referência não foi encontrada.**, was reproduced in two additional sets of simulations. These will be undertaken considering the previous assumptions regarding the mesh refinement and time step prescriptions and will validate them not only in longer simulation times but also in more complex heat exchanger pipe layouts. The analyses will focus on run number 1 and 2 (Table 3-4).

4.3.1 Geometry and material properties

The wall geometry and the heat exchanger pipe layout are the same for the two runs: wall thickness, T_w = 0.8 m, wall depth, D_w = 20 m, excavation depth, D_e of 16 m ($R = D_w/D_e$ = 1.25), and a 1,5 m half-panel width (Figure 4.13); the heat exchanger loop consists of 6 interconnected vertical pipe branches located on the soil side which are spaced at 0.25 m centres in the plane of the wall with a concrete cover of 50 mm (run 1) or 100 mm (run 2) and each pipe has a diameter of 25 mm. Figure 4.13 shows the model geometry and the heat exchanger pipe layout. The horizontal pipe branches, at the bottom of the

wall, are located 0.5 m above the wall foot. No information was given regarding the distance between the horizontal pipe branches, at the top of the wall, and the top boundary. Thus, the same value of 0.5 m was assumed.

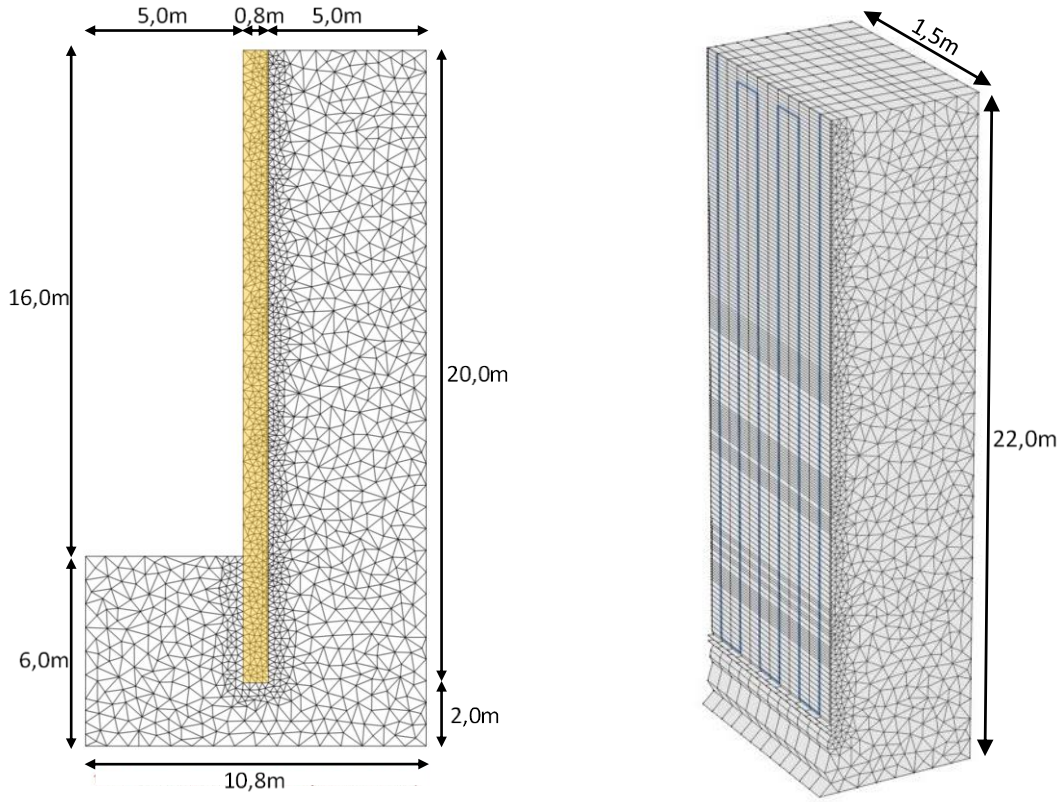

Figure 4.13 - Model geometry with heat exchanger pipe layout.

4.3.2 Boundary conditions, initial conditions and mesh

A constant inlet temperature was set to 20ºC during a simulation time of 60 days, with an initial ramp-up from 12ºC to 20ºC during the first 5 min. The initial soil temperature was set to 12ºC. As there was no information regarding the initial wall temperature, the same value was adopted for the wall. Additionally, a 12ºC constant temperature BC was applied to the right, left and bottom boundaries of the model. As can be seen in Table 3-4, the value of ΔT, the difference between the initial soil temperature and the constant temperature BC on the excavation plane, exposed wall face and top boundary, and the value of v, the fluid velocity, are different for the two runs. Therefore, for run 1 and 2, the temperature BC were set to 14ºC and 18ºC, and the fluid velocity was set to 0.2 m/s and 1.2 m/s, respectively. Figure 4.14 presents the initial soil and wall temperature, the defined constant temperature BC and fluid velocities assigned to the inlet nodes, for the two runs. The set of performed simulations is described in Table 4-5. In all of the schemes, a distance between slices of 0.125 m was adopted to simplify the implementation of the heat exchanger loop elements and to prevent element distortion, i.e. choosing a lower distance between slices would require a higher degree of refinement at the plane, which would increase simulation time and could lead to inaccuracy, as seen in the previous section; conversely, adopting a higher distance between slices, compatible with the spacing between pipe branches, would

require a lower degree of refinement at the plane and just one element between two pipe branches (0.25m), which can also lead to inaccuracy.

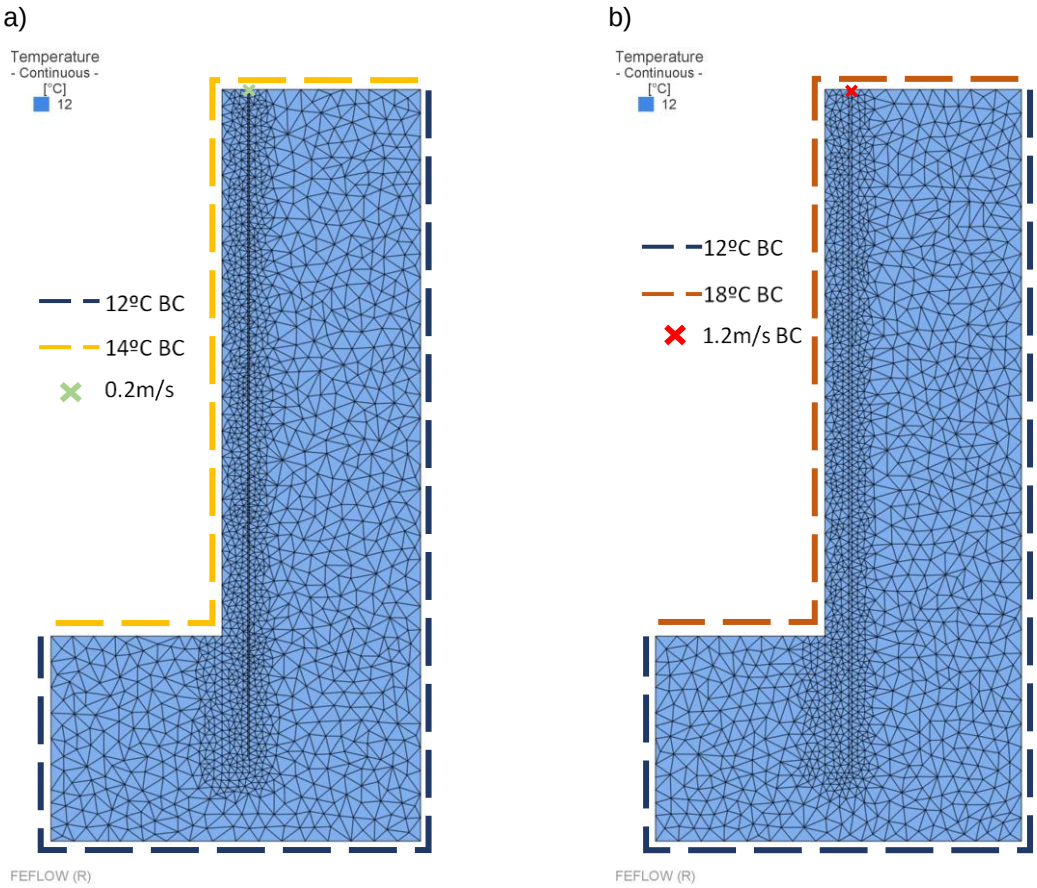

Figure 4.14 - Initial soil temperature, constant temperature boundary conditions and fluid velocity: a) run1; b) run2.

Table 4-5 - Description of the five simulation schemes adopted for validation of the parametric study of Di Donna et al. (2017).

Scheme	Run number from Di Donna et al. (2017)	# Nodes per slice	Pipe inner diameter, d_i [mm]	Prescribed additional time steps
I	1	1643	25	-
II	1	1643	20.4	-
III	2	2475	20.4	-
IV	2	2475	20.4	75 (between 6min and 80min)
V	2	1504	20.4	75 (between 6min and 80min)

4.3.3 Results and discussion

The heat transfer rate per wall surface area, q [W m^{-2}] can be calculated from Q (4-15) as:

$$q = \frac{Q}{A_w} \tag{4-18}$$

Where A_w [m^2] is the total wall surface area on the retained soil side (30 m^2 in this case).

As stated previously, the reported heat exchanger pipe diameter was 25 mm. Though, no information was given about the inner diameter of the pipes. The scheme I aims to reproduce run 1 from the parametric study of Di Donna et al. (2017) with an inner pipe diameter of 25 mm. Alternatively, scheme II reproduces the previous one but assuming an inner diameter of 20.4 mm, i.e. a pipe wall thickness of 2.3 mm, as in the previous section. From the results presented in Figure 4.15 and Figure 4.16 (semi-logarithmic graphs), it is possible to conclude that the inner pipe diameter assumed by the authors is 20.4mm.

The results of schemes III, IV and V reveal that: the higher fluid velocity prescribed on these schemes (1.2 m/s) demands additional time steps in the first stages of the simulation, which is not so evident in schemes I and II, with lower fluid velocity (0.2 m/s). Additionally, for the same time step history, moving from the finer mesh of scheme IV to the coarser one of scheme V, a better agreement is achieved at the early simulation times. This is in accordance with the results of the previous section and will be taken into consideration in the numerical analyses of the following chapter.

In the parametric study reported by Di Donna et al. (2017), the parameter values were defined for each run by changing one or more variables at the same time as the aim was to normalise the effect of each parameter on the heat transfer rate at different simulation times and not so much the heat transfer increase or decrease due to a specific parameter change. Therefore, reproducing run number 1 and 2 individually prevents a direct quantification of e.g. fluid velocity on the heat transfer rate as the concrete cover, concrete thermal conductivity and BC applied to the exposed wall surface also change.

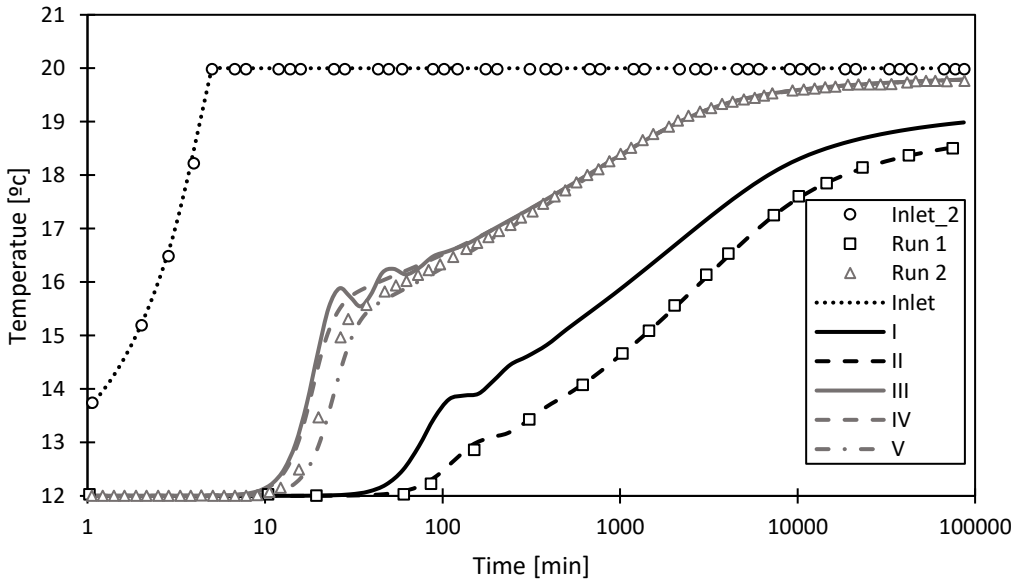

Figure 4.15 – Outlet temperature for the five simulation schemes. Original results from Di Donna et al. (2017).

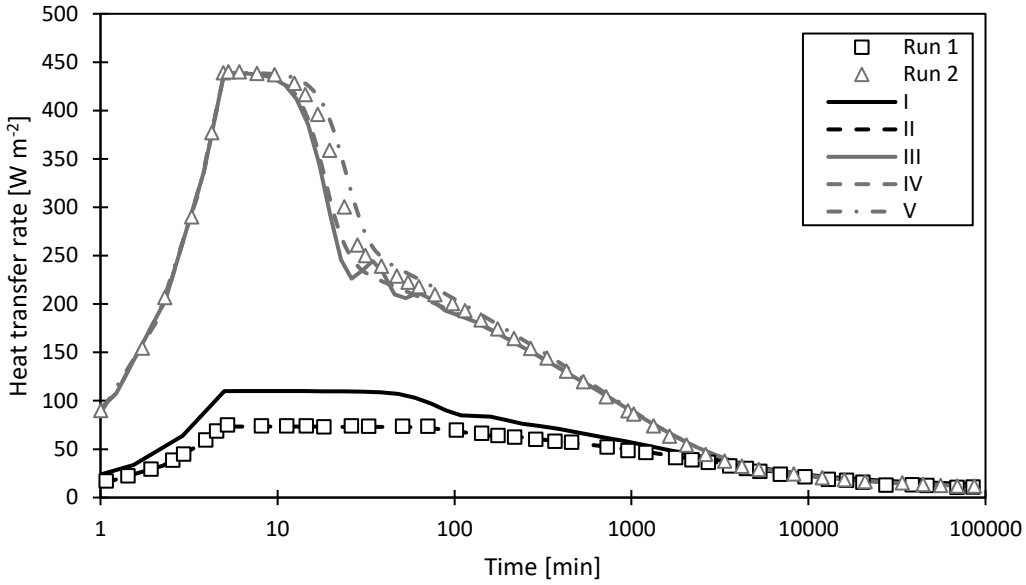

Figure 4.16 - Heat exchange power per wall surface area for the five simulation schemes. Original results from Di Donna et al. (2017).

Oscillations resulting from convergence problems are only visible at lower simulation (Figure 4.15 and Figure 4.16) and do not impact the long-term results, as shown by Figure 4.17. Additionally, the five simulation schemes are in good agreement with the long term numerical results of Di Donna et al. (2017) which indicates an adequate model assembly. The largest differences between the heat transfer rates of simulation schemes II and V and the numerical results reported by Di Donna et al. (2017) are observed for lower simulation times, as presented in Table 4-6. A 11.8% decrease in heat transfer rate at 60 d is observed from scheme II to V, which can be explained by the lower temperature BC assigned to the exposed wall surface and lower concrete thermal conductivity of scheme II (run 1 of Di Donna et al. (2017)), that according to the authors are the two parameters that have a higher impact on the heat transfer rate at 60 d (Figure 3.13). Additionally, the concrete cover and fluid velocity are said to be the parameters with the lowest impact.

Table 4-6 - Summary of the heat transfer rates of schemes II and V for 3 d, 5 d, 30 d and 60 d against the results reported by Di Donna et al. (2017).

Heat Transfer Rate [W/m²]				
	3 d (4320 min)	**5 d (7200 min)**	**30 d (43200 min)**	**60 d (86400 min)**
Run 1 Di Donna et al. (2017)	**30.8**	**24.6**	**15.1**	**13.3**
Scheme II	31.5 (+2.3%)	25.5 (+3.7%)	14.9 (-1.3%)	13.3 (0.0%)
Run 2 Di Donna et al. (2017)	**33.5**	**24.8**	**13.9**	**11.8**
Scheme V	34.4 (+2.7%)	26.2 (+5.6%)	14.0 (+0.7%)	11.9 (+0.8%)

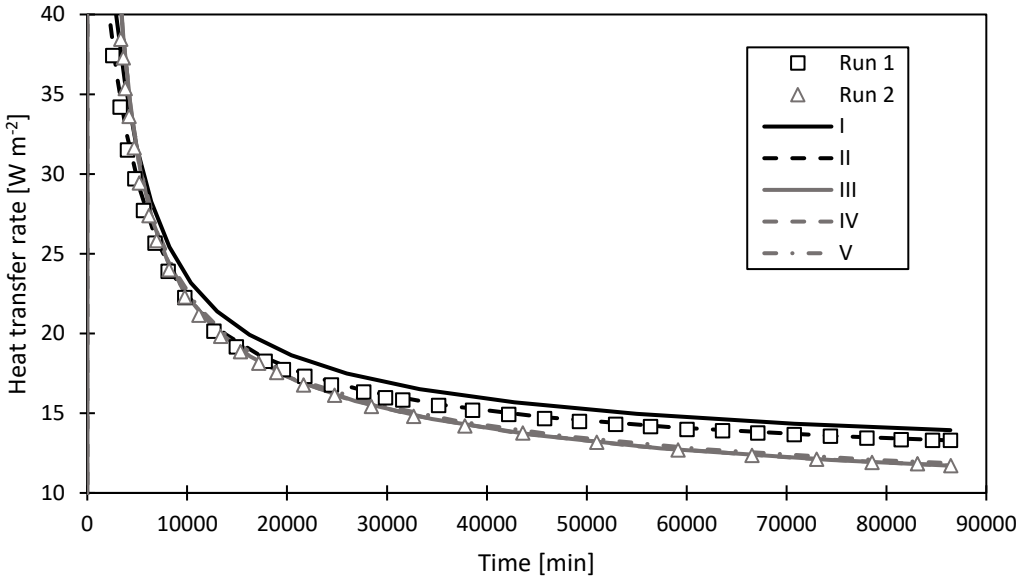

Figure 4.17 - Heat exchange power per wall surface area for the five simulation schemes. Run 1 and Run 2 results from Di Donna et al. (2017).

4.3.4 Conclusions

The previous analyses validate the sensitive behaviour of the outlet temperature and indirectly, the heat transfer rate, to the time step choice, as demonstrated in section 4.2. Higher flow rates in the pipes, due to higher diameter (Scheme I) or to higher fluid velocity (Scheme III) translate to convergence problems at the beginning of the simulation, solved through the prescription of additional time steps. The response behaviour to the mesh is also in accordance with the previous section, in which the coarser mesh better approximates the results of Di Donna et al. (2017) early in the simulation. At higher simulation times, there are no significant differences between the results of the two meshes.

5 Numerical analysis: parametric study

This chapter focuses on the numerical simulation of energy walls through a parametric study. As stated in previous chapters, the thermal behaviour of energy walls is complex to assess due to a high variability of parameters. The following parametric study aims to better understand how the thermal performance of energy walls is impacted by:

- Wall geometry;
- Heat exchanger distribution/density;
- Soil thermal conductivity;
- Thermal boundary conditions and the interior space;
- Thermal load;

5.1 Numerical model

5.1.1 Wall geometry

Diaphragm wall geometry presents some variability, mainly depending on the purpose of the structure in which they are implemented. Table 5-1 summarizes the diaphragm wall geometries of some studies presented previously where it is possible to see wall depths between 15 m and 38 m, as well as wall wall thicknesses between 0.8 m and 1.2 m.

Table 5-1 - Summary of diaphragm wall geometries.

Reference	Wall depth, D_w [m]	Excavation depth, D_e [m]	D_w/D_e	Panel width, W [m]	Wall thickness, T_w [m]
Amis et al. (2010)	36.0	24.0	1.50	3.3	0.8
(Xia et al. (2012)	38.0	18.5	2.05	2.25	1.0
Angelotti & Sterpi (2018)	15.2	10.8	1.49	2.4	0.5
Di Donna et al. (2017)	20.0	10.0 – 16.0	2.0 – 1.25	1.5	0.8 – 1.2
Barla et al. (2020)	15.5	9.5	1.63	2.5	0.8

To assess the impact of the geometry on the thermal performance of the wall, three different wall geometries were defined. For each of them, a set of parameters has to be prescribed as shown by Figure 5.1 a). The aim was to reproduce the geometry of three implementation scenarios for energy diaphragm walls: the first and the second being a typical underground carpark or building basement geometry (Dw/De = 1.25 – 1.5); the third being a typical underground metro station wall geometry (Dw/De = 1.17). Table 5-2 introduces the values of each wall parameter for the three geometries considered in the parametric study. A constant value for the wall base depth was adopted.

Table 5-2 - Wall geometry parameters assumed for the parametric study.

Geometry	Wall depth, D_w [m]	Excavation depth, D_e [m]	Panel width, W [m]	Wall surface area A_w [m²]	Wall thickness, T_w [m]	Slab thickness, T_s [m]
G1	15	10	1.6	24	0.6	0.6
G2	25	20	1.6	40	0.9	0.9
G3	35	30	1.6	56	1.2	1.2

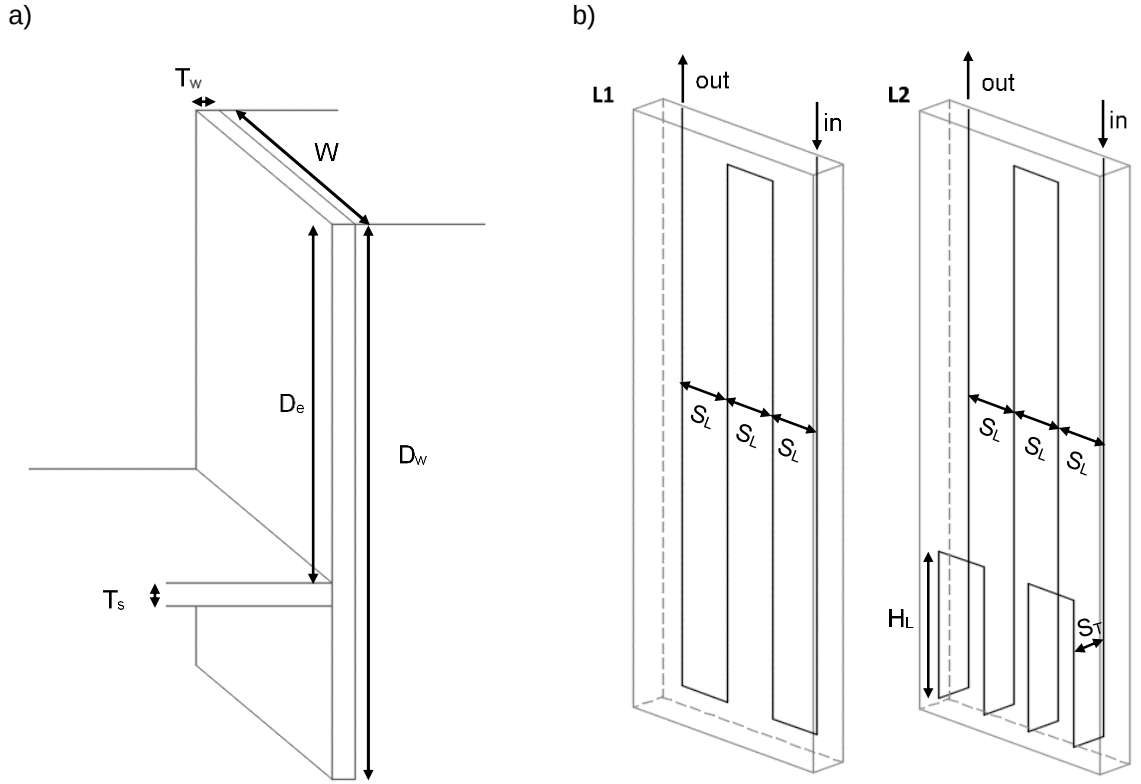

Figure 5.1 - Wall and heat exchanger loop geometry parameters for the parametric study.

5.1.2 Heat exchanger layout

There are multiple heat exchanger loop layouts presented in literature, mainly resulting from numerical analyses aiming to maximize the heat extraction rates of energy walls. Though, as seen in Section 3.2.1, the layout that maximises the heat exchange is not always the simpler to implement in the construction phase. Considering this, two W-shaped heat exchanger loop layouts were defined (Figure 5.1 b)). This W-shaped layout should not impact in a significant way the construction sequence and programme, and is typical of implemented solutions, e.g. Amis et al. (2010). A longitudinal spacing between vertical pipe branches, S_L, of 0.4m was adopted considering there is no significant thermal performance increase from adopting a spacing lower than about 0.3 m (Adam & Markiewicz, 2009; Makasis & Narsilio, 2020). A concrete cover to the pipes, C, of 0.1 m was also adopted as this is a typical target value used in design for structures constructed in contact with the ground and a distance of 1 m from the horizontal pipe branch at its highest point and the wall top boundary was specified.

Considering the work of Sterpi et al. (2018) that reports an increase of 15.8% in performance from adopting an enhanced layout that maximizes the heat transfer in the embedded part of the wall, a heat exchanger layout with that assumption was created (L2). The transverse spacing between vertical pipe branches, S_T on the heat exchanger loop L2, is defined with respect to the wall thickness, T_W, and to the concrete cover to the pipes, assumed on both faces of the wall (soil and expose face); the height of the loop on the embedded part of the wall, H_L, is defined taking into consideration a 0.5 m distance from the bottom slab face.

$$S_T = T_W - 2C \tag{5-1}$$

$$H_L = D_W - D_e - T_S - 0.5 \tag{5-2}$$

The exterior diameter of the heat exchanger pipes, d_o, was fixed at 25 mm, with a wall thickness, t_{pw} , of 2 mm, which correlates to an inner diameter, d_i, of 21mm and a cross sectional area, A, of 346.36 mm^2.

5.1.3 Material properties

The material properties that need to be defined are those for the soil, geostructure and heat carrier fluid. These were defined as bulk values, without the need to compute the solid and water phase properties through equations (4-12) to (4-14), as stated in section 4.2. Table 5-3 lists the thermo-physical properties of the materials, assumed for the parametric study.

Table 5-3 - Material Properties assumed in the parametric study.

	Soil	**Geostructure**	**Heat carrier fluid**
Bulk density, ρ [kg m^{-3}]	2000	2500	1000
Bulk specific heat capacity, c [J kg^{-1} K^{-1}]	1000	900	4200
Bulk volumetric heat capacity, $c\rho$ [MJ m^{-3} K]	2.0	2.25	4.2
Bulk thermal conductivity, λ [W m^{-1} K^{-1}]	1.0/2.0/3.0	2.0	0.6

The soil thermal conductivity will assume values of 1.0, 2.0 or 3.0 W/m K, depending on the run, to evaluate the impact of this soil parameter in the thermal performance of the system. All of the other material parameters are constant throughout the performed analyses. While the concrete thermal conductivity could become an important parameter in the long term Di Donna et al. (2017), it was not considered in the parametric analysis. The concrete parameters will be assigned to the wall and slab region.

5.1.4 Initial temperatures and boundary conditions

The initial soil and wall temperatures were defined as 17ºC, considering the average air temperature in Lisbon (see section 2.2). Given that the simulation length of the analyses was set to 3 years (1095 days), a set of varying temperature boundary conditions were established. Table 5-4 presents the temperature ranges of the inlet, interior space and exterior boundary conditions, the boundaries in which will be

assigned (Figure 5.2) and the equation that describes the sinusoidal profile. The values in bold refer to the baseline values. As can be seen, two additional inlet temperature profiles were defined, one with an average value of 20 ºC and the other with an average value of 14 ºC, alongside an additional interior space boundary condition, with an average value of 23 ºC. These will be considered in the parametric analysis presented in sections 5.3.3 and 5.3.5.

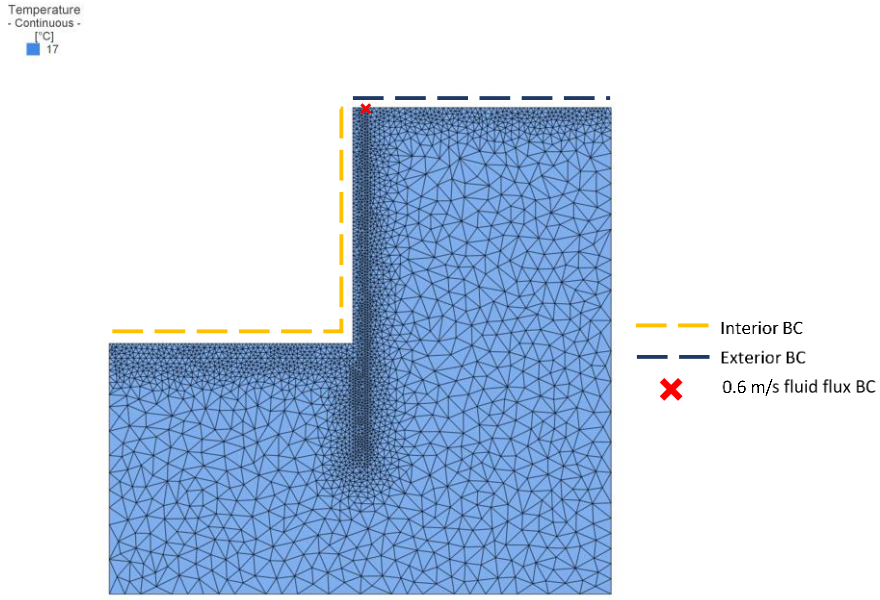

Figure 5.2 - Boundary conditions applied to the parametric study models.

Table 5-4 - Temperature boundary conditions for the parametric study.

	Assigned boundary	Case	Temperature [ºC]	Equation
Inlet	Inlet node	**In_1**	**17 ± 10**	$T_{in}(d) = 17 + 10\sin\left({}^{2\pi d}/_{365}\right)$
		In_2	20 ± 7	$T_{in}(d) = 20 + 7\sin\left({}^{2\pi d + 25.7294 \times 2\pi}/_{365}\right)$
		In_3	14 ± 7	$T_{in}(d) = 14 + 7\sin\left({}^{2\pi d + 25.7294 \times 2\pi}/_{365}\right)$
Interior space BC	Slab and wall surface	**Int_1**	**17 ± 3**	$T_{int}(d) = 17 + 3\sin\left({}^{2\pi d}/_{365}\right)$
		Int_2	23 ± 5	$T_{int}(d) = 23 + 5\sin\left({}^{2\pi d}/_{365}\right)$
Exterior BC	Top boundary	**Ext_1**	**17 ± 6**	$T_{ext}(d) = 17 + 6\sin\left({}^{2\pi d}/_{365}\right)$

The sinusoidal profile was adopted to bring the numerical analyses closer to the operation conditions of energy walls, since the heating and cooling demand imposed is dependent from the external air temperature that can be approximated by a sinusoidal periodic function. Figure 5.3 shows the temperature profiles of the inlet temperature and boundary conditions defined previously, for the three years of simulation.

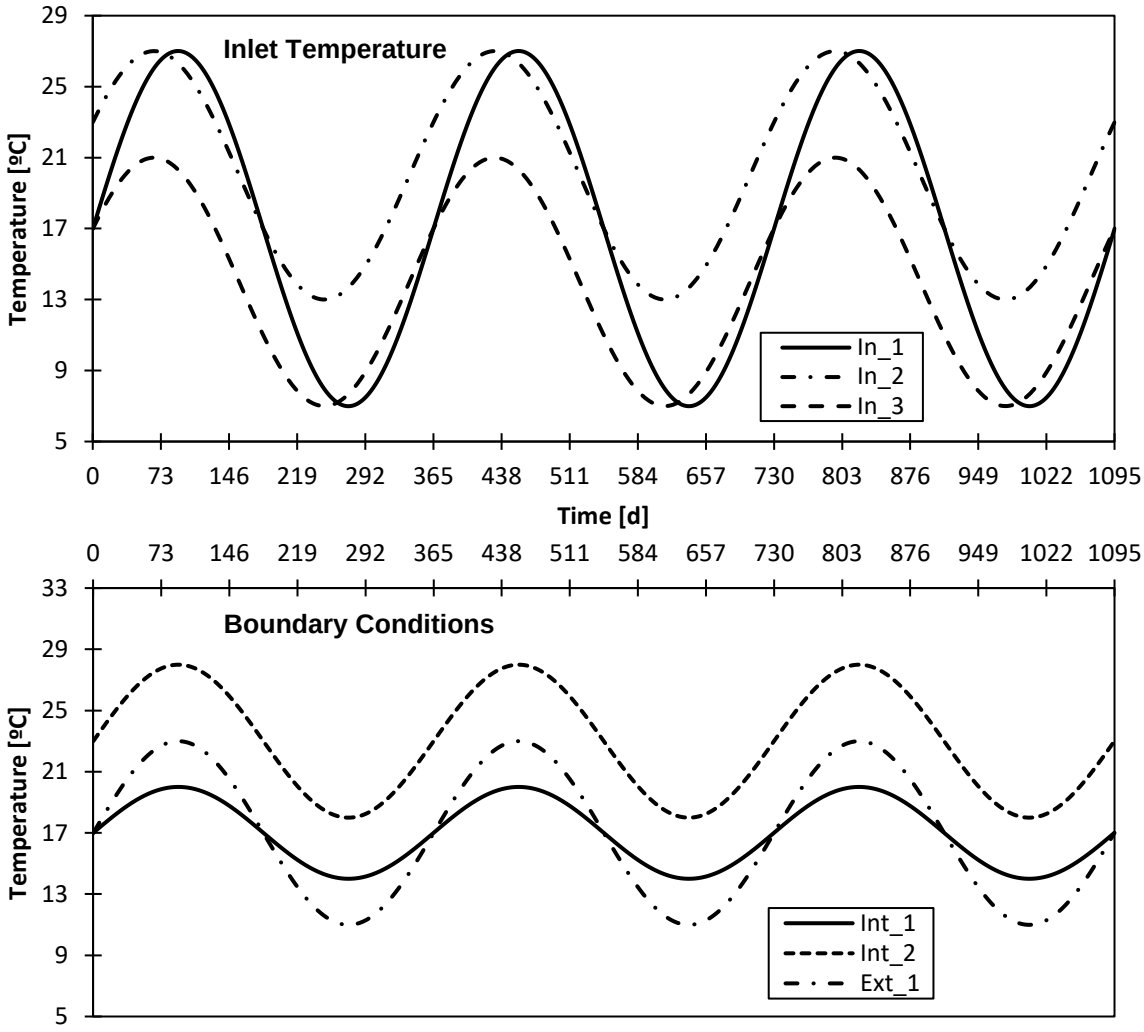

Figure 5.3 - Temperature profiles for the parametric study.

Additionally, the boundaries with no boundary condition assigned are adiabatic by default, which means that no heat flux will occur through them and the temperature at those nodes can change freely. Therefore, these boundaries were checked to be far enough from the wall not to have greatly affected the results, as will be presented in section 5.2.2.

A fluid flux boundary condition was defined at the inlet and outlet node of the heat exchanger loop, following the methodology described in Section 4.1.1. A flow velocity, v, of 0.6 m/s was assigned, in accordance with Xia et al. (2012) (0.25 to 1.5 m/s), Di Donna et al. (2017) (0.2 to 1.2 m/s) and Barla et al. (2020) (0.6 m/s). Considering the heat exchanger pipes geometry and the flow velocity, the Reynolds number can be calculated through the equation:

$$R_e = \frac{\rho_w v d_i}{\mu} \tag{5-3}$$

Where ρ_w is the water density (1000 kg/m^3), v is the flow velocity (0.6 m/s), d_i is the inner diameter of the pipe (0.21 m) and μ is the dynamic viscosity of the fluid (1.002 kg/(m s)), resulting in a Reynolds number of 12575, i.e. turbulent flow conditions occur inside the pipes which is optimal for heat transfer.

5.1.5 Overview of the cases

The parametric study will be performed considering what was described in previous sections. Table 5-5 summarises the combination of parameters in each simulation run of the baseline analysis, defined in terms of the inlet and boundary conditions' temperature profiles presented in Table 5-4 in bold. A case name was defined for each simulation run, containing the wall geometry, heat exchanger layout and the soil thermal conductivity considered for the run, and assuming the baseline values for the inlet and boundary conditions temperature profiles mentioned previously, thus making it easy to identify and compare the results. The presented cases will serve as reference to additional simulations that will be defined throughout the parametric analysis.

Table 5-5 – Baseline analysis cases details.

Wall Geometry	Heat Exchanger Layout	Boundary Conditions	Soil Thermal Conductivity, λ [W m^{-1} K^{-1}]	Case
G1	L1	Baseline	1.0	G1_L1_1.0
			2.0	G1_L1_2.0
			3.0	G1_L1_3.0
	L2	Baseline	1.0	G1_L2_1.0
			2.0	G1_L2_2.0
			3.0	G1_L2_3.0
G2	L1	Baseline	1.0	G2_L1_1.0
			2.0	G2_L1_2.0
			3.0	G2_L1_3.0
	L2	Baseline	1.0	G2_L2_1.0
			2.0	G2_L2_2.0
			3.0	G2_L2_3.0
G3	L1	Baseline	1.0	G3_L1_1.0
			2.0	G3_L1_2.0
			3.0	G3_L1_3.0
	L2	Baseline	1.0	G3_L2_1.0
			2.0	G3_L2_2.0
			3.0	G3_L2_3.0

5.2 Sensitivity analyses

5.2.1 Mesh and time-step sensitivity analysis

A mesh and a time-step sensitivity analysis was performed to assist in the definition of the mesh parameters. Considering what was presented in sections 4.2 and 4.3, a layer width of 0.1 m was adopted in all of the performed sensitivity analyses, resulting in 16 layers (17 slices) for a model width of 1.6 m. The case ***G1_L1_2.0*** was considered in all of the simulations.

A set of two different meshes (Table 5-6) and two different time-step lengths (Table 5-7) have been defined. The two different time steps were defined in terms of maximum time-step length conversely to the prescription of additional time-steps adopted in sections 4.2 and 4.3 since the system is in equilibrium at the beginning of the simulation and no convergence problems arise.

The “minimum angle” defines the minimum angle for each triangular element, with higher values resulting in a more regular mesh and lower values resulting in a higher number of elements generated. This parameter was tested and with values higher than 30º the mesh was impossible to generate due to the high computational resources needed, therefore 20º seemed a good compromise. The “polygon gradation” and “line gradation” controls the smoothness between the coarser elements of the mesh and the elements closer to the refinement borders. In the parametric study, the wall, slab and top boundary (polygons) and the heat exchanger loop (line) were defined as refinement areas as they will experience higher temperature gradients. Additionally, the “polygon target size” and “line target size” specifies the maximum side length of the elements in contact with the refined areas. The generated meshes resulted in elements with a side length of 0.1 m near the heat exchanger loop (M1 and M2), 0.16 m (M1) and 0.1 m (M2) on the slab, exposed wall face and top boundary and 0.65 m (M1 and M2) on the left, right and bottom boundaries of the model.

Table 5-6 - Mesh and time-step sensitivity analysis - mesh properties.

Mesh	Minimum Angle [º]	Polygon Gradation	Polygon target size [m]	Line Gradation	Line Target Size [m]	No. Elements per layer
M1	20	4	0.30	2	0.2	4732
M2	20	6	0.15	2	0.2	9987

Table 5-7 - Mesh and time-step sensitivity analysis - time-step properties

Time-Step	Maximum Time-Step Length [d]
T1	7
T2	0.5

From Table 5-8 it is possible to conclude that by reducing the time-step length by a factor of 14 (from time-step type T1 to type T2) the heat transfer rate increase is insignificant. Additionally, by enhancing the mesh refinement by a factor of 2 (from mesh type M1 to mesh type M2), the heat transfer rate decreases by about 1.55%, at the cost of an analysis duration 10 times longer.

Table 5-8 - Mesh and time-step sensitivity analysis results.

	Average peak heat transfer rate, q [W m^{-2}]		Difference to M1|T1	
	Cooling	**Heating**	**Cooling**	**Heating**
M1|T1	21.09	-20.67	-	-
M1|T2	21.10	-20.68	0.061%	0.063%
M2|T2	20.76	-20.35	-1.54%	-1.55%

Therefore, the M1|T1 combination was chosen as a ponderation between the numerical results accuracy and the analysis duration. The details regarding the number of triangular prismatic elements and nodes are presented in Table 5-9 for the three wall geometries defined in Section 5.1.1, after mesh type M1. Note that the increasing number of elements and nodes from geometry 1 to geometry 3 is only related to the fact that geometries with higher dimensions demand higher domain dimensions, which translates to more elements and nodes.

Table 5-9 - Mesh elements and nodes for the wall geometries of the parametric study.

Geometry	Mesh Elements	Mesh Nodes	Layer width [m]	Elements/layer	Elements/slice
G1	81680	45577	0.1 (16 layers)	5105	2681
G2	110496	61540	0.1 (16 layers)	6906	3620
G3	142112	78285	0.1 (16 layers)	8882	4605

5.2.2 Domain sensitivity analysis

Following the mesh and time-step sensitivity analysis, a domain analysis was performed to evaluate how the distance between the wall and the right (D_{Wr}) and the bottom (D_{Wb}) boundaries impacts the thermal performance of the wall. Therefore, a set of three different domains, i.e. three different sets of parameters for D_{Wr} and D_{Wb} were defined as listed in Table 5-10. The case ***G1_L1_2.0*** was considered in all of the simulations.

Table 5-10 - Domain analysis - domain properties.

	Distance between the wall and right boundary, D_{Wr} [m]	Distance between the wall base and bottom boundary, D_{Wb} [m]
D1	10.0	5.0
D2	5.0	10.0
D3	10.0	10.0

The results show a peak heat transfer rate average difference (for the three years of simulation) from M1|T1 (defined in the previous section) of:

- -1.47% (cooling) and -1.08% (heating) for domain type D1;
- 0.14% (cooling) and -0.05% (heating) for domain type D2;
- -1.30% (cooling) and -1.10% (heating) for domain type D3;

Which demonstrates that enlarging the distance between the wall and right boundary (D1) has a bigger impact on the thermal performance of the wall than adopting a distance of 10 m from the wall toe (D2), or adopting both (D3). Considering the results, the numerical model geometry was defined as shown by Figure 5.4. The final geometry is in accordance with the domain type D1.

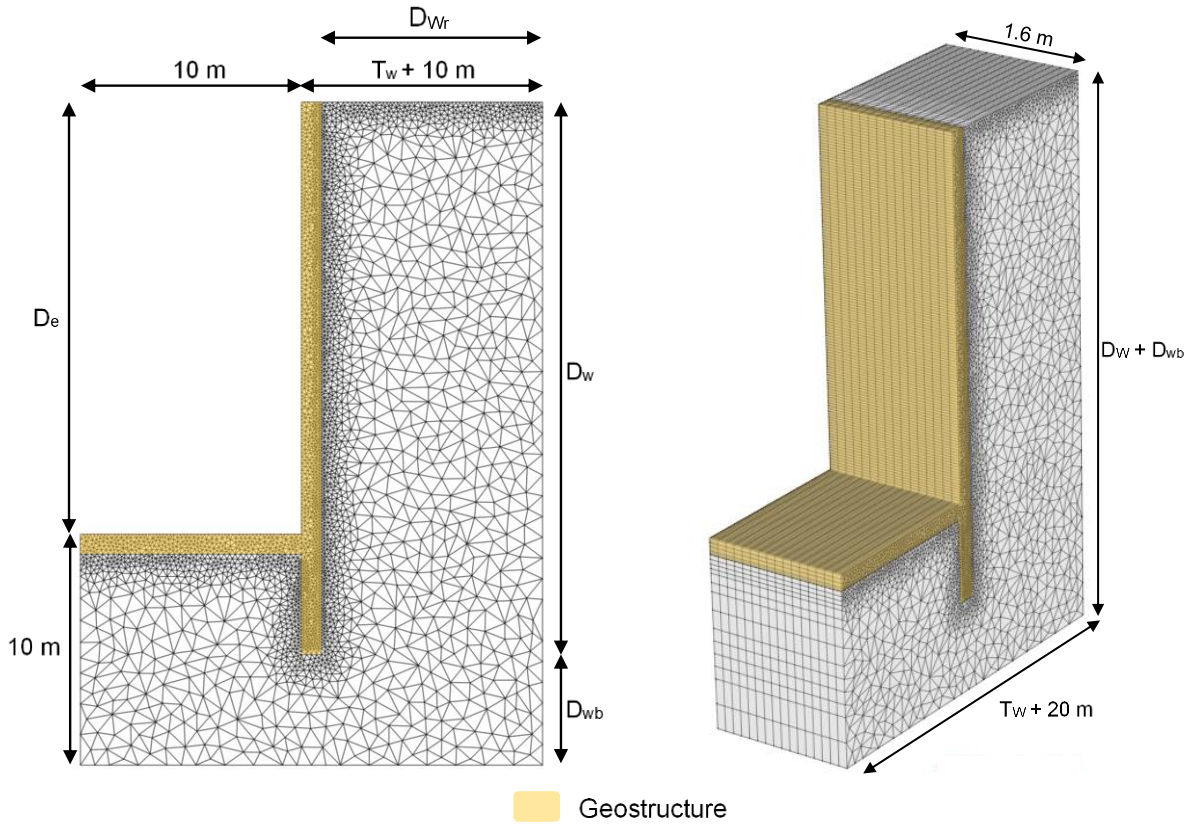

Figure 5.4 – Parametric study model geometry.

5.2.3 Boundary conditions sensitivity analysis

A constant temperature boundary condition of 17ºC, equal to the initial soil temperature, was intended to be defined to the bottom boundary of the model. Though, only after all the parametric study simulation runs it was noticed that this boundary condition was not assigned to the parametric study numerical models. Therefore, an additional simulation was performed, based on case ***G1_L1_2.0*** but with the constant temperature boundary condition assigned to the bottom boundary, resulting in an increase of 0.39% for cooling and a decrease of -0.11% for heating. Figure 5.5 shows the temperature evolution at the bottom boundary of the model, with a decrease in temperature from the first to the last cooling and heating cycles. It is possible that for simulation times higher than 3 years the impact on the thermal performance of the wall would be more noticeable. However, the incremental change in temperature

reduces quickly from the 1st to 2nd and from the 2nd to the 3rd year, which could indicate that it is stabilising.

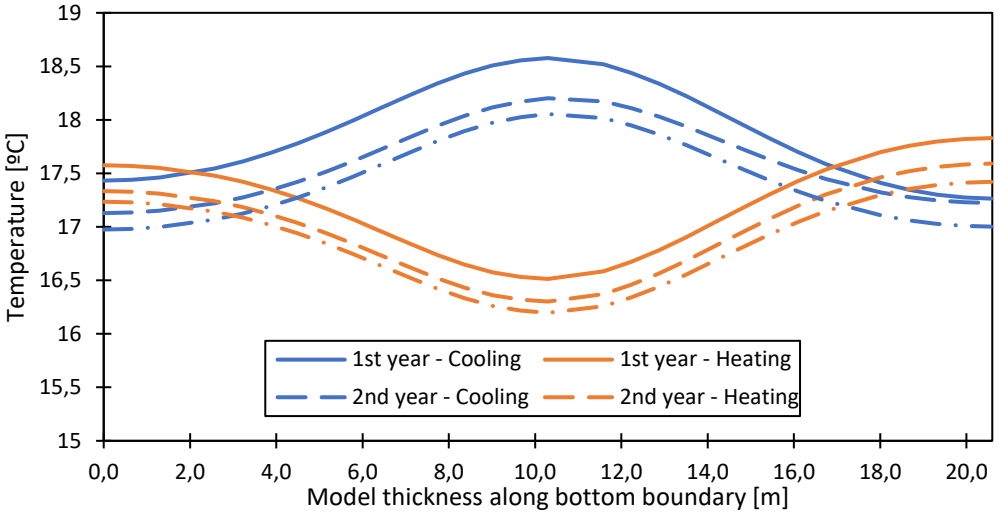

Figure 5.5 - Bottom boundary temperature evolution.

Nevertheless, the results are in line with the domain analysis of Section 5.2.2 that showed that the bottom boundary of the model is far enough to not impact significantly the thermal performance of the wall.

5.3 Parametric analysis

5.3.1 Baseline analysis results

A baseline analysis was defined in section 5.1.5, comprising the geometries, the soil thermal conductivities and the heat exchanger layouts previously defined. Figure 5.6 presents the results of the baseline analysis cases with a soil thermal conductivity of 2.0 W/m K, for the third year of simulation (730 d to 1095 d), in terms of outlet temperature. As can be seen, the outlet temperature evolution for all of the cases describes, as expected, the sinusoidal behaviour imposed by the inlet and boundary condition temperature profiles (Figure 5.3), with small outlet temperature differences between them.

The small differences in outlet temperate are more visible when the results are presented in terms of heat transfer rate per wall surface area, q [W m^{-2}], computed through equation (4-18) but considering Q as:

$$Q = mc_w\,(T_o - T_i) \tag{5-4}$$

Note that in accordance with equation (5-4), positive heat transfer rates refer to the heating operation mode, as outlet temperatures are higher than inlet temperatures, and negative heat transfer rates refer to the cooling operation mode, as outlet temperatures are lower than inlet temperatures. Figure 5.7 shows the heat transfer rate evolution during the three years of simulation and Figure 5.8 shows the same results but only for the period comprising the third year of simulation, from 730 d to 1095 d.

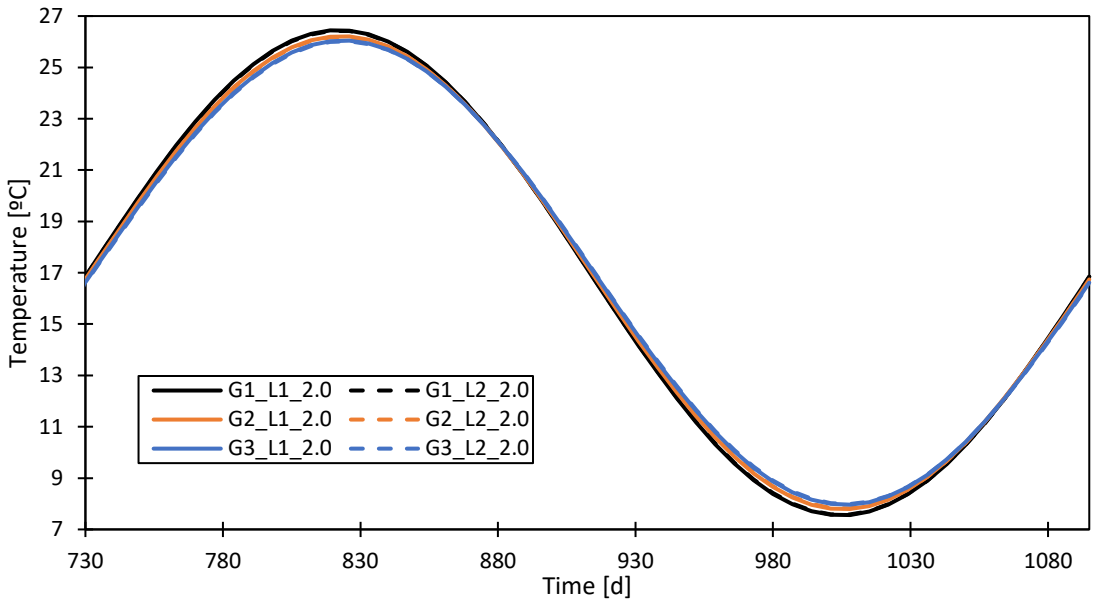

Figure 5.6 - Baseline analysis outlet temperature evolution during the third year of simulation.

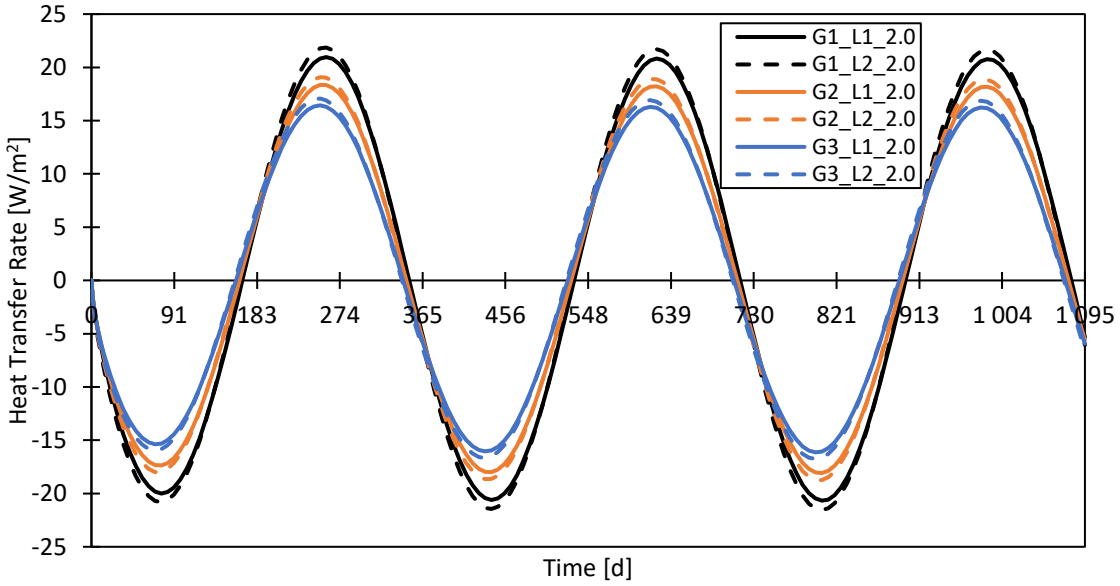

Figure 5.7 - Baseline analysis heat transfer rate evolution.

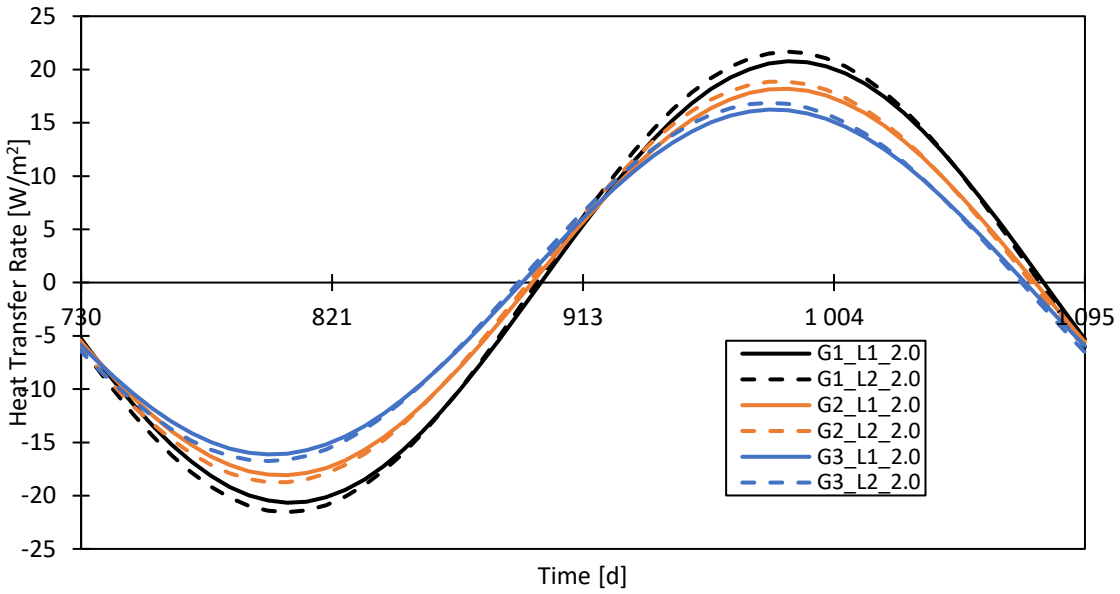

Figure 5.8 - Baseline analysis heat transfer rate during the third year of simulation.

Although only the 2.0 W/m K soil thermal conductivity cases are presented in Figure 5.7 and Figure 5.8, a similar behaviour was identified for the 1.0 W/m K and 3.0 W/m K soil thermal conductivity cases. The results of those cases can be consulted in Appendix B.

5.3.2 Influence of soil thermal conductivity, wall and heat exchanger geometry

As stated previously, the parametric study aims to provide a better understanding regarding the influence of a set of parameters on the thermal performance of energy walls. The first to be discussed are the soil thermal conductivity, wall geometry and heat exchanger layout. This analysis is based on the results of the baseline analysis cases, defined in section 5.1.5, alongside an additional simulation based on case ***G2_L1_2.0***, with a higher embedded depth of 10 m. The distinguished parameter in relation to all of the other cases is the total wall depth that goes from 25 m to 30 m, therefore the case name ***G2_L1_2.0_30*** adopted for this additional simulation. To compare the heat transfer rates from the different geometries, a new parameter, D_b, the embedded depth of the wall below excavation level, was defined, as:

$$D_b = D_w - D_e \tag{5-5}$$

The relationship curves between the heat transfer rate and the soil thermal conductivity as well as between the heat transfer rate and the excavation to wall base depth ratio are presented in Figure 5.9. The left column presents the relationships dependent on the soil thermal conductivity, therefore the case names omit this parameter. The same is applicable to the right column, in which the case names omit the geometry type, as the relationship is dependent on the ratio between De and Db.

As expected, the highest heat transfer rates are achieved for the highest values of soil thermal conductivity. An almost linear relationship is observed between the soil thermal conductivity and the heat transfer rate, in all of the geometries and heat exchanger layouts. For heat exchanger layout L1

specifically, a heat transfer rate increase of 11.1%, 11.3% and 12.5% (heating) and of 11.0%, 11.1% and 12.3% (cooling) is observed for geometries G1, G2 and G3, respectively, through doubling the soil thermal conductivity, translating to an average increase of 11.6% and 11.4% for heating and cooling, respectively. Furthermore, the 50% increase in soil thermal conductivity, from 2.0 W/m K to 3.0 W/m K, translates to an increase in heat transfer rate of 7.4%, 7.5% and 8.1% (heating) and of 7.4%, 7.6% and 8.2% (cooling) for geometries G1, G2 and G3, respectively, resulting in an average increase of 7.7% for both heating and cooling. A similar behaviour is observed for the geometries combined with the heat exchanger layout L2, translating to an average heat transfer rate increase of 13.3% and 13.1% for heating and cooling respectively, from doubling the soil thermal conductivity, and an average increase of 8.9% and 9.0% for heating and cooling respectively, from 2.0 W/m K to 3.0 W/m K. As the heat exchanger layout L2 has a higher area in contact with the ground, the increase in soil thermal conductivity results in a higher increase of heat transfer rate.

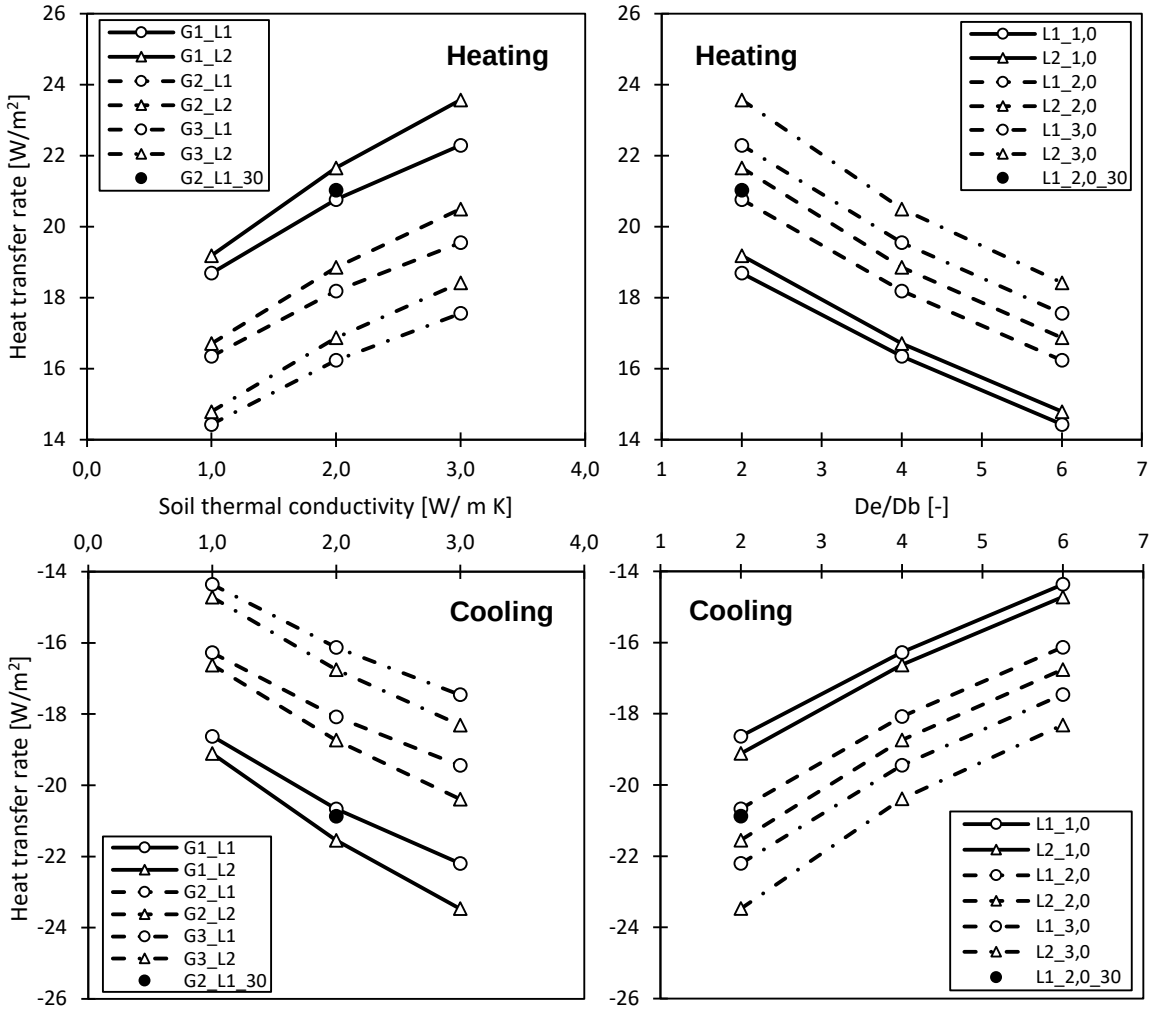

Figure 5.9 - Effect of soil thermal conductivity, wall and heat exchanger geometry.

The heat exchanger layout, as shown by Figure 5.9, also impacts the heat transfer rate but to a lesser degree than the soil thermal conductivity. The influence increases, as the soil thermal conductivity increases. In fact, an average increase in heat transfer rate of 2.4% (1.0 W/m K), 4.0% (2.0 W/m K) and 5.2% (3.0W/m K) is observed between the heat exchanger layout L1 and L2 in heating mode, while an

average increase of 2.4% (1.0 W/m K), 3.9% (2.0 W/m K) and 5.2% (3.0 W/m K), between the heat exchanger layout L1 and L2, is observed in cooling mode. An average increase of 20.1% (L1) and 23.3% (L2) is observed from 1.0 W/m K to 3.0W/m K. Although the direct comparison of results could be erroneous due to the high variability in the parameters used, Sterpi et al. (2020) reports results for a similar set of heat exchanger layouts and wall geometry (De/Db = 2.1), and a soil thermal conductivity of 2.2 W/m K, that show a 5.0% increase in the heat transfer rate per square metre of wall from a layout only on one side of the embedded part of the wall (like layout L1) to a layout on both sides of the embedded part of the wall (like layout L2).

Regarding the wall geometry, the results show that as the depth of the wall increases, from G1 to G3 or from De/Db=2 to De/Db=6, the heat transfer rate per square metre of wall decreases. However, this trend is counteracted by the case ***G2_L1_30*** / ***L1_2.0_30*** in which a total wall depth of 30 m results in a similar heat transfer rate to that of a 25 m total depth wall (G1 or De/Db=2). Namely, it is possible to conclude that the case ***G2_L1_30*** reveals a similar heat transfer rate to ***G1_L1*** for a soil thermal conductivity of 2.0W/m K, as seen in the left column of Figure 5.9, and the case ***L1_2.0_30*** reveals a similar heat transfer rate to ***L1_2.0*** for a De/Db ratio of 2, as seen in the right column of Figure 5.9. This indicates that the wall geometry, specifically the ratio between the exposed part and the embedded part of the wall, plays an important role in the thermal output of the system. Although this geometry was only tested with a soil thermal conductivity of 2.0 W/m K and the heat exchanger layout L1, a similar behaviour is expected in the other cases considered, i.e. an almost linear relationship with the soil thermal conductivity and the De/Db ratio, with an offset from the results of geometry type G2, if subject to the same parameter variations. This is due to a higher embedded depth that increases the ground contribution to the resulting heat transfer rate. Figure 5.10 presents the heat transfer rate results per metre of depth of the wall, for the heat exchanger layout L1. When the heat power is normalized against the total depth of the wall, the difference from the heat transfer rate of case ***L1_2.0_30*** to the other set of cases is even more evident. Compared to the case ***L1_2.0*** for a wall depth of 30 m, an increase of 22.2% (heating) and 22.0% (cooling) is achieved.

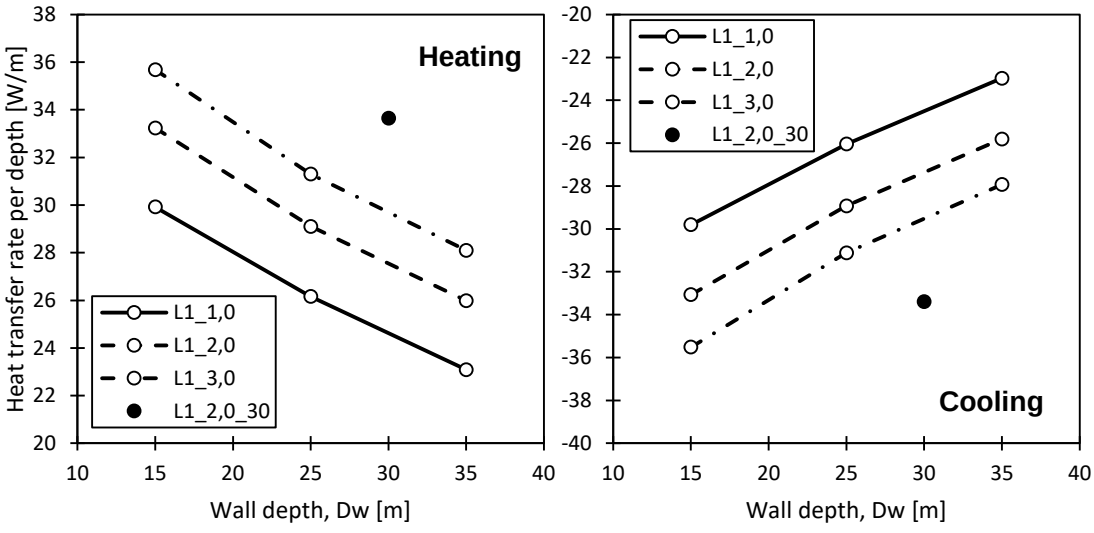

Figure 5.10 - Heat transfer rate per total depth of the wall for heat exchanger layout L1.

5.3.3 Influence of interior space

The BC of the exposed wall face was changed from a variable temperature BC (exterior air temperature) to either an adiabatic BC or a convective heat transfer BC, representing case ***G1_L1_2.0_C*** and ***G1_L1_2.0_A***, respectively. For the former, the numerical model is established without any BC assigned to the slab and exposed wall face nodes, reproducing a scenario were the exposed face of the wall is insulated from the excavated environment. In the case of the convection BC, a variable temperature boundary condition has to be combined with a heat transfer boundary condition. The convective heat transfer coefficient, h, has to be defined, and a value of 10 W/m^2 K was adopted after Bourne-Webb et al. (2016), to simulate moderate air-speeds (0.5 to 2 m/s) inside the excavation space.

Figure 5.11 presents the results for the two considered boundary conditions alongside the heat transfer rate results of case ***G1_L1_2.0*** (variable temperature BC) that are summarized in terms of peak heat transfer rate in Table 5-11. As expected, the convective boundary condition heat transfer rate is in between the two extremes, imposed by the temperature and adiabatic boundary conditions. The results of the adiabatic boundary condition show that almost 42% of the heat output is due to the heat exchange between the wall and the excavated space. On the other hand, the difference between assuming very large air-speeds and moderate air-speeds on the wall surface, i.e. between ***G1_L1_2.0*** and ***G1_L1_2.0_C***, results in a loss of efficiency of almost 13%, which is in accordance with Di Donna et al. (2020) that report a 10% to 12% decrease after assigning a value of h = 2.5 W/m K.

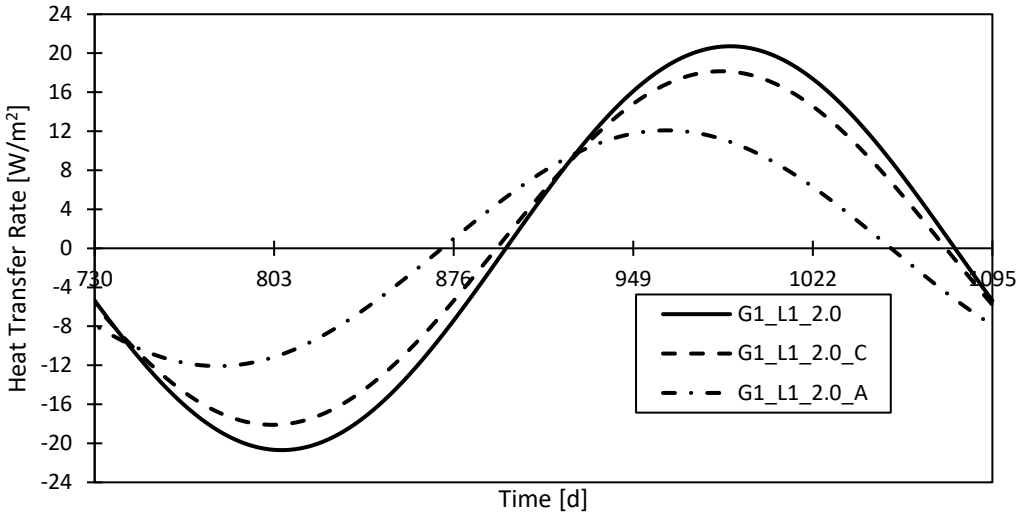

Figure 5.11 - Boundary conditions sensitivity analysis: results for the third year of simulation.

Table 5-11 - Boundary conditions sensitivity analysis - peak heat transfer rate values and comparison with the results of a variable temperature boundary condition (G1_L1_2.0).

	G1_L1_2.0_C		G1_L1_2.0_A	
	Heat Transfer Rate [W/m²]	**Difference to G1_L1_2.0 [%]**	**Heat Transfer Rate [W/m²]**	**Difference to G1_L1_2.0 [%]**
Cooling	-18.10	-12.52	-12.08	-41.61
Heating	18.15	-12.40	12.09	-41.65

An additional set of simulations was established to evaluate the system response to a warmer interior space. Therefore, all of the cases of geometry type ***G3*** and the case ***G2_L1*** (see Table 5-5 in section 5.1.5) were considered. The interior BC was changed to the Int_2 BC, defined in Table 5-4 of section 5.1.4. The evolution of the new and previous interior BC, alongside the inlet temperature is presented in Figure 5.12.

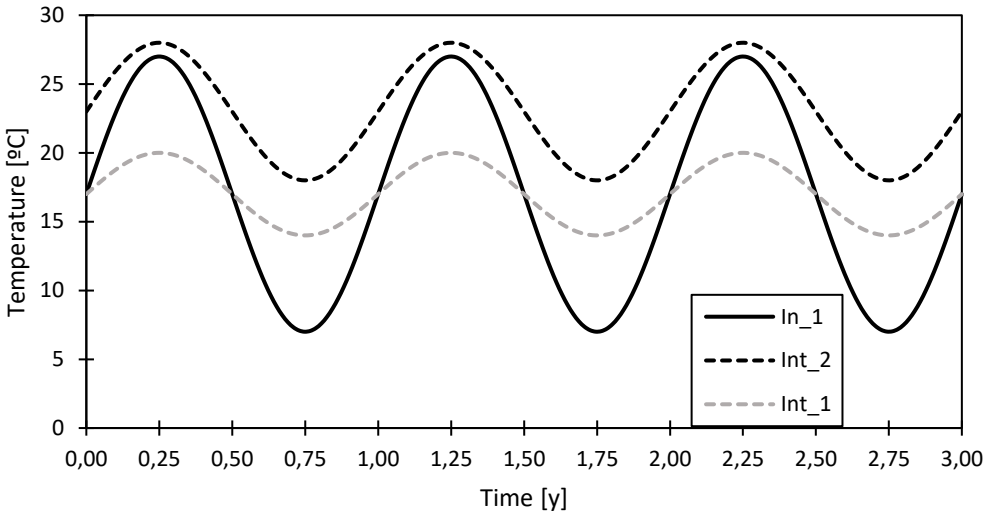

Figure 5.12 - Inlet and interior BC temperature evolution for the influence of the interior space analysis.

The results in terms of heat transfer rate per square metre of wall are presented in Figure 5.13, alongside the results of case ***G3_L1***, the reference case with the interior BC Int_1. As shown, there is a significant increase in the heat transfer rate in heating mode and, conversely, a significant decrease of performance in cooling mode. This confirms what was evident in the temperature BC evolution of Figure 5.12, that the interior BC temperature is always higher than the inlet temperature, which will reduce the cooling system performance. In fact, the cooling provided by the system results from the previous heating operation in which the heat extracted lead to a low temperature field around the wall. That allows for a short cooling period as soon as the inlet temperature increases again, that ceases when the wall and the soil around it reach a thermal equilibrium with the inlet temperature. Consequently, it is possible to conclude that the cooling provided is only due to the storage capacity of the wall and soil and that the interior space do not contribute in a positive way to it. Actually, once the wall is colder than the interior boundary condition, the interior space is contributing in a negative way to the cooling performance of the wall. Table 5-12 present the percentage differences between these set of simulations, with interior BC Int_2, and the baseline analysis simulations, showing an average heat transfer rate increase between 35.6% and 38.7%, in heating mode, and an average heat transfer rate decrease between 61.6% and 69.3%, in cooling mode. It is also noticeable that as the soil thermal conductivity increases, the differences decrease. Once again, this is due to the higher contribution of the soil to the heat performance of the system.

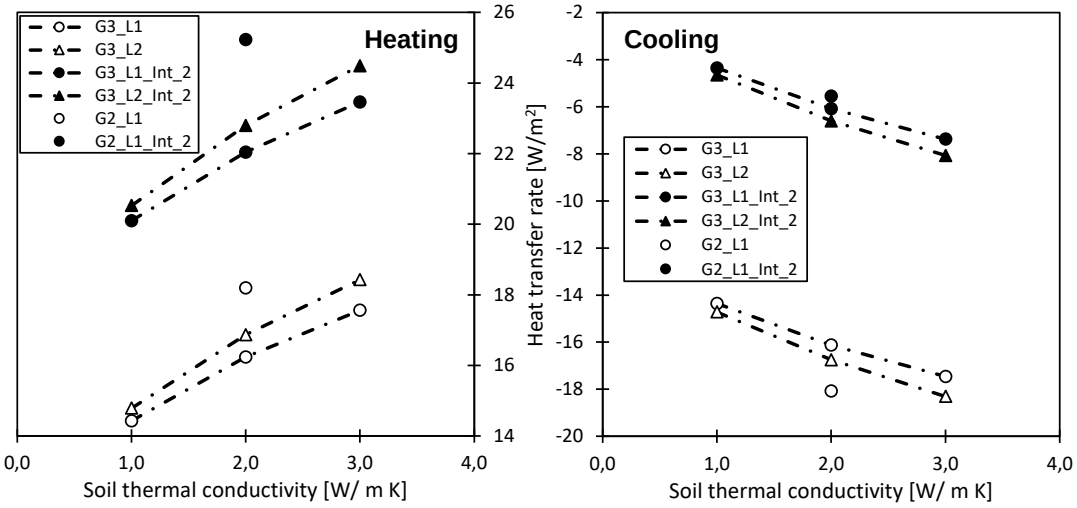

Figure 5.13 - Heat transfer rate results for the interior space analysis.

Table 5-12 - Difference between Int_1 and Int_2 BC.

	G3_L1		G3_L2		G2_L1	
λs	**Heating**	**Cooling**	**Heating**	**Cooling**	**Heating**	**Cooling**
1.0	39.3%	-69.7%	38.8&	-68.4%	-	-
2.0	35.7%	-62.3%	35.2%	-60.6%	38.7%	-69.3%
3.0	33.6%	-57.7%	32.9%	-55.9%	-	-
Average	**36.2%**	**-63.2%**	**35.6%**	**-61.6%**	**38.7%**	**-69.3%**

Two of the previous considered cases had the simulation time extended to 10 years to check if there was some degradation in the heat transfer rate imposed by the warmer interior space since the average value of the BC Int_2 is higher than all of the other imposed temperatures. As can be seen in Table 5-13, no significant drop in thermal performance was observed. With this result, the temperature profiles at 3 m and 25m depth were checked, from the wall face to the right boundary, both with and without the geothermal system activated for the case ***G3_L1_2.0_Int_2***. The temperature profiles are presented in Figure 5.14, for both heating and cooling operation. The temperature profiles for the ten years of simulation (geothermal system activated) can be consulted in Appendix C. From the results at 3 m depth, it is evident that with the geothermal system deactivated, the temperature around the right boundary increases from the first to the third year of simulation. This is even more noticeable at 25 m depth as there is less influence from the top boundary condition. In the case where the geothermal system is activated, the temperature profiles are stable and remain at the temperature registered for the first year of simulation, with the geothermal system deactivated. Therefore, the excessive heat from the interior environment is being absorbed by the heat exchanger loop, which prevents the system saturation in the long term.

Table 5-13 - Heat transfer rate results of G3_L1_2.0 for a simulation period of 10 years.

	Heat Transfer Rate [W/m²]	
	Heating	**Cooling**
G3_L1_2.0_Int_2 (3rd year)	22.04	-6.08
G3_L2_2.0_Int_2 (3rd year)	22.80	-6.60
G3_L1_2.0_Int_2 (10th year)	22.05	-6.07
G3_L2_2.0_Int_2 (10th year)	22.80	-6.60

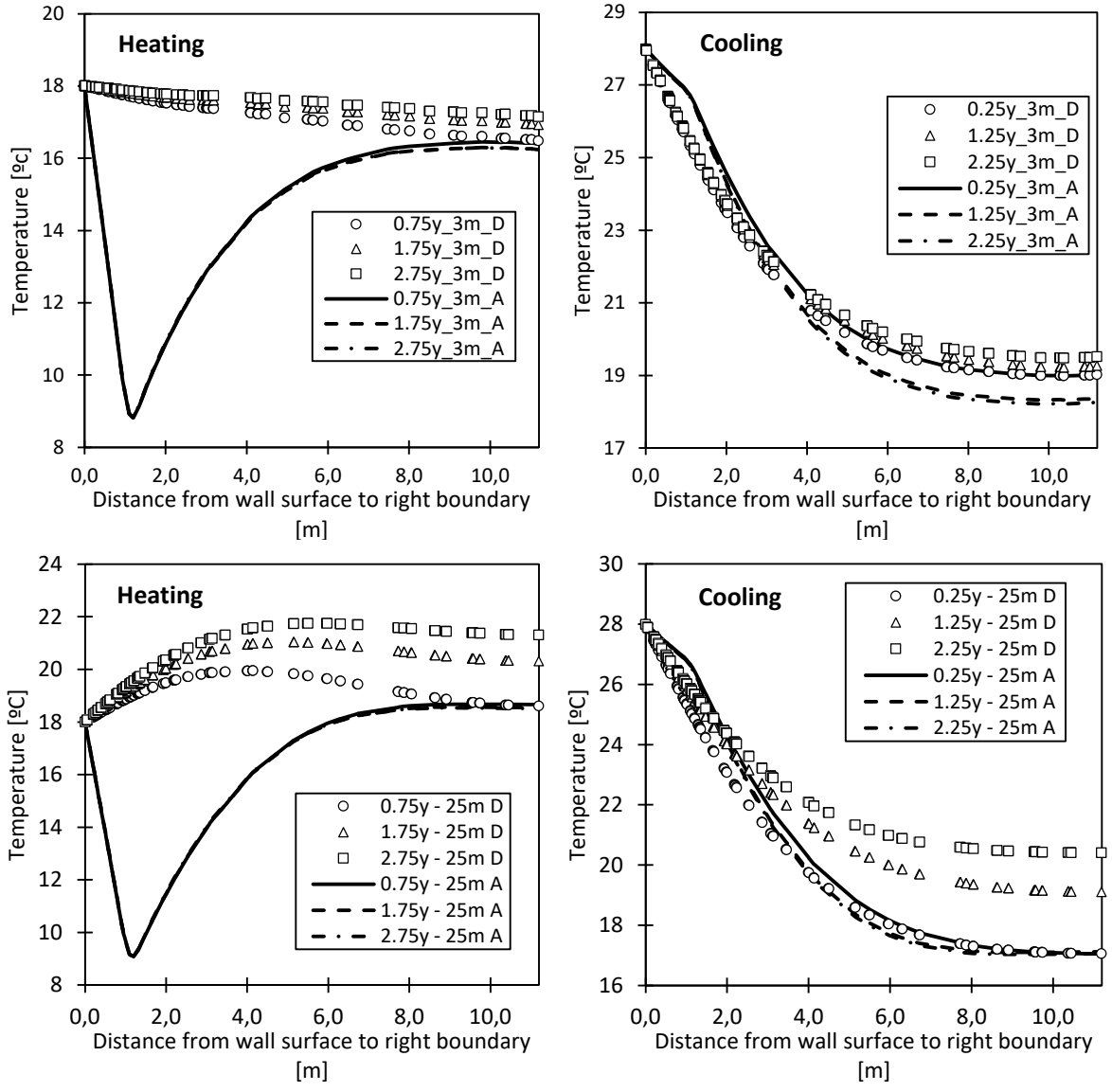

Figure 5.14 - Temperature profiles at 3 m and 25 m for case G3_L1_2.0_Int_2. D refers to geothermal system deactivated; A refers to geothermal system activated;

5.3.4 Influence of top boundary condition

An additional set of simulations was defined based on geometry types ***G1***, ***G2*** and ***G3***, the heat exchanger layout ***L1*** and a soil thermal conductivity of ***2.0*** W/m K to evaluate how the top BC impacts

the heat transfer rate. Namely, if the top BC is somehow responsible for the higher heat transfer rate values computed for the geometries with lower total depth, as it is expected to impact those in a larger degree than it does to the deeper geometries. Therefore, the top BC (Ext_1 defined in Table 5-4, section 5.1.4) was changed to an adiabatic boundary condition, with the case name ***L1_2.0_Atop***.

The results of the heat transfer rate per square metre of wall against the De/Db ratio are presented in Figure 5.15. As seen, the influence is higher for a De/Db ratio of 2, for both heating (0.92%) and cooling (0.72%) modes, than it is for a De/Db ratio of 6 (0.49% in heating mode; 0.34% in cooling mode). Therefore, assuming an adiabatic BC instead of a variable temperature BC seems to produce little impact in the final results. As a result, the higher surface area of the deeper geometries, as well as the depth, seems to be the factors that explain why normalising the exchange power (Q) by the wall area or depth, results in lower heat transfer rates, as the higher values of those parameters overcome the gain in exchange power of the biggest wall geometries.

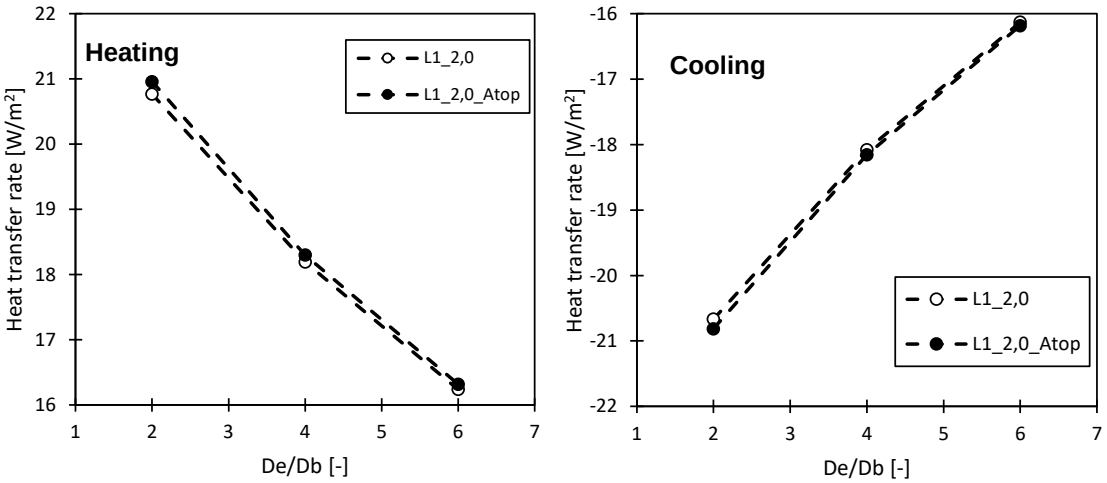

Figure 5.15 - Heat transfer rate results of top boundary condition analysis, for heating an cooling mode.

5.3.5 Influence of inlet temperature

An unbalanced thermal load was imposed to the system by changing the inlet temperature assigned to the case ***G2_L1_2.0***. The two new inlet temperature profiles, ***In_3*** (heating dominant) and ***In_2*** (cooling dominant) were defined in Table 5-4 from section 5.1.4. As a result, the case ***G2_L1_2.0_In_3*** shows a 3.5%, 2.2% and 1.5% increase in hat transfer rate, in heating mode, for the first, second and third year of simulation. As the thermal load is heating dominant, the cooling performance is much lower than that of case G2_L1_2.0 (-67.3%, -60.9% and -59.9% for the first, second and third year of simulation). The case ***G2_L1_2.0_In_2*** shows a high heat transfer rate value at early simulation time due to the high difference in temperature between the inlet and the outlet, therefore not being representative of the first year peak cooling heat transfer rate. In the second and third years, the difference to the case G2_L2_2.0 is of 3.2% and 2.0%, respectively. On the other hand, the decrease in heating performance is similar to the decrease in cooling performance of case G2_L1_In_3 (-61.1%, -60.0% and -59.5% for the first, second and third year of simulation).

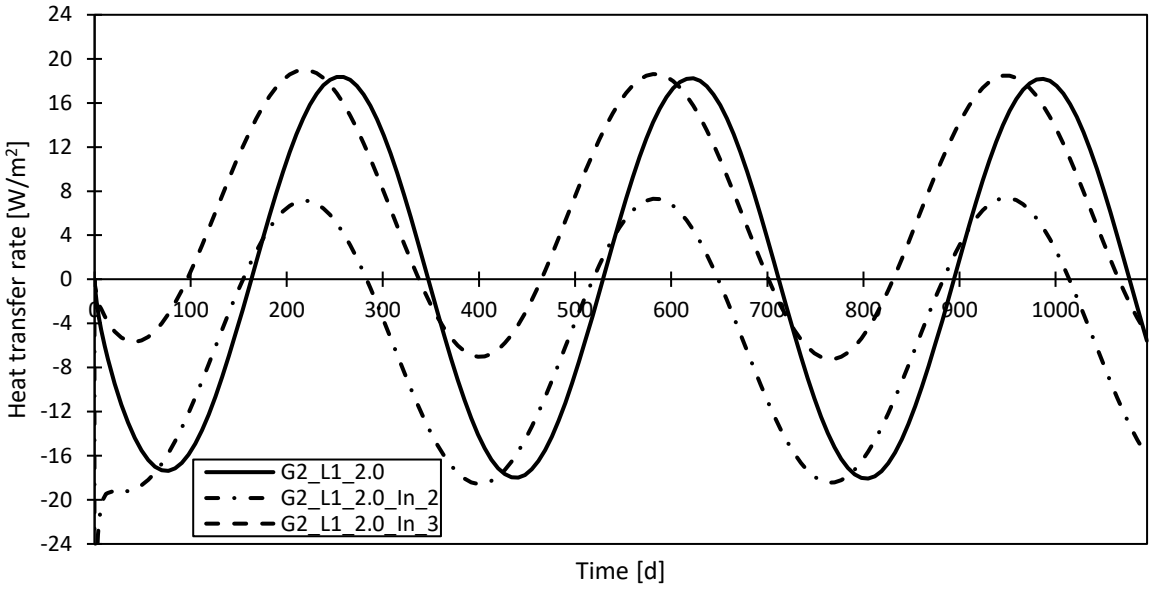

Figure 5.16 - Heat transfer rate evolution during the three years of simulation, for the additional inlet temperature analysis.

The two cases simulation time was extended to 10 years to check possible losses in the heat transfer rate due to system saturation. As shown by Table 5-14, the difference in heat transfer rate between the tenth year and the third year of simulation is not significant. Therefore, no significant decrease in performance is observed after 10 years of simulation, which indicates that this configuration favours the heat exchange with the interior space that has a variable temperature BC (Int_1) assigned. In the case of a convective or adiabatic BC assigned to the exposed wall surface, some thermal performance decrease is expected after ten years of simulation.

Table 5-14 - Peak heat transfer rate for the additional inlet temperature analysis.

	Peak Heat Transfer Rate, q [W/ m²]					
	G2_L1_2.0		**G2_L1_2.0_In_2**		**G2_L1_2.0_In_3**	
Year	**Heating**	**Cooling**	**Heating**	**Cooling**	**Heating**	**Cooling**
1st	18.36	-17.37	19.01	-5.68	19.01	-5.68
2nd	18.23	-17.99	18.63	-7.03	18.63	-7.03
3rd	18.19	-18.08	18.47	-7.25	18.47	-7.25
10th	-	-	18.32	-7.45	18.32	-7.45

6 Conclusions and future developments

The aim of this thesis was to provide relevant knowledge regarding the thermal behaviour of energy walls, a type of energy geostructure which has seen a rising interest in the last decade but that still lack a full understanding regarding the parameters that impact their thermal performance the most, essential to provide an efficient design, that maximizes the heat exchanged for multiple scenarios of application.

Firstly, a review and summary of previous works was undertaken, highlighting their assumptions and key differences, as well as the variations that those produce in the thermal performance of the considered energy walls. As seen, a key difference between energy walls and other types of energy geostructures or SGE systems is that a large portion of the wall is exposed to the interior environment, a medium without the stable temperature profiles throughout the year, characteristic of the ground. Therefore, a set of numerical analyses were assembly in the finite element software FEFLOW to evaluate the impact on the heat transfer rate of the wall geometry, the soil thermal conductivity, the interior space, the exterior ground surface and the thermal load imposed by the inlet temperature. As seen:

- The deepest geometries result in lower heat transfer rates per square metre of wall as the higher area overcomes the heat power gains, even though the deepest geometries provide significantly more energy than the shallower geometries;
- The soil thermal conductivity proves to have a significant positive impact on the heat transfer rate, with an average increase as high as 23.3% between a soil thermal conductivity of 1.0 W/m K and 3.0 W/m K;
- The conditions on the interior space in contact with the wall also impact the heat transfer rate considerably, with a decrease of almost 13% when low air speeds are considered at the interior space, and a decrease of almost 42% when insulation between the wall and the space is considered. Additionally, an interior space with excessive heat proves to be beneficial for heating but detrimental to the cooling operation;
- The temperature of the top boundary condition (surface ground temperature) was found to have a limited impact on the heat transfer rate;
- The unbalanced thermal load imposed by the inlet temperature impacts the amount of energy extracted for cooling and heating, but the impact seems to stabilise in the first two annual cycles and no system saturation (in terms of soil temperature change and further loss of efficiency) was observed in the long term

Overall, this thesis provides additional knowledge for the energy walls subject that can act as guideline in future developments. In a first stage, an even more extensive parametric study should be assembled to try to create a design guideline, which was not entirely possible in this thesis. Namely, combining all the parameters considered in the baseline analysis with additional values of D_b and D_w/D_e ratios, after which a combined analysis of all the parameters must be undertaken. Due to the large amount of data that those analyses will generate, processes like data mining should be employed to identify patterns in

the system response and establish the degree of impact that each parameters has on the thermal performance of energy walls.

Additionally, and even though there some reports in the literature that state that the structural behaviour of energy walls is not compromised by the imposed thermal load, coupled thermal-mechanical 3D analyses are still scarce, due to the high computational resources needed to performed them and additional studies should be performed.

Lastly, a more detailed analysis regarding the integration of energy walls in the heating and cooling system of buildings should be undertaken, considering the thermal loads imposed by different types of buildings, to assess how much of that energy demand is satisfied by energy walls, as well as an economical point of view analysis. Additionally, the numerical results of energy walls should be included in the energy simulation of buildings.

References

Adam, D., & Markiewicz, R. (2009). Energy from earth-coupled structures, foundations, tunnels and sewers. *Geotechnique*, *59*(3), 229–236. https://doi.org/10.1680/geot.2009.59.3.229

Amis, T. (2011). Energy Piles and Diaphragm Walls. *Ground Source Live*, *June*.

Amis, T., Robinson, C. A. W., & Wong, S. (2010). Integrating Geothermal Loops into the Diaphragm Walls of the Knightsbridge Palace Hotel Project. *Proceeding of the 11th DFI / EFFC International Conference, London*, *July*, 10.

Angelotti, A., & Sterpi, D. (2018). On the performance of energy walls by monitoring assessment and numerical modelling: a case in Italy. *Environmental Geotechnics*, 1–8. https://doi.org/10.1680/jenge.18.00037

Banks, D. (2012). *An Introduction to Thermogeology: Ground Source Heating and Cooling* (2nd ed.). John Wiley & Sons.

Barla, M., & Di Donna, A. (2018). Energy tunnels: concept and design aspects. *Underground Space*, *3*(4), 268–276. https://doi.org/10.1016/j.undsp.2018.03.003

Barla, M., Di Donna, A., & Perino, A. (2016). Application of energy tunnels to an urban environment. *Geothermics*, *61*, 104–113. https://doi.org/10.1016/j.geothermics.2016.01.014

Barla, M., Di Donna, A., & Santi, A. (2020). Energy and mechanical aspects on the thermal activation of diaphragm walls for heating and cooling. *Renewable Energy*, *147*, 2654–2663. https://doi.org/10.1016/j.renene.2018.10.074

Bergman, T. L., Lavine, A. S., Incropera, F. P., & DeWitt, D. P. (2011). Fundamentals of Heat and Mass Transfer, 7th Edition. In *John Wiley & Sons* (7th ed., Vol. 33, Issue 2).

Bourne-Webb, P. J., Amatya, B., Soga, K., Amis, T., Davidson, C., & Payne, P. (2009). Energy pile test at lambeth college, London: Geotechnical and thermodynamic aspects of pile response to heat cycles. *Geotechnique*, *59*(3), 237–248. https://doi.org/10.1680/geot.2009.59.3.237

Bourne-Webb, P. J., Bernard, J.-B., Friedemann, W., von der hude, N., Pralle, N., Uotinen, V. M., & Widerin, B. (2013). Delivery of Energy Geostructures. In *Energy Geostructures* (pp. 229–263). John Wiley & Sons, Inc. https://doi.org/10.1002/9781118761809.ch12

Bourne-Webb, P. J., & Bodas Freitas, T. M. (2020). Thermally-activated piles and pile groups under monotonic and cyclic thermal loading–A review. *Renewable Energy*, *147*(xxxx), 2572–2581. https://doi.org/10.1016/j.renene.2018.11.025

Bourne-Webb, P. J., Bodas Freitas, T. M., & Da Costa Gonçalves, R. A. (2016). Thermal and mechanical aspects of the response of embedded retaining walls used as shallow geothermal heat exchangers. *Energy and Buildings*, *125*, 130–141. https://doi.org/10.1016/j.enbuild.2016.04.075

Bourne-Webb, P. J., Bodas Freitas, T. M., & Freitas Assunção, R. M. (2019). A review of pile-soil interactions in isolated, thermally-activated piles. *Computers and Geotechnics*, *108*(November 2018), 61–74. https://doi.org/10.1016/j.compgeo.2018.12.008

Brandl, H. (2006). Energy foundations and other thermo-active ground structures. *Geotechnique*, *56*(2), 81–122. https://doi.org/10.1680/geot.2006.56.2.81

Buhmann, P., Moormann, C., Westrich, B., Pralle, N., & Friedemann, W. (2016). Tunnel geothermics—A German experience with renewable energy concepts in tunnel projects. *Geomechanics for*

Energy and the Environment, *8*, 1–7. https://doi.org/10.1016/j.gete.2016.10.006

Calado, A. (2016). *Monitorização da temperatura do solo . Desenvolvimento e estudo experimental de um permutador de calor ar-solo*. Universidade da Beira Interior.

Chamorro, C. R., García-Cuesta, J. L., Mondéjar, M. E., & Pérez-Madrazo, A. (2014). Enhanced geothermal systems in Europe: An estimation and comparison of the technical and sustainable potentials. *Energy*, *65*, 250–263. https://doi.org/10.1016/j.energy.2013.11.078

Di Donna, A., Cecinato, F., Loveridge, F., & Barla, M. (2017). Energy performance of diaphragm walls used as heat exchangers. *Proceedings of the Institution of Civil Engineers: Geotechnical Engineering*, *170*(3), 232–245. https://doi.org/10.1680/jgeen.16.00092

Di Donna, A., Loveridge, F., Piemontese, M., & Barla, M. (2020). The role of ground conditions on the heat exchange potential of energy walls. *Geomechanics for Energy and the Environment*, *3*. https://doi.org/10.1016/j.gete.2020.100199

Diersch, H. J. G. (2014). FEFLOW: Finite element modeling of flow, mass and heat transport in porous and fractured media. In *FEFLOW: Finite Element Modeling of Flow, Mass and Heat Transport in Porous and Fractured Media* (Vol. 9783642387). https://doi.org/10.1007/978-3-642-38739-5

Fadejev, J., Simson, R., Kurnitski, J., & Haghighat, F. (2017). A review on energy piles design, sizing and modelling. *Energy*, *122*, 390–407. https://doi.org/10.1016/j.energy.2017.01.097

Franzius, J. N., & Pralle, N. (2011). Turning segmental tunnels into sources of renewable energy. *Proceedings of the Institution of Civil Engineers: Civil Engineering*, *164*(1), 35–40. https://doi.org/10.1680/cien.2011.164.1.35

Frodl, S., Franzius, J. N., & Bar, T. (2010). Planung und bau der tunnel-geothermieanlage in Jenbach. *Geomechanik Und Tunnelbau*, *3*(5), 658–668. https://doi.org/10.1002/geot.201000037

Goetzl, G. (2020). *MUSE – Differences between deep and shallow geothermal energy*. GeoERA. https://geoera.eu/blog/muse-differences-between-deep-and-shallow-geothermal-energy/

IPMA. (2015). *Portal do Clima*. http://portaldoclima.pt/en/

Kürten, S., Mottaghy, D., & Ziegler, M. (2015). Design of plane energy geostructures based on laboratory tests and numerical modelling. *Energy and Buildings*, *107*, 434–444. https://doi.org/10.1016/j.enbuild.2015.08.039

Laloui, L., & Rotta Loria, A. F. (2020). Energy geostructures. In *Analysis and Design of Energy Geostructures* (pp. 25–65). Elsevier. https://doi.org/10.1016/B978-0-12-816223-1.00002-3

Lee, C., Park, S., Choi, H. J., Lee, I. M., & Choi, H. (2016). Development of energy textile to use geothermal energy in tunnels. *Tunnelling and Underground Space Technology*, *59*, 105–113. https://doi.org/10.1016/j.tust.2016.06.014

Loveridge, F. (2012). The Thermal Performance of Foundation Piles used as Heat Exchangers in Ground Energy Systems. In *University of Southhampton*.

Loveridge, F., McCartney, J. S., Narsilio, G. A., & Sanchez, M. (2020). Energy geostructures: A review of analysis approaches, in situ testing and model scale experiments. *Geomechanics for Energy and the Environment*, *22*, 100173. https://doi.org/10.1016/j.gete.2019.100173

Lowe, R., Chiu, L. F., Oikonomou, E., Gleeson, C., Love, J., Wingfield, J., & Biddulph, P. (2017). *Final Report on Analysis of Data From Heat Pumps Installed Via the Renewable Heat Premium Payment*

(RHPP) Scheme.

Makasis, N., & Narsilio, G. A. (2020). Energy diaphragm wall thermal design: The effects of pipe configuration and spacing. *Renewable Energy*, *154*, 476–487. https://doi.org/10.1016/j.renene.2020.02.112

Miara, M., Guenther, D., Kramer, T., Oltersdorf, T., & Wapler, J. (2011). *Heat Pump Efficiency - Analysis and Evaluation of Heat Pump Efficiency in Real-life Conditions*. 42.

Nicholson, D. P., Chen, Q., Pillai, A., & Chendorain, M. (2013). Developments in thermal piles and thermal tunnel lining for city scale GSHP systems. *Thirty-Eighth Workshop on Geothermal Reservoir Engineering*, 1437–1444.

Rees, S. J. (2016a). 1 - An introduction to ground-source heat pump technology. In S. J. Rees (Ed.), *Advances in Ground-Source Heat Pump Systems* (pp. 1–25). Woodhead Publishing. https://doi.org/https://doi.org/10.1016/B978-0-08-100311-4.00001-7

Rees, S. J. (2016b). 5 - Horizontal and compact ground heat exchangers. In S. J. Rees (Ed.), *Advances in Ground-Source Heat Pump Systems* (pp. 117–156). Woodhead Publishing. https://doi.org/https://doi.org/10.1016/B978-0-08-100311-4.00005-4

Sanner, B. (2004). Geothermal heat pumps technologies and development. *Technika Poszukiwań Geologicznych*, *43*(5–6), 26–34.

Snijders, A. L., & Drijver, B. C. (2016). 9 - Open-loop heat pump and thermal energy storage systems. In *Advances in Ground-Source Heat Pump Systems* (pp. 247–268). Elsevier. https://doi.org/10.1016/B978-0-08-100311-4.00009-1

Soga, K., & Rui, Y. (2016). 7 - Energy geostructures. In S. J. Rees (Ed.), *Advances in Ground-Source Heat Pump Systems* (pp. 185–221). Woodhead Publishing. https://doi.org/https://doi.org/10.1016/B978-0-08-100311-4.00007-8

Soga, K., Rui, Y., & Nicholson, D. (2015). Behaviour of a thermal wall installed in the Tottenham Court Road station box. *Proc. Crossrail Conference, Crossrail Ltd and Federation of Piling Specialists, City Hall, London*, 112–119.

Sterpi, D., Angelotti, A., Habibzadeh-Bigdarvish, O., & Jalili, D. (2018). Assessment of thermal behaviour of thermo-active diaphragm walls based on monitoring data. *Journal of Rock Mechanics and Geotechnical Engineering*, *10*(6), 1145–1153. https://doi.org/10.1016/j.jrmge.2018.08.002

Sterpi, D., Tomaselli, G., & Angelotti, A. (2020). Energy performance of ground heat exchangers embedded in diaphragm walls: Field observations and optimization by numerical modelling. *Renewable Energy*, *147*, 2748–2760. https://doi.org/10.1016/j.renene.2018.11.102

Sun, M., Xia, C., & Zhang, G. (2013). Heat transfer model and design method for geothermal heat exchange tubes in diaphragm walls. *Energy and Buildings*, *61*, 250–259. https://doi.org/10.1016/j.enbuild.2013.02.017

Tan, Y., & Li, M. (2011). Measured performance of a 26 m deep top-down excavation in downtown Shanghai. *Canadian Geotechnical Journal*, *48*(5), 704–719. https://doi.org/10.1139/t10-100

Tan, Y., & Wei, B. (2012). Observed Behaviors of a Long and Deep Excavation Constructed by Cut-and-Cover Technique in Shanghai Soft Clay. *Journal of Geotechnical and Geoenvironmental Engineering*, *138*(1), 69–88. https://doi.org/10.1061/(ASCE)GT.1943-5606.0000553

Tinti, F., Boldini, D., Ferrari, M., Lanconelli, M., Kasmaee, S., Bruno, R., Egger, H., Voza, A., & Zurlo, R. (2017). Exploitation of geothermal energy using tunnel lining technology in a mountain environment. A feasibility study for the Brenner Base tunnel – BBT. *Tunnelling and Underground Space Technology*, *70*(August), 182–203. https://doi.org/10.1016/j.tust.2017.07.011

Xia, C., Sun, M., Zhang, G., Xiao, S., & Zou, Y. (2012). Experimental study on geothermal heat exchangers buried in diaphragm walls. *Energy and Buildings*, *52*, 50–55. https://doi.org/10.1016/j.enbuild.2012.03.054

Xiong, Z., Fisher, D. E., & Spitler, J. D. (2015). Development and validation of a Slinky™ ground heat exchanger model. *Applied Energy*, *141*, 57–69. https://doi.org/10.1016/j.apenergy.2014.11.058

Xu, Q., Zhu, H., Ma, X., Ma, Z., Li, X., Tang, Z., & Zhuo, K. (2015). A case history of shield tunnel crossing through group pile foundation of a road bridge with pile underpinning technologies in Shanghai. *Tunnelling and Underground Space Technology*, *45*, 20–33. https://doi.org/10.1016/j.tust.2014.09.002

Zottl, A., & Nordman, R. (2012). *D4.2 /D 2.4. Concept for evaluation of SPF Version 2.2*. 1–18.

Appendix

Appendix A

Efficiency of GSHP systems

The efficiency of a ground source heat pump can be evaluated by the ratio between the extracted energy and the energy spent for operation. This coefficient is referred to as the coefficient of performance (COP) and is defined as:

$$COP = \frac{E}{W_r} \tag{A-1}$$

Where E is the quantity of energy removed or supplied and W_r is the quantity of work required by the system for heating and cooling, respectively (Rees, 2016a). A heat pump is a heat engine that transforms thermal energy into mechanical energy, working in reverse, the same theoretical limit efficiency (Carnot efficiency) applies. The Carnot theorem states that the limiting factors for heat engine efficiency are the temperature at which the heat enters the engine and the temperature of the reservoir in which the engine dumps the heat. Therefore, the coefficient of performance has a maximum value in heating mode (A-2) and cooling mode (A-3) defined as:

$$COP_{max}^{heating} = \frac{T_H}{T_H - T_C} \tag{A-2}$$

$$COP_{max}^{cooling} = \frac{T_C}{T_C - T_H} \tag{A-3}$$

Where T_H is the absolute temperature of the hot reservoir and T_C is the absolute temperature of the cold reservoir.

As shown by equations (A-2) and (A-3), GSHPs do not have a fixed COP due to the dependency on the reservoir temperatures. Hence, higher efficiencies are achievable with similar source and sink temperatures (as the divisor in the equations tens to zero). Since GSHPs exchange heat with an almost constant temperature reservoir, high COP values are achievable which indicates that the energy delivered is much bigger than the one consumed by the system (see Figure 2.4). However, thermal loads must be reliably predicted and either balanced or restricted, to prevent excessive heat extraction or injection which would lead to permanent soil temperature changes that impact the long-term efficiency of the system. An inter-seasonal operation with balanced heating and cooling loads is most favourable.

Because of this, if the energy used by GSHPs to operate comes from renewable energy sources, the carbon emissions associated with heating and cooling can be severely reduced and minimal, even comparing to electrical resistance heating using renewable energy, as the latter lacks the energy multiplying capacity of GSHPs (Rees, 2016a). Additionally, GSHPs are more efficient than other heat pumps, such as air source heat pumps (ASHP), because the ground temperature is closer to room temperature than to the air temperature, which eliminates the need of additional energy consumption to defrost ASHP evaporator in low air temperatures heating periods and to raise the refrigerant fluid to a

temperature higher than the exterior temperature, which significantly lowers heat pump performance during the most demanding periods of heat demand.

GSHP system efficiency must consider the whole system and not only the efficiency of the GSHP. The circulation pumps of the primary and secondary circuits, as well as supplementary heating or cooling sources that some GSHP systems can incorporate, have an impact on the efficiency of the whole system. Additionally, the secondary circuit can also significantly impact the system efficiency since the required output temperature is controlled by the type of heat distribution equipment. According to Banks (2012), temperature values may be:

- Higher than 60ºC for old conventional hot water heating system;
- 45-55ºC for low temperature, high radiator surface heating system;
- 35-45ºC for underfloor water circulating heating system;
- 25-30ºC for air circulating heating system.

As seen previously, heat pump efficiency increases with lower temperature gradients between source and sink which makes them more suitable for underfloor and air circulating heating systems.

There has been some concern among researchers regarding the definition of a performance metric that considers the efficiency of the whole system. To answer this, a seasonal performance factor (SPF) was defined and can be established from the average of monitoring data of systems and technologies that already have been implemented, which allows the comparison with other heating systems, like oil and gas, and the estimation of running costs and carbon emission savings (Rees, 2016a).

To calculate the SPF, a variety of system boundaries must be defined to evaluate the impact of the different components on the system efficiency. Therefore, the European project SEPEMO (Zottl & Nordman, 2012) defined these system boundaries, SPF_{H1} through SPF_{H4}, for heating mode and SPF_{C1} through SPF_{C4}, for cooling mode. As the methodology is the same for both operation modes, a scheme of the heating mode system boundaries is presented in Figure A.1. SPF_{H1} system refers to the refrigerant cycle performance, therefore being similar to the COP definition presented earlier, except that COP metric considers a small part of the pump electric consumption and most fan electric consumption. SPF_{H2} system adds the equipment that allows the heat source to be available to the heat pump, such as the circulating pumps on the ground loop and SPF_{H3} system adds the backup heater (if installed), which allows the comparison with other heating systems since it represents the whole heat pump system. Lastly, SPF_{H4} takes into account the auxiliary equipment of the heat distribution circuit. Additionally, for SPF_{H3} and SPF_{H4}, when the energy source of the backup heater is other than electricity, the energy content has to be determined through the fuel demand and calorific value. Also, in case of solar thermal backup, the energy required to run the system has to be considered (Zottl & Nordman, 2012).

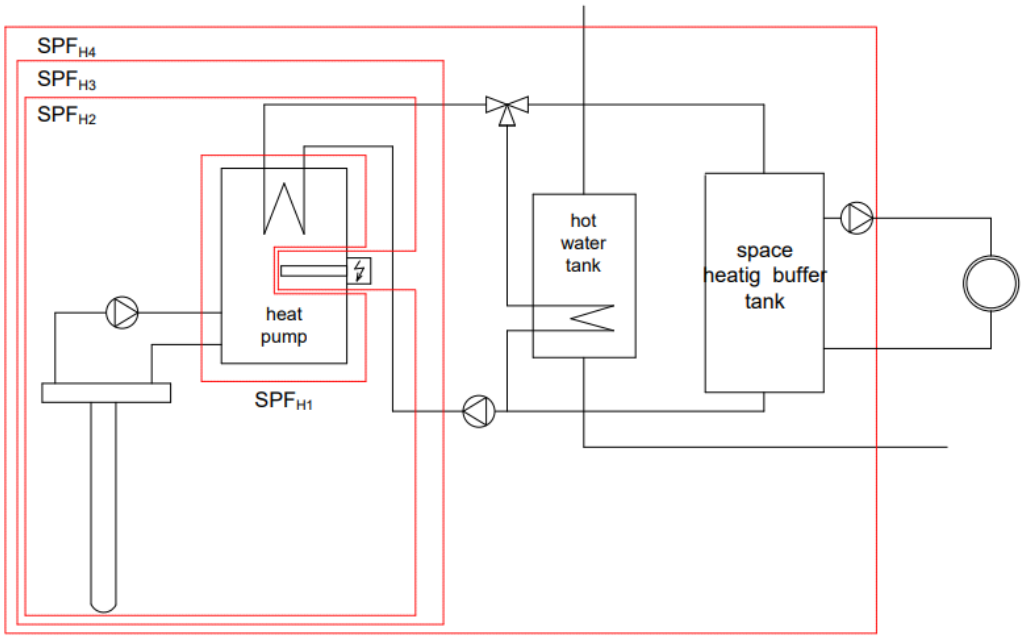

Figure A.1 - Schematic representation of system boundaries for SPF calculation (Zottl & Nordman, 2012).

The SPF system boundaries described previously are defined trough the following equations presented by Zottl & Nordman (2012):

$$SPF_{H1} = \frac{Q_{H\_hp} + Q_{W\_hp}}{E_{HW\_hp}} \quad \text{(A-4)}$$

Where:

- Q_{H_hp} is the quantity of heat of the heat pump in space heating operation [kWh];
- Q_{W_hp} is the quantity of heat of the heat pump in domestic hot water operation [kWh];
- E_{HW_hp} is the electrical energy use of the heat pump for space heating and domestic hot water [kWh];

$$SPF_{H2} = \frac{Q_{H\_hp} + Q_{W\_hp}}{E_{S_{fan/pump}} + E_{HW\_hp}} \quad \text{(A-5)}$$

Where:

- $E_{S_{fan/pump}}$ is the electrical energy use of the heat pump source: fan or heat carrier fluid pump for space heating and domestic hot water [kWh];

$$SPF_{H3} = \frac{Q_{H\_hp} + Q_{W\_hp} + Q_{HW\_bu}}{E_{S_{fan/pump}} + E_{HW\_hp} + E_{HW\_bu}} \quad \text{(A-6)}$$

Where:

- E_{HW_bu} is the energy use of back-up heater for space heating and domestic hot water [kWh];

$$SPF_{H4} = \frac{Q_{H\_hp} + Q_{W\_hp} + Q_{HW\_bu}}{E_{S_{fan/pump}} + E_{HW\_hp} + E_{bt\_pump} + E_{HW\_bu} + E_{B_{fan/pump}}} \quad \text{(A-7)}$$

Where:

- E_{bt_pump} is the electrical energy use of the buffer tank pump [kWh];
- $E_{B_{fan/pump}}$ is the electrical energy use of the heat sink (building): fans or pumps for space heating and domestic hot water [kWh];

In cooling mode, the system composition is similar to that presented in Figure A.1 for the heating mode, except for the absence of the hot water tank. If an auxiliary cooling unit is installed, the electrical energy use of this additional cooling unit is only accounted in SPF_{C4} since it is considered independent from the main system. The full description of the two operation modes as well as a comparison with other standards is available in Zottl & Nordman (2012).

A report from GSHP systems field trials in the UK (Lowe et al., 2017) presented some conclusions regarding SPF_{H2} and SPF_{H4} values. A sample of 99 GSHP systems showed a SPF_{H2} median value of 2.81 (range of values between 2.52 and 3.16), with 77% of them with SPF_{H2} values higher than 2.5. ASHP systems showed a SPF_{H2} median value of 2.63 (range between 2.24 and 2.94) and 58% with values of SPF_{H2} higher than 2.5. Additionally, the authors highlighted that the minimum values for SPF_{H4} required to make CO_2 savings are much lower than the ones needed to make cost savings when compared to conventional heating systems, even in the UK that has a fairly high electricity carbon intensity. The highest minimum value of SPF_{H4} for CO_2 reduction was set as 1.5 when compared to gas as a heat source and the highest minimum value of SPF_{H4} for cost reduction was set as 3.25 when compared to oil as a heat source, although cost reductions are very sensitive to tariffs. Miara et al. (2011) reported a comparison study between ASHP and GSHP efficiency undertaken between 2007 and 2010 in Germany. The authors report average SPF_{H3} values ranging between 3.9 and 4.1 for GSHP and between 2.9 and 3.0 for ASHP. They also point out that more than 90% of the heat pumps were combined with underfloor heating systems, resulting in an average inlet temperature for the heating period of 36ºC. In summer, when DHW operation was predominant, an average inlet temperature of 52ºC was determined. Consequently, a decrease in the SPF_{H3} value was observed which leads authors to recommend the lowest operation temperatures possible in the heat distribution and DHW systems.

Appendix B

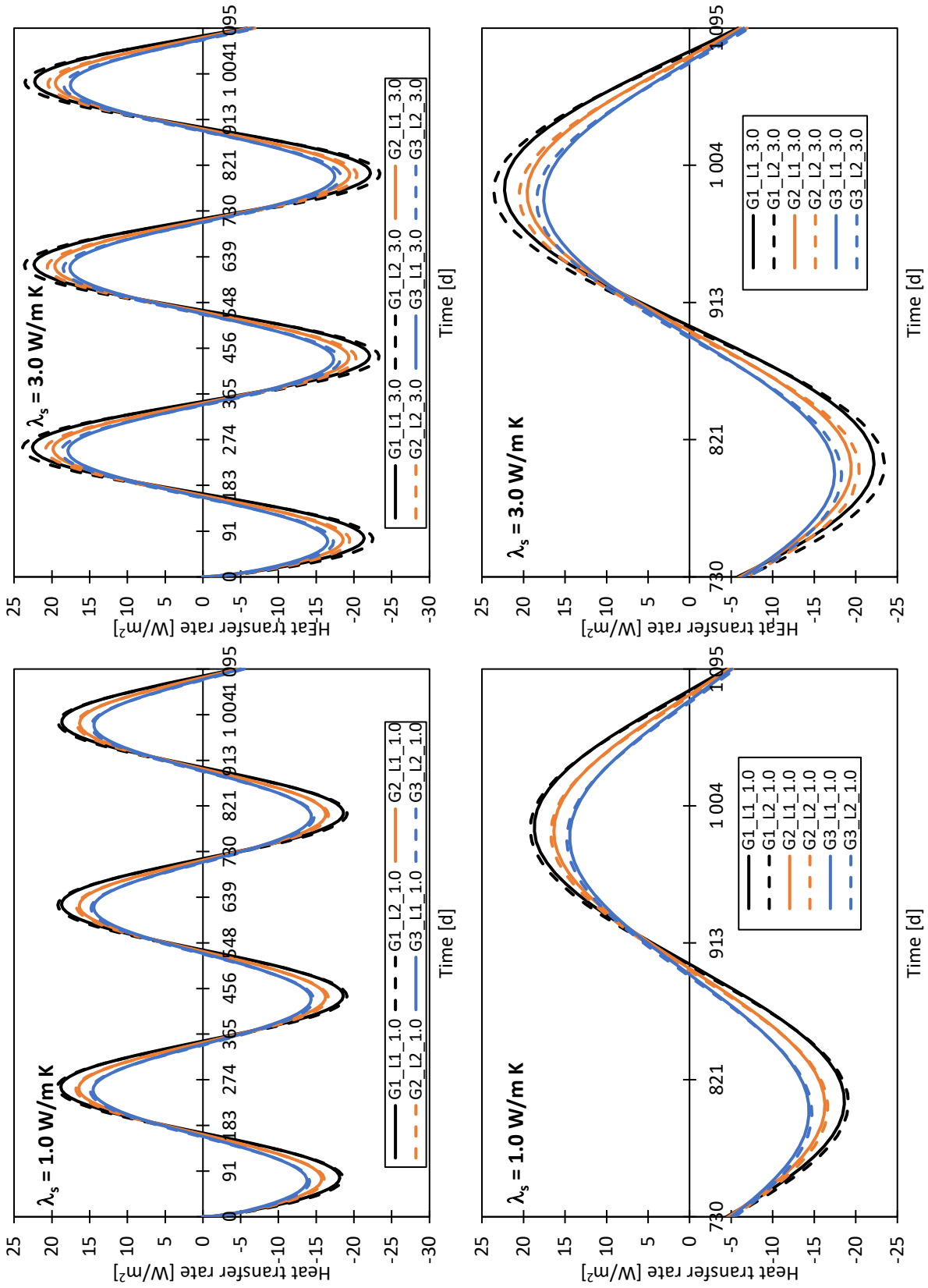
λs = 1.0 W/m K
λs = 3.0 W/m K
Heat transfer rate [W/m²]
Time [d]
G1_L1_1.0
G1_L2_1.0
G2_L1_1.0
G2_L2_1.0
G3_L1_1.0
G3_L2_1.0
G1_L1_3.0
G1_L2_3.0
G2_L1_3.0
G2_L2_3.0
G3_L1_3.0
G3_L2_3.0

Appendix C

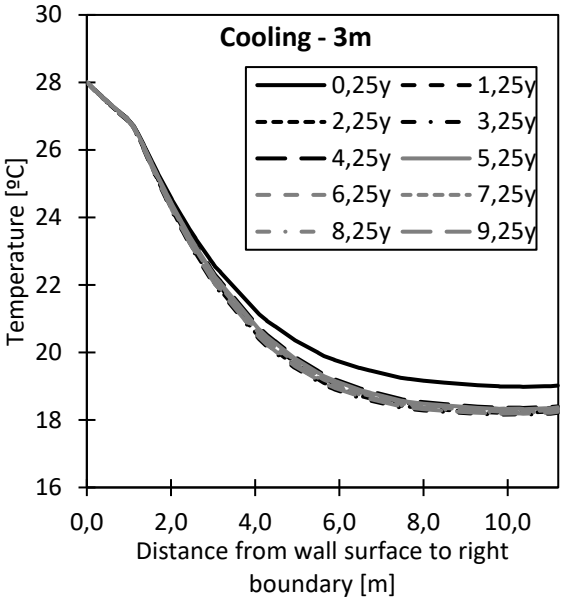
Cooling - 3m
Temperature [ºC]
30
28
26
24
22
20
18
16
0,0
2,0
4,0
6,0
8,0
10,0
Distance from wall surface to right boundary [m]
0,25y
1,25y
2,25y
3,25y
4,25y
5,25y
6,25y
7,25y
8,25y
9,25y

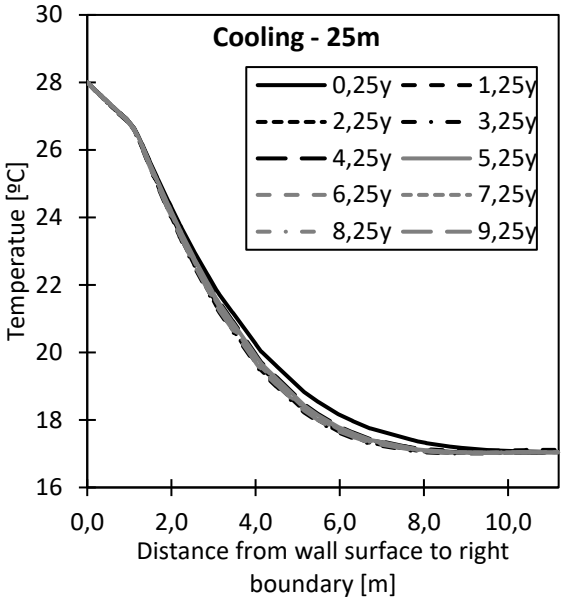
Cooling - 25m
Temperatue [ºC]
30
28
26
24
22
20
18
16
0,0
2,0
4,0
6,0
8,0
10,0
Distance from wall surface to right boundary [m]
0,25y
1,25y
2,25y
3,25y
4,25y
5,25y
6,25y
7,25y
8,25y
9,25y

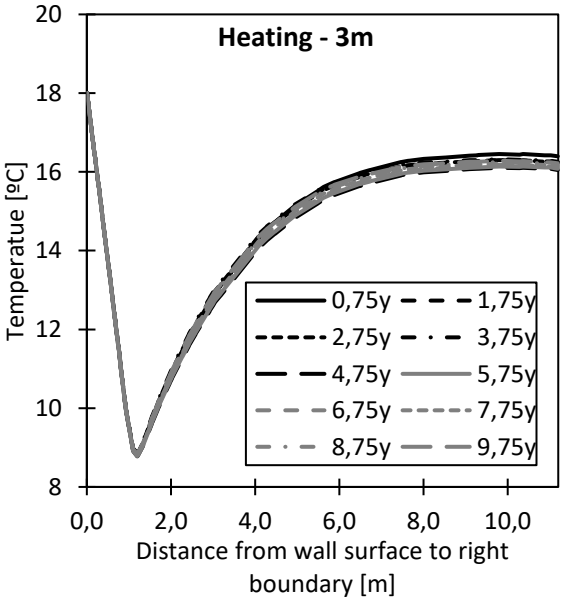
Heating - 3m
Temperatue [ºC]
20
18
16
14
12
10
8
0,0
2,0
4,0
6,0
8,0
10,0
Distance from wall surface to right boundary [m]
0,75y
1,75y
2,75y
3,75y
4,75y
5,75y
6,75y
7,75y
8,75y
9,75y

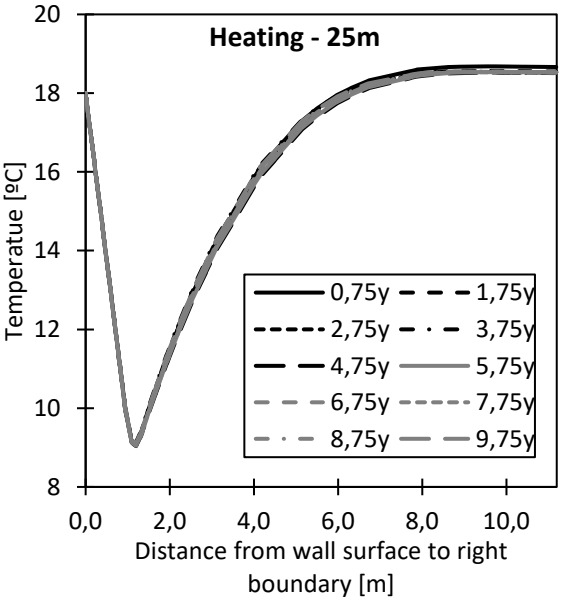
Heating - 25m
Temperatue [ºC]
20
18
16
14
12
10
8
0,0
2,0
4,0
6,0
8,0
10,0
Distance from wall surface to right boundary [m]
0,75y
1,75y
2,75y
3,75y
4,75y
5,75y
6,75y
7,75y
8,75y
9,75y